

Electronic Thesis and Dissertation Repository

3-20-2020 3:00 PM

Characterization and Enhancement of Local Drug Delivery in Orthopaedic Infection

Tina Khazae, *The University of Western Ontario*

Supervisor: David W. Holdsworth, *Robarts Research Institute*

A thesis submitted in partial fulfillment of the requirements for the Master of Science degree in Medical Biophysics

© Tina Khazae 2020

Follow this and additional works at: <https://ir.lib.uwo.ca/etd>



Part of the [Medical Biophysics Commons](#)

Recommended Citation

Khazae, Tina, "Characterization and Enhancement of Local Drug Delivery in Orthopaedic Infection" (2020). *Electronic Thesis and Dissertation Repository*. 6851.
<https://ir.lib.uwo.ca/etd/6851>

This Dissertation/Thesis is brought to you for free and open access by Scholarship@Western. It has been accepted for inclusion in Electronic Thesis and Dissertation Repository by an authorized administrator of Scholarship@Western. For more information, please contact wlsadmin@uwo.ca.

Abstract

The delivery of antibiotics is an important component of therapy for orthopedic device-related infections (ODRI). In this study, we have investigated new techniques to characterize and enhance antibiotic delivery for ODRI. Characterization of small-molecule diffusion is essential to the development of drug-delivery systems. We have developed a quantitative, non-invasive, longitudinal, micro-CT technique to quantify the diffusion of small-molecules in an intact phantom. We employed a radio-opaque molecule (*i.e.*, Iohexol) as a surrogate for commonly used antibiotics (*e.g.*, Vancomycin). We characterized diffusion from a finite-core carrier into an agar, tissue-equivalent phantom. The estimate of the diffusion coefficient was derived from the analysis of radial diffusion distance of Iohexol and the cumulative release amount of this drug surrogate. This micro-CT method enabled us to describe the elution of small-molecules from enhanced carriers within a porous metal scaffold. To enhance antibiotic delivery, we designed and fabricated gyroid-based scaffolds with appropriate mechanical properties and filled with Iohexol-loaded carriers. Diffusion characteristics within the porous structures were evaluated using the micro-CT technique.

Keywords

Diffusion, small-molecules, local drug delivery, micro-CT, drug-surrogate, contrast agent, orthopedic device-related infection, 3D-printed porous scaffold.

Summary for Lay Audience

Orthopedic device-related infection is a devastating problem that is associated with metal implants. Infection can occur any time after primary orthopedic surgery, and can result in severe residual disability and in-hospital mortality; thus, it is a burden for the health care system and for patients. In this work, we focused on infection near orthopedic joint implants, since more than 130,000 knee and hip joint replacement surgeries are performed each year in Canada and thousands become infected.

The current treatment for implant-associated infection is two-stage revision surgery. The first challenge is to eliminate the infection; thus, patients would undergo invasive surgery to remove the infected components. During this stage, the patient would also receive systemic antibiotics in addition to local antibiotics to the target joint.

Local treatment would be performed by placing a temporary component that can be loaded with antibiotics. This temporary component maintains the structure of the joint and releases drugs to the target tissue. However, current antibiotic carriers are not highly effective for local infection treatment and release an insufficient amount of the drugs to the target tissue. After 6-8 weeks, if the infection is eradicated, temporary carriers should be removed due to the low mechanical properties of these carriers; hence, a second surgery would be performed to remove the carrier and place the final revision implants.

In this work, our goal was to understand how antibiotics are being released through carriers to the surrounding tissue. We used a micro-CT imaging technique to monitor the release of a drug mimic from a commonly used orthopedic carrier to a tissue-equivalent phantom and characterized the release. We were able to optimize the imaging technique for evaluating the diffusion of the drug from various carriers, qualitatively, and quantitatively.

Upon understanding of drug release, we proposed the application of highly-porous 3D-printed metal structures in combination with current antibiotic carriers. The pores of the structure can be filled with the antibiotic-loaded carrier to satisfy the needs for local infection treatment, while the material properties (*i.e.*, titanium alloy) would maintain the mechanical strength that is required for a joint implant; thus can be retained in the joint and eliminate the need for multiple surgeries.

Co-Authorship Statement

The following thesis contains two manuscripts, one has been submitted, and the second is intended for publication within scientific journals. Chapter 2 is an original research article entitled “Micro-CT imaging technique to characterize diffusion of small- molecules” and has been submitted for publication within the proceedings of the SPIE, Medical Imaging 2020: Biomedical Applications in Molecular, Structural, and Functional Imaging, Volume 11317, in January 2020. This manuscript is co-authored by Tina Khazae, Chris J.D Norley, Hristo N. Nikolov, Steven I. Pollmann, and David W. Holdsworth. In my role as an MSc candidate, I was responsible for the experimental design, phantom fabrication, performing micro-CT scans, artifact corrections, optimization of image analysis methods, all data analysis, mathematical interpretation of experiments, and final manuscript preparation. Chris J.D Norely advised on image acquisitions and provided editorial input. Steven I. Pollman aided in artifact correction, and Hristo N. Nikolov contributed to the experimental design of this work. David W. Holdsworth, as the principal investigator and supervisor, designed the study, reviewed the results, gave editorial assistance, and provided mentorship.

Chapter 3 is an original research article in preparation, entitled “Mechanical Properties and Diffusion Characterization of Highly Porous 3D-printed Scaffolds.” The manuscript is co-authored by Tina Khazae, Santiago Cobos, Gregory Hong, Todor G. Ivanov, and David W. Holdsworth. In my role as an MSc candidate, I was involved in the study design, contributed to the mechanical analysis, performed micro-CT scans and reconstructions, analyzed and interpreted all data, and wrote the manuscript text. Santiago Cobos contributed to the study design, Gregory Hong aided with the CAD design, and Todor G. Ivanov was involved in finite element analysis. David W. Holdsworth, as the principal investigator and supervisor, designed the study, reviewed the results, gave editorial assistance, and provided mentorship.

Acknowledgments

I would like to acknowledge those individuals who have given me guidance and support throughout my time as a graduate student. First and foremost, I would like to thank my supervisor David Holdsworth for his mentorship during my time in his group. He has helped me to understand the capabilities of X-ray imaging systems better, develop my problem-solving skills, improve my communication as a scientific researcher, and has provided valuable insight to each of my projects.

I would like to thank, my advisory committee: Mathew Teeter for his effort to improve my communication skill through his valuable feedbacks, his guidance in the study progress and his willingness to support when I had any concern or questions; David Heinrichs as his wealth of knowledge in infection helped me to develop the conceptual idea of my research and to understand the burden of infection better.

I would like to acknowledge the efforts of all the students and staff within the Holdsworth lab for their support and collaborative efforts that make the day-to-day operations feasible. In particular, Hristo Nikolov, Steven Pollmann, Todor Ivanov, Jaques Milner. Special thanks must also be given to Chris Norley, for his endless support, spending many long days behind the micro-CT, excellent effort to improve my imaging knowledge, guidance in preparing and organizing manuscripts, in addition to all personal support over the two years. My deepest appreciation for helpful advice, much-needed coffee breaks, and his patience.

Finally, and most importantly, I would like to thank my parents (Katy and Mehdi), who have helped me a lot to stay grounded and encouraged me during all the challenging times; much of the time over the past two years, we were not in the same country, but I always had their unconditional love and support as I completed this work. There is great comfort in knowing they appreciate science as much as I do. I would also want to thank my beloved brother (Sina) for all the unique and beautiful memories that he made in my life. He always believed in me, and that made me believe in myself and stand for our dreams.

List of Abbreviations

ODRI	Orthopedic device-related infection
PJI	Peri-prosthetic joint infection
PMMA	Poly (methyl methacrylate)
MIC	Minimum inhibitory concentration
TJR	Total joint replacement
MSIS	Musculoskeletal Infection Society
CPR	C-reactive protein (CPR)
AAOS	American Association of Orthopedic Surgeons
MRI	Magnetic resonance imaging
CT	Computed tomography
MRSA	Methicillin-resistant <i>Staphylococcus aureus</i>
IV	Intravenous
PBS	Phosphate-buffered saline
UV	Ultraviolet
HPLC	High-performance liquid chromatography
MS	Mass spectrometry
ZOI	Zone of inhibition
Da	Dalton

3D	Three-dimensional
HU	Hounsfield Unit
2D	Two-dimensional
GE	General electric
CAD	Computer aid design
PLA	Polylactic acid
OD	Outer Diameter
H	Height
WT	Wall Thickness
FOV	Field-of-view
Al	Aluminum
BHC	Beam hardening correction
ROI	Region of interest
VOI	Volume of interest
PDE	Probability distribution equation
SNR	Signal-to-noise ratio
TPMS	Triply periodic minimal surface
ADEISS	Additive DEsign in Surgical Solution
FEM	Finite element method
CFD	Computational Fluid Dynamics

Table of Contents

Abstract.....	ii
Summary for Lay Audience.....	iii
Co-Authorship Statement.....	iv
Acknowledgments.....	v
List of Abbreviations	vi
Table of Contents.....	viii
List of Tables	xii
List of Figures.....	xiii
Preface.....	xviii
Chapter 1	1
1 Introduction to Orthopedic Device-Related Infection.....	1
1.1 Peri-Prosthetic Joint Infection.....	3
1.1.1 Definition	3
1.1.2 Risk Factors	3
1.1.3 Diagnosis.....	5
1.1.4 Biofilms.....	5
1.1.5 Treatment	6
1.2 Antibiotic Carriers	8
1.2.1 Poly methyl methacrylate (PMMA).....	8
1.2.2 Calcium Sulphate and Calcium Phosphate	9
1.3 Characterization of Antibiotic Elution.....	11
1.4 Thesis Objectives	14
1.5 Scope of Thesis	15

1.6	References.....	17
Chapter 2	22
2	Quantitative, non-invasive micro-CT imaging technique to characterize small-molecule diffusion.....	22
2.1	Introduction.....	23
2.1.1	Micro-CT Imaging.....	24
2.1.2	Beam Hardening.....	29
2.2	Materials and Methods.....	30
2.2.1	Contrast Agent.....	30
2.2.2	Experimental Design.....	30
2.2.3	Phantom Molds.....	32
2.2.4	Phantom Preparation.....	34
2.2.5	Image Acquisition.....	35
2.2.6	Beam Hardening Correction.....	36
2.2.7	Image Analysis.....	39
2.2.8	Calculation of Diffusion Coefficient.....	42
2.3	Results.....	45
2.3.1	CT Measurements.....	45
2.3.2	Diffusion Visualization.....	45
2.3.3	Quantitative Analysis of Line Profiles.....	48
2.3.4	Calculation of Iohexol Concentration.....	50
2.3.5	Diffusion Coefficient Calculation.....	51
2.4	Conclusion.....	53
2.4.1	Image-based Diffusion Characterization.....	53
2.4.2	Limitations.....	54
2.4.3	Applications.....	54

2.4.4	Summary	56
2.5	References	57
Chapter3	60
3	Mechanical Properties and Diffusion Characterization of Highly Porous 3D-printed Scaffolds.....	60
3.1	Introduction.....	60
3.1.1	Gyroid-based Structures.....	62
3.1.2	Selective Laser Melting	65
3.1.3	Finite element method.....	66
3.2	Material and Methods	66
3.2.1	Design of Porous Gyroid-based Cylinders	66
3.2.2	Finite Element Analysis of Gyroid-based Cylinders	69
3.2.3	Additive Manufacturing of Gyroid Cylinders.....	72
3.2.4	Diffusion Characterization Within the Gyroid-based Cylinder	74
3.3	Results.....	77
3.3.1	Finite Element Results	77
3.3.2	Gyroid-based Cylinder Fabrication.....	82
3.3.3	Diffusion coefficient Calculation.....	82
3.4	Conclusion	84
3.4.1	Mechanical and Diffusion Characterization of a Porous Scaffold.....	84
3.4.2	Limitations	85
3.4.3	Implications and Future Applications	87
3.4.4	Summary	88
References	89
Chapter 4	93
4	Conclusion and Future Directions.....	93

4.1 Summary	93
4.2 Future Directions	96
4.3 References	101
Curriculum Vitae	104

List of Tables

Table 2.1: CT numbers measured within each phantom. Custom volumes of interests (VOIs) were selected at first the scan time (<i>i.e.</i> , 1.25 hours after phantom fabrication) within each diffusion phantom.....	45
Table 3.1: Gyroid-based cylindrical scaffolds (17 mm diameter and 40 mm length) with varying porosity ranging from (60-90%).....	69
Table 3.2: Calculated displacement and effective elastic moduli of gyroid-based cylinders with varying porosity ranging from (60-90%). All samples were tested under 10 KN compression load in ABAQUS software. G00 is the solid cylinder of 17 mm ×40 mm out of Ti6Al4V.....	80
Table 4.3: Iohexol diffusion coefficient (m^2/s) through various cylindrical core carriers to the annular, agar tissue-equivalent, sink. The diffusion coefficients were obtained by fitting the CT-image data to the diffusion mathematical models.	96

List of Figures

- Figure 1.1: Modifiable risk factors associated with peri-prosthetic Joint infection. Patient age, obesity, frailty, and smoking history, among other risk factors, have been associated with increased short-term complications. 4
- Figure 1.2: Two-stage revision surgery in chronic PJI treatment. Stage I is to eradicate infection; during stage I, the infected implant is removed, and local antibiotic treatment is performed along with systemic therapy to eradicate infection. Temporary antibiotic carriers are used at this stage for local treatment; after infection is eliminated, temporary spacers are removed, and a new revision prosthesis is implanted. (Adapted from Suhardi, Bichara et al. 2017)..... 8
- Figure 2.1: Principle of cone-beam CT scanner. Object is irradiated by the X-ray beam and the attenuated X-rays are collected by a flat panel detector, providing a single two-dimensional projection. The gantry rotates by a small defined increment angle; at the next angular position another projection is acquired. Subsequently numerous 2D projections are collected over various angles around the object to construct a volumetric image..... 27
- Figure 2.2: GE eXplore speCZT. Located at Robarts Research Institute, it is a cone-beam micro-CT imaging system which we used in this work to characterize diffusion of contrast agent drug surrogate (Iohexol) 28
- Figure 2.3: Cupping artifact, Beam hardening results in cupping artifact (a) not corrected, (b) corrected. The x-ray beam becomes harder in the center of the homogenous material because it is the thicker than the periphery. The centre is erroneously assigned a lower gray value (CT number)..... 29
- Figure 2.4: Two-part intact phantom – A schematic diagram of the diffusion phantom, showing the finite-source (30 mg/ml Iohexol) “core” carrier material (agar or CaSO₄ matrices) in red and the tissue-equivalent “sink” in grey into which the drug-surrogate contrast agent diffuses during the longitudinal micro-CT imaging experiments. 31

Figure 2.6: Molds and final assembled diffusion-phantom (a) a two-part, 3D-printed, “negative” mold used for making the silicone-elastomer, inner-core mold; (b) two-part, silicone-elastomer mold used for pouring the inner-core carrier; (c) Iohexol-loaded, inner-core carrier, Stimulan matrix containing the drug-surrogate; (d) 3D-printed, PLA container mold for housing the phantom showing the lid with air- and water-calibration chambers, sealing-screws, and o-rings; (e) final, assembled, diffusion phantom showing the inner-core carrier surrounded by the agar tissue-equivalent sink into which the contrast-agent drug-surrogate diffuses..... 33

Figure 2.5: Phantom container-mold – CAD drawing of the 3D-printed, PLA, container-mold showing the (a) air and (b) water linear-calibration chambers in the phantom lid; (c) the central alignment ring in the base for accurate placement of the carrier core; and (d) the lateral ridges for rotational orientation. 33

Figure 2.7: Beam hardening correction. Iohexol loaded Stimulan[®] core in agar scanned on SpeCZT (90 kVp, 40 mA), 1.25 hrs after fabrication, with CT axial slice and corresponding diametric line profiles in the same axial CT slice. (a) no beam hardening correction (b) with beam hardening correction. Cupping artifact caused under estimation of attenuation (CT transmission ratio) within inner core Iohexol loaded matrix. CT numbers represent relative Iohexol concentration. 37

Figure 2.8: Al Calibration phantom for beam hardening correction in micro-CT and corresponding transmission image. (a) Al phantom was fabricated in house in different thickness by gluing disks of various diameters together in an alternating fashion. (b) Projection image from the scanner, obtained at 90 kVp and 40 mA. 38

Figure 2.9: Plot of aluminum calibrator phantom thickness vs. gray-scale values. We selected relative thickness of Al phantom based on the range of our data (maximum Iohexol transmission ratio) and fitted a one phase (inverse) decay to acquired data points at the application range. The fitted function parameters were then used to create a look-up table to re-linearize the data. 39

Figure 2.10: CT numbers calibrators. Custom regions of interest (ROIs). in (a) air chamber and (b) water-filled pocket within the phantom's lid to measure corresponding signal intensity of air and water for calibration purposes. 40

Figure 2.11: Spatially averaging axial CT slices. Demonstrates SNR of a diametric line profile through the Iohexol-loaded Stimulan[®] core in agar (a) 0.1 mm spatial voxel spacing (b) 0.1 mm in-plane and 5.0 mm axial spacing and radially averaged. Increase in signal-to-noise (SNR) ratio is observed in averaged slices in z-axis..... 41

Figure 2.12: CT slices of Iohexol loaded agar cylindrical core in agar. Diffusion process of Iohexol contrast agent drug surrogate was characterized by down-gradient propagation, spreading and smoothing over time (a) 1.25 hrs, (b) 5.08 hrs (c) 8.08 hrs (d) 18.08 hrs (e) 47.58 hrs (f) 76.08 hrs after phantom fabrication. CT axial slices showed almost uniform concentration of Iohexol after 76.0 hrs. 46

Figure 2.13: CT slices of Iohexol loaded Stimulan[®] cylindrical core in agar. Iohexol contrast agent drug surrogate diffuses slowly from the core into pure agar, contrast agent diffuses from the core primarily over the first 120 hours and remains relatively stable between 435 and 600 hours. a) 1.25 hrs, (b) 8.25 hrs (c) 24.0 hrs (d) 70.25 hrs (e) 121.50 hrs (f) 607.25 hrs after phantom fabrication. 47

Figure 2.14: Two-dimensional (2D) diametric line profiles within an axial CT slice. (a) Iohexol loaded Stimulan[®] cylindrical core and (b) Iohexol Loaded Plaster cylindrical core surrounded by pure agar sink phantom at different time points. Iohexol contrast agent drug surrogate diffused from core into agar periphery. Diffusion from the core was reduced to a negligible value approximately 145 hrs after phantom fabrication. ... 49

Figure 2.15: Two-dimensional (2D), diametric, line profiles through an axial CT slice in Iohexol-loaded cylindrical agar core surrounded by a pure agar sink at various time points. Iohexol contrast agent drug surrogate diffused from the agar core into agar periphery. The gradient of Iohexol concentration observed within phantom was significantly reduced 76.0 hrs after phantom fabrication. 50

Figure 2.16: Linear regression plot of radial diffusion distance vs. time. The slope of the line represents $4D$ in two-dimensional diffusion. The derived diffusion coefficient was equal to $2.26 \times 10^{-10} \text{ m}^2 \text{ s}^{-1}$ 51

Figure 2.17: Plot of the cumulative release of Iohexol contrast agent vs. time, (a) Iohexol-loaded Stimulan® in agar (b) Iohexol-loaded Plaster in agar. Diffusion coefficients of $0.46 \times 10^{-10} \text{ m}^2 \text{ s}^{-1}$ and $0.85 \times 10^{-10} \text{ m}^2 \text{ s}^{-1}$ for Iohexol incorporated in the Stimulan® and plaster cores, respectively. 52

Figure 3.1: Schematic of Gyroid-lattice structure, (a) shows one unit cell of a gyroid structure where d is the pore size, T is the wall thickness and L is the length, (b) The unit cell with the length of 6 mm that was used in this work (c) three-dimensionally volume rendering of a unit cell forming a cylindrical structure of 17 mm diameter \times 40 mm length. 64

Figure 3.2: load-bearing surfaces of a gyroid-based cylinder at various cross sections. Various cross-section shapes viewed from in plane shift of the two-dimensional cross-section. The area fractions occupied by the structure are approximately the same for all cross-sections. 64

Figure 3.3: 3D rendering of Gyroid cylinder of 17 mm diameter and 40 mm length. Unit gyroid cell of 6mm in length was repeated to create a cubic lattice, followed by a Boolean intersection operation to achieve a cylindrical design using open-source design software (Blender 2.78 3D software). 68

Figure 3.4: Top surface of gyroid-based cylinders of 17 mm diameter and 40 mm length with various porosity. Renderings illustrate altering of the wall thickness and porosity: G00) 0%, G01) 60%, G02) 70%, G03) 80%, G04) 85%, G05) 90%. All gyroid-based cylinders were designed by periodically repeating a unit cell of 6 mm in length in 3 principal spatial directions (x,y,z). 68

Figure 3.5: Compression load and boundary condition of the gyroid-based cylinder. A uniform distributed load of 10 KN was applied on a stainless-steel plate, the boundary condition for the plate is displacement-rotation and only one-degree freedom is allowed

in the load direction. The cylinder is fully-constraint at the bottom, while expansion of lateral surfaces is free to occur.....	70
Figure 3.6: Finite element mesh of a gyroid-based cylinder. The cylinder was discretized by linear, 4-node tetrahedral elements	71
Figure 3.7: Schematic of gyroid-based cylinders of 17 mm diameter and 40 mm length with various porosity on the 3D-printer build-plate. G00) 0%, G01) 60%, G02) 70%, G03) 80%, G04) 85%, G05) 90%. The cylinders are attached to the build platform through support structures of 400 μm. Support filaments are built using the same Ti6Al4v powder to avoid warping and distortion that may occur due to the high processing temperatures.....	74
Figure 3.8: CT volume of gyroid-based cylinder with 80% porosity (G03) acquired by isosurface volume rendering after beam hardening correction (BHC). The images on the right show that the correction algorithm has resulted in significant reduction of metal artifacts.....	77
Figure 3.9: : Maximum Von Mises stress and regions with high-stress values at outer surface. (a) the maximum stress value was observed at the edge of the top surface due to the limitation in mesh sizing. (b) there were regions with no underlying support at the outer surface that exhibited artifactually higher stress values due to design limitations, these numbers do not represent the strength of structure and were eliminated in this work. ..	78
Figure 3.10: 3D-printed gyroid-based cylinders (17 mm length × 40 mm diameter) with varying porosity values G00) 0% G01) 60 G02) 70% G03) 80% G04) 85% G05) 90%. A 3D-metal printer (AM400, Renishaw plc, UK) was used with laser power of 400W and laser spot size of 70 μm.....	82
Figure 3.11: Plot of the cumulative release of Iohexol contrast agent vs. time. Contrast agent was embedded in plaster and was loaded into a gyroid-based cylinder of 80% porosity (<i>i.e.</i> , G03) and surrounded with an annulus of pure agar. The image data were fitted to the equation for a cylindrical geometry drug delivery carrier; a diffusion coefficient of $0.50 \times 10^{-10} \text{ m}^2/\text{s}$ was calculated.	83

Preface

This work is dedicated in memory of Sina Khazae.

Chapter 1

1 Introduction to Orthopedic Device-Related Infection

This thesis addresses unmet needs related to orthopedic device-related infections (ODRI), which includes infections near fracture-fixation components that are used during trauma surgery [1-4], as well as peri-prosthetic joint infections (PJI) near orthopedic components (such as hip and knee replacements) [5-8]. Infections – along with component wear and loosening – are a major cause of surgical revision of total joint replacements (TJR) [9]. While significant improvements in orthopedic surgical devices have reduced the risk of mechanical failure in trauma and joint replacements, relatively little progress has been made in the area of infection and mainly PJI [9]. PJI is one of the most common reasons for early revision (within five years of primary surgery) of both hip and knee replacements[10]. In North America, orthopedic surgical site infections affect over 100,000 people each year [11, 12]. In the US, recent data show that the percentage of knee arthroplasty revision surgeries due to infection has grown from 13% in 2012 to 22% in 2018 [13]. Infection can lead to catastrophic complications, including severe, residual disability, limb amputation, and death; PJI doubles the risk of in-hospital mortality [14].

Infection is a growing problem in orthopedic surgery. It is now the number one reason for early revision of hip and knee replacements in Canada [10]. The number of total knee and hip joint replacements continues to rise in Canada, with a 17% increase in the number of arthroplasties performed over the past five years [10]. Unfortunately, 9700 (or 7%) of these surgeries are implant revisions, which are more complex than primary surgeries and result in longer recovery time and much higher procedure costs [10]. In the 2018 International Consensus Meeting (ICM) on musculoskeletal infection [10, 15], it has been concluded that “*Musculoskeletal infections remain the bane of orthopedic surgery, and result in grievous illness and inordinate costs that threaten healthcare systems; ... prevention, diagnosis, and treatment has remained largely unchanged over the last 50 years*” [10].

Patients who are diagnosed with PJI undergo revision surgery to replace an infected implant with a new revision prosthesis. Revision surgery is challenging, and includes multiple stages spanning several months. Revision surgery is also typically 5 to 10 times more expensive

than the initial surgery, making PJI a significant burden for the health care system. Additionally, most patients do not return to previous levels of activity after multiple revision surgeries, and there is also a considerable drop in the patient's quality of life after infection treatment and revision surgery due to PJI [16].

Total joint replacement implants are made mainly of bio-compatible, metal components which carry a risk of foreign-body immune reaction near the prosthesis. Previous work in animal models has shown that in the presence of a foreign body, the bacterial concentration required to induce an infection is reduced by more than a factor of 100,000 [17], making the risk of infection a very significant concern. Infection susceptibility is also dramatically increased in the presence of a foreign body due to the establishment of a biofilm on the foreign body surface that protects bacteria from host immune system defense [18]. This protective environment makes PJI particularly tenacious and difficult to treat with systemic antibiotics.

The current gold standard treatment for PJI is two-stage revision surgery: the first removes the infected implant and treats infection; the second installs the final revision prosthesis. During the first stage, following implant removal, a surgeon places temporary antibiotic-loaded cement spacer for local antibiotic delivery that targets the joint, in addition to systemic infection treatment to ensure complete infection eradication. Unfortunately, the mechanism of action for local antibiotic delivery is poorly characterized and local antibiotic treatment is associated with relatively poor clinical outcomes. Elution of antimicrobial agents through commonly employed carriers, such as Poly (methyl methacrylate) (PMMA) manifests as a rapid, initial diffusion phase, followed by a subsequent significant decrease. This decrease may even lead to a drop in the antibiotic level below the bacterial minimum inhibitory concentration (MIC), resulting in further bacterial resistance within the infected joint, making treatment still more challenging. Current antibiotics carriers exhibit poor diffusion characteristics. There is a distinct need to understand the diffusion mechanism better and enhance infection treatment through local drug delivery in PJI.

1.1 Peri-Prosthetic Joint Infection

1.1.1 Definition

PJIs are classified as either chronic or acute. Acute PJI symptoms occur within 3-6 weeks after primary joint replacements and are mainly due to direct contamination caused primarily by highly virulent microorganisms [19]. Chronic PJI symptoms appear after six weeks following primary joint replacement and are caused by low-virulence pathogens. There is also a risk of late infection – more than two years after surgery – reported to be mainly due to blood-borne dissemination [20]. Chronic and late infections are more challenging to differentiate from mechanical loosening, since as the infection progresses, it may produce similar symptoms, such as implant loosening [9, 19].

The definition for PJI has dramatically improved diagnostic confidence among surgeons. Musculoskeletal Infection Society (MSIS) has defined PJI as "*a sinus tract (i.e., tunneling wound) communicating with the prosthetic joint or two positive cultures with phenotypically identical organisms from the peri-prosthetic tissue or fluid samples.*" Culture results may also be supported by the presence of pre-operative and intra-operative minor criteria, such as: elevated C-reactive protein (CRP); high synovial fluid white blood cell count; or positive histological analysis of peri-prosthetic tissue [19, 20]. A further Consensus Meeting in 2013 endorsed the MSIS definition and modified it slightly to improve diagnostic confidence; adding supportive evidence for absolute infection diagnosis and resulting in more accurate guidelines for diagnosis. This includes developing a functional definition of “Acute” versus “Chronic” PJI based on intra-operative findings (*e.g.*, single culture growth, and positive histology)[10]. Patients are classified as having a PJI if they meet the diagnostic criteria as proposed by the MSIS and endorsed at the consensus meeting.

1.1.2 Risk Factors

PJI is most common in the first five years after primary joint replacement, however, it can present at any time during the patient’s lifetime [10]. Many different risk factors are associated with infected joints and increased short-term complications [10, 23]: patient age; obesity, frailty, and smoking history, among others. Patients with a history of PJI or multiple surgeries on the same joint should also be considered to be at high risk [21, 24]. Patients with

symptoms such as continuous pain or stiffness in the revised joint may also represent a higher probability of infection [21, 24]. In general, some modifiable risk factors make patients more susceptible to developing PJI after primary joint replacement. A diagram representing overall risk factors for joint infections was published by the American Academy of Orthopedic Surgeons (AAOS) in 2009. (Fig 1.1)

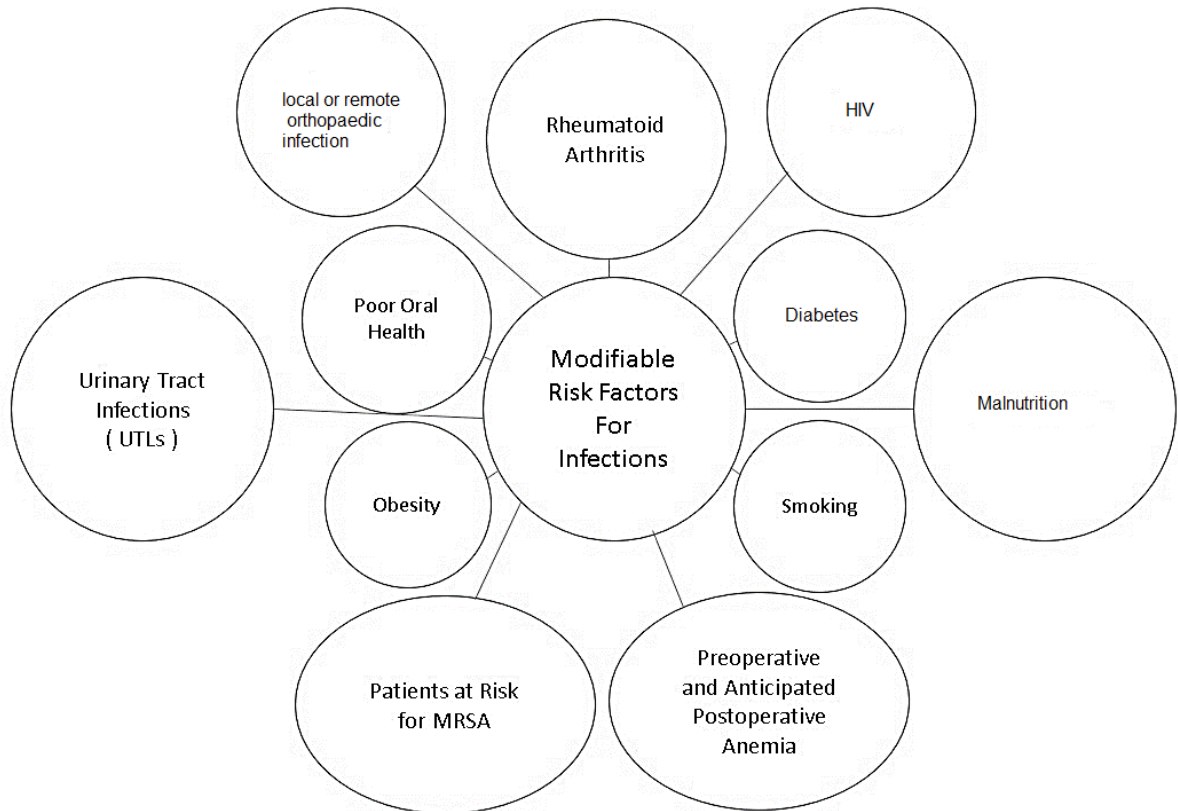


Figure 1.1: Modifiable risk factors associated with peri-prosthetic joint infection. Patient age, obesity, frailty, and smoking history, among other risk factors, have been associated with increased short-term complications.

[Adapted from Orthopedic Infection prevention and control, AAOS 76th meeting report, 2009].

1.1.3 Diagnosis

Accurate and efficient diagnosis of PJI is a challenge for clinicians, and there is still no absolute “gold-standard” available [9]. Significant evidence of PJI is identical, and supportive evidence is often required [11]. PJI is typically diagnosed *via* a combination of clinical, laboratory, and intraoperative findings. Imaging techniques can also be applied for PJI diagnosis. While magnetic resonance imaging (MRI), computed tomography (CT), and nuclear imaging are not considered direct approaches for PJI diagnosis, they can be used to identify symptoms that are associated with infection in complicated cases [21]. Cyteval *et al.* reported the application of CT to diagnose infection in hip, joint replacements. Some CT findings, like peri-prosthetic fluid collection and joint distention, could be used to identify PJI in the hip joint. Still, we may not be able to employ CT generally as a direct, diagnostic tool for other joint infections [22]. MRI suffers from magnetic susceptibility artifacts near metal implants, making PJI diagnosis challenging [23]. Among all imaging modalities, nuclear medicine is often considered as a useful imaging technique for PJI diagnosis. This imaging method has been used since the 1970s; however, these tests have limitations, in case of sensitivity and accuracy. For example, bone scintigraphy is sensitive but not specific when there are osseous abnormalities present. There is also typically a 1-3 day interval between injection of the radiopharmaceutical and imaging [24].

1.1.4 Biofilms

The risk of infection in total joint replacements was described first by Gristina in 1987 [25]. Prosthetic implants will, ideally, function successfully for many years, making implant surfaces potential interfaces on which individual bacteria can attach and eventually form a biofilm, potentially resulting in PJI. The biofilm phenotype can describe chronic PJI. They are mainly caused by the very rapid growth of bacteria [18]. Bacteria that are noted to cause peri-prosthetic infection include coagulase-negative staphylococci (30–43%), *Staphylococcus aureus* (12–23%), streptococci (9–10%), enterococci (3–7%), gram-negative organisms (3–6%) or anaerobes (2–4%) [26]. Staphylococci (specifically *S. aureus* and *Staphylococcus epidermis*) are the most common biofilm-forming bacteria in PJI [27].

In biofilm formation, bacteria adhere to the implant surface in a highly hydrated extracellular matrix. The microorganisms within biofilms form complex, highly organized communities

[20] that are metabolically inactive and up to 1000 times more resistant to antibiotics than systemic bacteria. Biofilms act as a protection layer against body immune response and antibiotic penetration [28]. To completely eradicate biofilm-related bacteria, a much higher concentration of antibiotics is required [29], making this problem notoriously tricky. Concerns of systemic toxicity to the patient prevents clinicians from performing high-dose, systemic antibacterial treatment. The most widely used antibiotics used in PJI are gentamicin, tobramycin, and vancomycin [30].

Methicillin-resistant *Staphylococcus aureus* (MRSA) has been reported to play a vital role in biofilm formation in peri-prosthetic joint infection [18]. The increasing prevalence of MRSA in orthopedic infection makes current treatment even more complicated. MRSA bacteria strains exhibit tolerance to antibiotics [18] by adhering to the implant, becoming sessile (immobile), reducing their metabolic rate, and secreting a protein layer that protects them from antibiotics. Biofilm-covered colonies then act as a reservoir for MRSA [31]. Moreover, biofilms that are exposed to a level of antimicrobial agent below a certain concentration have been shown to increase the development of biofilm formation and increase the likelihood of further bacterial resistance [32]. This minimum inhibitory concentration (MIC) is defined as the lowest concentration of antimicrobial agent that prevents bacteria growth [33]. There are different methods available for measuring MICs of different microorganisms against antimicrobial agents [34]. Thus, orthopedic implants exhibiting chronic infection caused by MRSA must be removed. In a study of 117 patients with PJI, Cobo *et al.* [35] reported that patients infected with MRSA had the highest rate of failure, even after two-stage revision surgery. There is a high risk of infection recurrence after implanting the revision prosthesis, if even a minimal amount of bacteria has been retained. Reducing the threat of antibiotic-resistant biofilms is a very active area of interest in recent years.

1.1.5 Treatment

Due to the projected burden of PJI to the health care system and individuals, an efficient and safe strategy is required for treatment. Antibiotic therapy is a common general strategy to treat chronic/acute PJI with a combination of surgical approaches. In acute PJI, clinicians typically perform systemic antibiotic therapy and monitor the patients until the infection has been eliminated, based on MSIS guidelines. The PJI patient then will undergo single surgery

for debridement of necrotic and granulation tissue and exchange of the polyethylene spacer in order to ensure that no bacteria remain in the infected joint. These approaches have been reported to have a success rate that ranges between 31-78% [36].

For patients with chronic PJI, the current gold standard is two-stage revision surgery (Fig 1.2). In stage 1, the objective is to eradicate infection. Primary components are removed, and patients undergo both systemic and local antibiotic therapy to ensure complete eradication of infection. Clinicians typically take advantage of antibiotic carriers for local treatment, combined with systemic therapy for 6-8 weeks, during which time patient serum concentration is tracked to monitor infection level. After the infection is fully cleared, stage 2 is implemented to maintain joint biomechanics. During this surgery, temporary components are removed, and a revision prosthesis is implanted after final debridement of surrounded tissue.

Culture-directed intravenous (IV) antibiotics are commonly used for systemic therapy, however, systemic treatment of infection with antibiotics should be limited to a certain level, due to toxicity and potential damage to other body organs [31]. Systemic toxicity is a barrier to performing high-dose systemic antibacterial treatment clinically. Reduced blood supply at the site of infection also reduces the efficacy of systemic therapy [36]. Therefore, local drug delivery is employed as an adjunct treatment to systemic therapy during Stage I. Antimicrobial agents can be delivered locally to the surgical site *via* acrylic-based, non-biodegradable cements (*e.g.*, PMMA) or biodegradable, mineral-based bone cement (*e.g.*, calcium sulfate or calcium phosphate). Local drug delivery also offers the potential for controlled release over an extended time from novel release devices.

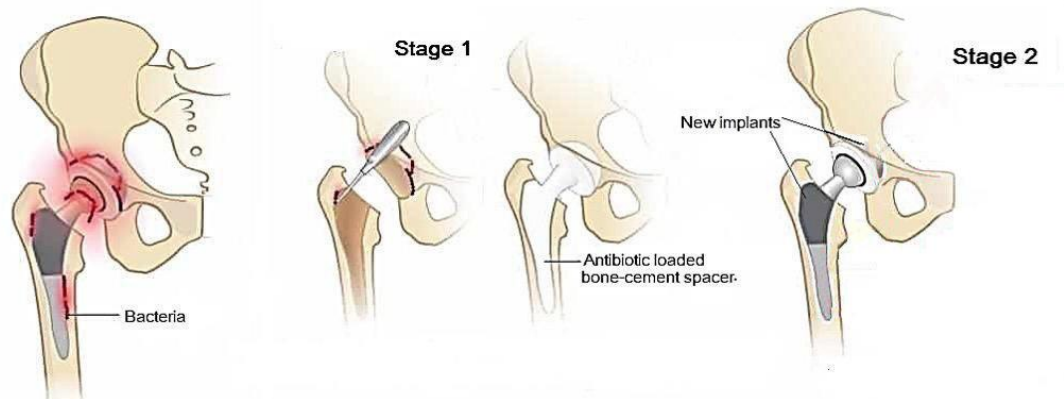


Figure 1.2: Two-stage revision surgery in chronic PJI treatment. Stage 1 is to eradicate infection; during Stage 1, the infected implant is removed, and local antibiotic treatment is performed along with systemic therapy to eradicate infection. Temporary antibiotic carriers are used at this stage for local treatment; after infection is eliminated, temporary spacers are removed in Stage 2, and a new revision prosthesis is implanted. (Adapted from Suhardi, Bichara et al. 2017)

1.2 Antibiotic Carriers

1.2.1 Poly methyl methacrylate (PMMA)

The use of PMMA as a bone cement spacer compound was first introduced by Buchholz Engelbrecht for local drug delivery in PJI in 1970 [37]. Antimicrobial agents can be added to temporary spacers during the industrial manufacture of the bone cement, or with manual blending upon preparation within the operating room. Pre-mixed bone-cement spacers have also been available since the 1990s [38]. Bone-cement spacers aim not only to deliver higher dose antibiotic concentration to target tissue than systemic administration, but also to manage and maintain the joint space after removal of the primary implant.

PMMA is an acrylic, dense, and non-absorbing material; although it is widely used in two-stage revisions, there are several drawbacks associated with its application. It usually must be removed in stage II of PJI treatment after fulfilling its function as a carrier for antibiotics and a mechanical spacer within the joint [39]. If PMMA spacers remain for more extended

periods without the placement of new revision implants, they have shown a complication rate of 26–60 % within 49–54 months, mainly due to dislocation (11–17 %) and fracture (10–14 %) [40]. PMMA also polymerizes during mixing of the powder polymer with a liquid monomer and generates high temperature due to an exothermic reaction; thus, it is not an ideal carrier choice for heat-sensitive antibiotics [39]. Moreover, due to poor mechanical properties of PMMA, antibiotic concentration in these spacers is limited by the minimum allowed mechanical properties. High-dose antibiotic-impregnated PMMA demonstrates an increased risk of mechanical failure due to a drop in mechanical properties [41]. Hanssen *et al.*, classified antibiotic-loaded bone cement spacers into high dose (>2 g antibiotic per 40 g cement) and low dose (<2 g antibiotic per 40 g cement) and recommended high dose for use as beads in trauma-related infections and low dose for joint replacement prosthesis [42, 43].

Local treatment is an essential factor in infection eradication during stage I. PMMA exhibits relatively poor antibiotic elution kinetics. In fact, it is likely that only 10% of the antibiotic is eluted from PMMA bone cement due to its hydrophobicity [44]. Elution kinetics are often defined as a ‘burst’ release of antibiotics over the first few days (7–10), followed by an exponential drop over time [45]. This leads to the potential for sustained periods where local antibiotic concentration falls below the MIC level [39]. Most studies agreed on a burst release followed generally by an exponential decay in eluted antibiotic concentration from PMMA carriers (*i.e.*, biphasic release) [46–48]; thus, there is an absolute need for a new approach to characterize antibiotic elution and develop materials and structures to deliver high-dose antimicrobial agents consistently over a more extended period.

1.2.2 Calcium Sulphate and Calcium Phosphate

Calcium phosphate and calcium sulphate cement have been used for the treatment of bone defects for more than one hundred years [49]. While PMMA bone-cement spacers are used for high and medium load-bearing applications, calcium phosphate and calcium sulphate are generally used for medium and low load-bearing applications. They are also a good choice for drug delivery and are employed as antibiotic carriers in orthopaedic trauma infections [49]. Whereas PMMA allows a small amount of antibiotic to release, these calcium-based biomaterials eventually release their entire load of antibiotics due to their inherent biodegradability [44]. They also provide much higher elution efficiency of antibiotics

through diffusion. The elution is taking place over a more extended period, which may help to maintain complete bacteria eradication during the intermediate stage of PJI treatment [30].

Calcium phosphate is usually a mix of two main components; one is the powder that is basically a combination of different calcium phosphate salts, and two is the liquid, which is a sodium phosphate solution. The paste would be prepared by mixing two components in the operating room. The mixture would set in 2-7 minutes. After the paste hardens, it is very similar to the mineral phase of the bone. Calcium phosphate will remain several years after implantation, and its resorption rate is very slow. Unlike PMMA bone cement, calcium phosphate is visible in x-ray images without any need to add contrast agents. Calcium phosphate exhibits mechanical properties that range between cancellous and cortical bone in compression (*i.e.*, compression strength 17 MPa for calcium phosphate); however, it is lower than cancellous bone in tensile and shear strength [49]. Unlike PMMA, polymerization of calcium phosphate-based bone substitute is through hydration and generates a negligible heat that does not denature incorporated heat-sensitive antibiotics [44].

Calcium sulphate bone substitutes are biocompatible and resorb much faster than calcium phosphate, reported in the range of 40-70 days; however, the exact degradation rate depends on the size and implanted location of the calcium sulphate. Rapid resorption of calcium sulphate carriers increases the elution kinetics of antibiotics in local treatment. Resorption of the carrier would make more space for antibiotic molecules to diffuse from the carrier to target infected tissue, in other words, there are two mechanisms that combine to enhance drug delivery in local treatment: small molecule diffusion (*i.e.*, mass diffusion) and resorption [49]. There are some other factors *in vivo* that might affect the entire diffusion process (*e.g.*, carrier swelling, chemical reactions, loads). During preparation of calcium sulphate bone substitutes, powder and solution (which is mainly sterile water) are mixed and the crystallization process starts; this process does not create any exothermic reaction. This is an advantage over PMMA bone-cement carriers for the application of heat-sensitive antibiotics. Calcium sulphate also has inherently high radiographic attenuation, and there is no need to add any contrast agent. However, calcium sulphate has low mechanical strength; it is weak and brittle, with low compressive strength.

Although calcium sulphate carriers have been reported to exhibit superior elution characteristics compared to PMMA, their poor mechanical properties act as a barrier for application during an intermediate stage of PJI treatment as a replacement for current PMMA carriers. Calcium sulphate occurs in the di-hydrate form naturally. The hemihydrate form is produced by dehydration of the dihydrate by heating. There are two main compositions of calcium sulphate material available, characterized as either an α -form or β -form hemihydrate, depending on the method of heating. Conventional Plaster-of-Paris is the β -calcium sulphate hemihydrate. The α -form provides a stronger product than the β -form, mainly due to differences in the density [49]. High-purity, medical-grade, calcium sulphate (Stimulan® Rapid Cure, Biocomposites, Keele, U.K.) is a synthetic, recrystallized α -hemihydrate [50].

1.3 Characterization of Antibiotic Elution

Although local antibiotic treatment is widely used as a standard method to eliminate infection during the intermediate stage of PJI treatment, the exact mechanism of elution remains to be fully elucidated. As discussed earlier, antimicrobial agents can be delivered to the surgical site by temporary biocompatible carriers. These carriers can be either biodegradable or non-biodegradable. PMMA bone cement and mineral-based bone substitutes (*e.g.*, calcium sulphate and/or phosphate) are two commonly available delivery carriers. These carriers are routinely used to deliver antimicrobial agents to the target tissue and control infections related to trauma or PJI. There are also some recent advances in developing polymer-based biomaterials to be able to embed drug clusters in the polymer matrix. Drug-eluting polymers might enhance local drug delivery due to higher elution characteristics over an extended period, while maintaining mechanical strength to withstand loading [51, 52].

There is an undeniable demand to improve drug delivery in local treatment for ODRI. We first need to understand the elution mechanisms of antibiotics in local treatment. Several studies have focused on the characterization of antibiotic elution and their relative activity against the most common bacteria that are associated with PJI (*e.g.*, *Staphylococcus aureus*). Release of antibiotic from a carrier depends on several factors such as carrier porosity, antibiotic types and combinations, corresponding concentration ratio (*i.e.*, loading amount), carrier preparation techniques, carrier surface characteristics, dynamic or static environment, and also *in-vivo* circumstances, such as the effect of exposure to body fluids [48, 52].

A literature search was performed through PubMed to update our knowledge regarding methods that have been introduced to study elution characteristics of antibiotics in local treatment of ODRI. We can classify available literature into *in-vitro* and *in-vivo* studies. *In-vitro* characterization of elution is based on measuring local antibiotic concentration in a culture medium (*e.g.*, normal saline, phosphate-buffered saline (PBS), simulated body fluid) at various time points. The common methodology of *in-vitro* evaluation of elution characteristics is based on incorporating a known concentration of antimicrobial agents to a defined carrier, immersing the carrier in a solution, and finally, invasive-sampling of the solution at various time points to measure antibiotic concentration available within the solution. The antimicrobial agent concentration that is available in the solution at different time points is then used to describe the diffusion characteristic of that agent through the known carrier [39, 45, 53]. The amount of the solution in which antimicrobial agent is diffusing should be maintained at a level for invasive sampling, while ensuring full coverage of the antibiotic-loaded carriers; thus, the medium needs to be refreshed totally or partially after invasive-sampling at each time point. In this way, invasive sampling may affect the diffusion kinetics. The concentration of antimicrobial agents within the medium can also be measured by the application of different methods such as ultraviolet (UV) high-performance liquid chromatography (HPLC), UV spectroscopy, combined liquid chromatography-mass spectrometry (LC-MS), fluorescence polarization immunoassay, and a flow chamber technique for medium collection and disk diffusion assay [39, 45, 54-58].

There are some other methodologies described in the literature to study antibiotic elution. Merkhan *et al.* developed a technique to evaluate antibiotic concentration in PBS by measuring the relative pH. He hypothesized that the pH of the PBS medium is a function of antibiotic concentration that has been diffused into the solution. This study evaluated the release kinetics of gentamicin from PMMA cement [59].

Evaluating the zone of inhibition (ZOI) is another method to describe antibiotic elution characteristics seen in the literature. ZOI is defined as a circular area around the spot of the antibiotic in which the bacteria colonies do not grow. Although ZOI is mainly used to maintain the bioactivity of bacteria against different types and concentrations of antimicrobial agents, it can also be used to quantify the elution kinetics of antibiotics. For this methodology, a plate of medium is first seeded by known bacteria, and antibiotic-

impregnated carriers would then be placed on the plate. The plate can be assessed to evaluate the clearance zone around the carriers over time. The measurement of ZOI at various time points will represent how far antibiotics have been released [60] and so can be used to compare the diffusion rate within different carriers.

Along with molecular diffusion that is based on random motion of the molecules from a higher gradient to lower gradient levels, some other factors affect the elution characteristics from a specific carrier *in-vivo*. Rogers *et al.* reported the effect of loads on diffusion characteristics. They measured the antibiotic diffusion from PMMA knee spacers in phosphate buffer saline after performing cyclic loading on the phantom. They concluded that dynamic spacers would have a higher elution rate than static spacers, and loading will promote elution characteristics [61].

Kummer *et al.* described the effect of sonication on elution kinetics. They presented that PMMA has higher elution kinetics when combined with sonication over a particular period of time. However, the application of sonication to enhance elution from calcium sulphate/phosphate carriers remains unclear [62].

One drawback of the above methodologies is the invasive sampling of the medium. As described, a sample from a medium (*i.e.*, the solution in which antimicrobial agent is diffusing) is invasively collected at each time point. The concentration of the antimicrobial agent then measured within the collected sample to describe the diffusion of the antimicrobial agent. Antimicrobial-loaded carriers can also be washed out thoroughly and placed in a new fresh solution for the next time point sample collection. However, in the *in-vivo* environment, diffusion of the antimicrobial agent into the surrounding tissues is occurring in a diffusion-limited environment. There is some evidence that if we expose the antimicrobial-loaded carrier into fresh fluids, the elution kinetics may vary. Elution may cause a saturation of the surrounding medium in a controlled environment, and the gradient that supports the antimicrobial agent release at the beginning is expected to drop faster over time in the case of saturation [52, 63].

Dusane *et al.* studied the diffusion of antibiotic from PMMA and calcium sulphate carriers by using a diffusion-limited agar method to simulate *in-vivo* controlled environment. In this study, carriers were created and embedded in pure agar to track diffusion into a finite agar

sink (i.e., a reservoir that molecules can diffuse from the core into it). The agar gel diffusion method was used to evaluate bacteria bioactivity by measuring the ZOI over different time points [60]. A second study was performed by using a fluorescein optical tracer as a surrogate for antibiotics [47]. In this study, researchers loaded fluorescein tracer into the carriers as a surrogate for commonly available antibiotics. Fluorescein dye tracer is a freely water-soluble material that shows hydrophilic characteristics and can be used as a surrogate for antibiotics in order to study elution kinetics [64-66]. Fluorescent optical imaging techniques were used to monitor release kinetics and track the diffusion distance of fluorescein over time. Real-time images were taken by a gel documentation system, and the diffusion distance was observed in a solid hydrogel agar medium and calculated by standard image thresholding.

The release of antibiotics from actual-size knee and hip PMMA cement spacers has also been studied *in vivo*. These studies were performed either during the intermediate stage of PJI treatment (when a temporary spacer is implanted) or after removal of the spacer. Measuring a patient's serum antibiotic concentration over time was used to evaluate elution kinetics [67]. Pharmacokinetic properties *in vivo* at the time of spacer implantation was also determined by collecting synovial fluid from patients. The final concentration of antibiotics was obtained from the fluid joint at the time of spacer removal during intermediate stage surgery [52].

1.4 Thesis Objectives

The overall goal of this work is to characterize and improve local drug delivery in PJI management. Although local antibiotic delivery is commonly used in PJI treatment, the exact diffusion mechanism is not fully understood. There is an obvious need to better understand antibiotic diffusion in local drug delivery, and subsequently deliver high dose antibiotics to the target tissue with the desired diffusion rate over an extended period (while maintaining necessary mechanical properties).

The specific objectives of this work are:

1. Development of a quantitative, non-invasive, longitudinal micro-computed tomography (micro-CT) imaging technique to characterize the diffusion of small molecules from a finite-source carrier to a finite tissue-equivalent phantom sink.
2. Design and fabrication of a 3D-printed metal porous scaffold and investigation of the application of highly porous structures in the development of drug-delivery systems. A highly porous metal scaffold can separate the competing needs for mechanical strength by providing structural support while maintaining appropriate drug-elution characteristics.

1.5 Scope of Thesis

Chapter 2: quantitative, non-invasive micro-CT imaging technique to characterize small-molecule diffusion.

Given the introduction to PJI, current standard treatment, and previous literature, there is considerable evidence that the exact antibiotic elution mechanism from bone cement spacers is not yet well understood. We believe that a new approach is required in order to make significant progress in local drug delivery in PJI treatment. A micro-CT imaging technique can be used to characterize small-molecule diffusion. In this chapter, we demonstrate the development of a non-destructive, non-invasive, longitudinal image-based method to track the diffusion of a drug surrogate contrast agent over time. The concept of using drug surrogate is not new; fluorescein has been used as an optical tracer to study elution in calcium sulphate and PMMA previously [47]. However, in this research, we use an x-ray contrast agent (Iohexol) with a molecular weight of 821 Da, which is much closer to that of commonly used antibiotics like Vancomycin with a molecular weight of 1449 Da compared to fluorescein with molecular weight of 332 Da.

Chapter3: mechanical properties and diffusion characterization of highly porous 3D-printed scaffolds

In this chapter, we aim to design and fabricate a 3D-printed titanium-alloy porous structure and investigate the concept of a highly-porous metal scaffold containing antibiotic-eluting

carriers. Our structure aims to deliver high-dose antibiotics with calcium-sulphate carriers. Calcium sulphate carriers provide superior elution kinetics compare to PMMA, and the proposed porous structure would maintain the necessary mechanical properties.

We based our scaffold design on a gyroid-based structure. The gyroid provides the advantage of a highly porous, open structure without significant stress concentrations [68]. Gyroid parameters (*i.e.*, unit-cell size and wall thickness) can be modified parametrically, providing control over the porosity and hence mechanical strength. We modified the parameters for the gyroid-based design over the range of 60 to 90% porosity; these values fall within the range that can be fabricated in metal using 3D printing. Cylindrical gyroid-based scaffolds with 80% porosity were selected to perform a diffusion experiment and characterize the diffusion of Iohexol contrast agent drug-surrogate using micro-CT within the presence of the metal scaffold. The long-term goal in this work is to develop more effective drug-eluting implants, potentially removing the need for two-stage revision surgery.

1.6 References

1. Qiu, X.S., et al., *Coating the plate with antibiotic cement to treat early infection after fracture fixation with retention of the implants: a technical note*. BMC Musculoskelet Disord, 2018. **19**(1): p. 360.
2. Moriarty, T.F., et al., *Orthopaedic device-related infection: current and future interventions for improved prevention and treatment*. EFORT Open Rev, 2016. **1**(4): p. 89-99.
3. Metsemakers, W.J., et al., *Influence of implant properties and local delivery systems on the outcome in operative fracture care*. Injury, 2016. **47**(3): p. 595-604.
4. Raschke, M., T. Vordemvenne, and T. Fuchs, *Limb salvage or amputation? The use of a gentamicin coated nail in a severe, grade IIIc tibia fracture*. Eur J Trauma Emerg Surg, 2010. **36**(6): p. 605-8.
5. Hutzler, L. and J. Williams, *Decreasing the Incidence of Surgical Site Infections Following Joint Replacement Surgery*. Bull Hosp Jt Dis (2013), 2017. **75**(4): p. 268-273.
6. Kamath, A.F., et al., *Quantifying the Burden of Revision Total Joint Arthroplasty for Periprosthetic Infection*. J Arthroplasty, 2015. **30**(9): p. 1492-7.
7. Kurtz, S.M., et al., *Economic burden of periprosthetic joint infection in the United States*. J Arthroplasty, 2012. **27**(8 Suppl): p. 61-5 e1.
8. Bhandari, M., et al., *Clinical and economic burden of revision knee arthroplasty*. Clin Med Insights Arthritis Musculoskelet Disord, 2012. **5**: p. 89-94.
9. Boddapati, V., et al., *Revision Total Knee Arthroplasty for Periprosthetic Joint Infection Is Associated With Increased Postoperative Morbidity and Mortality Relative to Noninfectious Revisions*. J Arthroplasty, 2018. **33**(2): p. 521-526.
10. *Hip and Knee Replacements in Canada, 2017 - 2018*. Canadian Joint Replacement Registry Annual Report, 2019. **Canadian Institute for Health Information**.
11. Morgenstern, M., et al., *Diagnostic challenges and future perspectives in fracture-related infection*. Injury, 2018. **49**: p. S83-S90.
12. Shohat, N. and J. Parvizi, *Prevention of Periprosthetic Joint Infection: Examining the Recent Guidelines*. J Arthroplasty, 2017. **32**(7): p. 2040-2046.
13. *AJRR Annual Report on Hip and Knee Arthroplasty Data*. American Joint Replacement Registry, 2019: p. 60.

14. Shahi, A., et al., *In-Hospital Mortality in Patients With Periprosthetic Joint Infection*. J Arthroplasty, 2017. **32**(3): p. 948-952 e1.
15. Saeed, K., et al., *2018 international consensus meeting on musculoskeletal infection: Summary from the biofilm workgroup and consensus on biofilm related musculoskeletal infections*. J Orthop Res, 2019. **37**(5): p. 1007-1017.
16. Morgenstern, M., et al., *The effect of local antibiotic prophylaxis when treating open limb fractures: A systematic review and meta-analysis*. Bone Joint Res, 2018. **7**(7): p. 447-456.
17. Kapadia, B.H., et al., *Periprosthetic joint infection*. The Lancet, 2016. **387**(10016): p. 386-394.
18. McConoughey, S.J., et al., *Biofilms in periprosthetic orthopedic infections*. Future Microbiol, 2014. **9**(8): p. 987-1007.
19. Parvizi, J., et al., *The 2018 Definition of Periprosthetic Hip and Knee Infection: An Evidence-Based and Validated Criteria*. J Arthroplasty, 2018. **33**(5): p. 1309-1314 e2.
20. Cyteval, C. and A. Bourdon, *Imaging orthopedic implant infections*. Diagn Interv Imaging, 2012. **93**(6): p. 547-57.
21. Zmistowski, B., et al., *Diagnosis of periprosthetic joint infection*. J Arthroplasty, 2014. **29**(2 Suppl): p. 77-83.
22. Cyteval, C., et al., *Painful infection at the site of hip prosthesis: CT imaging*. Radiology, 2002. **224**(2): p. 477-83.
23. Love, C., et al., *Role of nuclear medicine in diagnosis of the infected joint replacement*. Radiographics, 2001. **21**(5): p. 1229-38.
24. Love, C. and C.J. Palestro, *Nuclear medicine imaging of bone infections*. Clin Radiol, 2016. **71**(7): p. 632-46.
25. Gristina, A.G., *Biomaterial-centered infection: microbial adhesion versus tissue integration*. Science, 1987. **237**(4822): p. 1588-95.
26. Pandey, R., A.R. Berendt, and N.A. Athanasou, *Histological and microbiological findings in non-infected and infected revision arthroplasty tissues. The OSIRIS Collaborative Study Group. Oxford Skeletal Infection Research and Intervention Service*. Arch Orthop Trauma Surg, 2000. **120**(10): p. 570-4.
27. Choong, P.F., et al., *Risk factors associated with acute hip prosthetic joint infections and outcome of treatment with a rifampinbased regimen*. Acta Orthop, 2007. **78**(6): p. 755-65.
28. Giulieri, S.G., et al., *Management of infection associated with total hip arthroplasty according to a treatment algorithm*. Infection, 2004. **32**(4): p. 222-8.

29. Smith, A.W., *Biofilms and antibiotic therapy: is there a role for combating bacterial resistance by the use of novel drug delivery systems?* Adv Drug Deliv Rev, 2005. **57**(10): p. 1539-50.
30. Sasaki, T., et al., *In vitro elution of vancomycin from calcium phosphate cement.* J Arthroplasty, 2005. **20**(8): p. 1055-9.
31. Patel, A., et al., *Methicillin-resistant Staphylococcus aureus in orthopaedic surgery.* J Bone Joint Surg Br, 2008. **90**(11): p. 1401-6.
32. Jefferson, K.K., D.A. Goldmann, and G.B. Pier, *Use of confocal microscopy to analyze the rate of vancomycin penetration through Staphylococcus aureus biofilms.* Antimicrob Agents Chemother, 2005. **49**(6): p. 2467-73.
33. Andrews, J.M., *Determination of minimum inhibitory concentrations.* J Antimicrob Chemother, 2001. **48 Suppl 1**: p. 5-16.
34. Schumacher, A., et al., *In vitro antimicrobial susceptibility testing methods: agar dilution to 3D tissue-engineered models.* Eur J Clin Microbiol Infect Dis, 2018. **37**(2): p. 187-208.
35. Cobo, J., et al., *Early prosthetic joint infection: outcomes with debridement and implant retention followed by antibiotic therapy.* Clin Microbiol Infect, 2011. **17**(11): p. 1632-7.
36. Kuiper, J.W., et al., *Treatment of acute periprosthetic infections with prosthesis retention: Review of current concepts.* World J Orthop, 2014. **5**(5): p. 667-76.
37. Buchholz, H.W. and H. Engelbrecht, *[Depot effects of various antibiotics mixed with Palacos resins].* Chirurg, 1970. **41**(11): p. 511-5.
38. Boelch, S.P., et al., *Loading with vancomycin does not decrease gentamicin elution in gentamicin premixed bone cement.* J Mater Sci Mater Med, 2017. **28**(7): p. 104.
39. Aiken, S.S., et al., *Local release of antibiotics for surgical site infection management using high-purity calcium sulfate: an in vitro elution study.* Surg Infect (Larchmt), 2015. **16**(1): p. 54-61.
40. Jung, J., et al., *Complications after spacer implantation in the treatment of hip joint infections.* Int J Med Sci, 2009. **6**(5): p. 265-73.
41. Lilikakis, A. and M.P. Sutcliffe, *The effect of vancomycin addition to the compression strength of antibiotic-loaded bone cements.* Int Orthop, 2009. **33**(3): p. 815-9.
42. Hanssen, A.D., *Prophylactic use of antibiotic bone cement: an emerging standard--in opposition.* J Arthroplasty, 2004. **19**(4 Suppl 1): p. 73-7.

43. Hanssen, A.D. and M.J. Spanghehl, *Practical applications of antibiotic-loaded bone cement for treatment of infected joint replacements*. Clin Orthop Relat Res, 2004(427): p. 79-85.
44. Urabe, K., et al., *In vitro comparison of elution characteristics of vancomycin from calcium phosphate cement and polymethylmethacrylate*. J Orthop Sci, 2009. **14**(6): p. 784-93.
45. Samuel, S., et al., *In vitro study of elution kinetics and bio-activity of meropenem-loaded acrylic bone cement*. J Orthop Traumatol, 2012. **13**(3): p. 131-6.
46. Tsiapla, A.R., et al., *Drug delivery nanoplatfrom for orthopaedic-associated infections*. Materials Today: Proceedings, 2017. **4**(7): p. 6880-6888.
47. Dusane, D.H., et al., *Effects of loading concentration, blood and synovial fluid on antibiotic release and anti-biofilm activity of bone cement beads*. J Control Release, 2017. **248**: p. 24-32.
48. Bishop, A.R., et al., *Vancomycin elution, activity and impact on mechanical properties when added to orthopedic bone cement*. J Mech Behav Biomed Mater, 2018. **87**: p. 80-86.
49. Larsson, S., *Injectable Phosphate Cements - A Review*. Uppsala, Sweden, 2006. **2006**.
50. Oliver, R.A., et al., *Application of Calcium Sulfate for Dead Space Management in Soft Tissue: Characterisation of a Novel In Vivo Response*. Biomed Res Int, 2018. **2018**: p. 8065141.
51. Kim, T.W.B., et al., *3D printed liner for treatment of periprosthetic joint infections*. Med Hypotheses, 2017. **102**: p. 65-68.
52. Anagnostakos, K. and C. Meyer, *Antibiotic Elution from Hip and Knee Acrylic Bone Cement Spacers: A Systematic Review*. Biomed Res Int, 2017. **2017**: p. 4657874.
53. Cao, Z., et al., *In vitro and in vivo drug release and antibacterial properties of the novel vancomycin-loaded bone-like hydroxyapatite/poly amino acid scaffold*. Int J Nanomedicine, 2017. **12**: p. 1841-1851.
54. Bakhshandeh, S., et al., *Simultaneous Delivery of Multiple Antibacterial Agents from Additively Manufactured Porous Biomaterials to Fully Eradicate Planktonic and Adherent Staphylococcus aureus*. ACS Appl Mater Interfaces, 2017. **9**(31): p. 25691-25699.
55. Hernandez-Soria, A., et al., *In vitro elution characteristics of antibiotic laden BoneSource, hydroxyapatite bone cement*. J Biomater Sci Polym Ed, 2013. **24**(7): p. 797-806.
56. Suhardi, V.J., et al., *A Fully Functional Drug-Eluting Joint Implant*. Nat Biomed Eng, 2017. **1**.

57. Houdek, M.T., et al., *Elution of High Dose Amphotericin B Deoxycholate From Polymethylmethacrylate*. J Arthroplasty, 2015. **30**(12): p. 2308-10.
58. Stevens, C.M., et al., *An articulated antibiotic spacer used for infected total knee arthroplasty: a comparative in vitro elution study of Simplex and Palacos bone cements*. J Orthop Res, 2005. **23**(1): p. 27-33.
59. Merkhan, I.K., J.M. Hasenwinkel, and J.L. Gilbert, *Gentamicin release from two-solution and powder-liquid poly(methyl methacrylate)-based bone cements by using novel pH method*. J Biomed Mater Res A, 2004. **69**(3): p. 577-83.
60. McConoughey, S.J., et al., *Comparing PMMA and calcium sulfate as carriers for the local delivery of antibiotics to infected surgical sites*. J Biomed Mater Res B Appl Biomater, 2015. **103**(4): p. 870-7.
61. Rogers, B.A., et al., *Does cyclical loading affect the elution of antibiotics from articulating cement knee spacers?* J Bone Joint Surg Br, 2011. **93**(7): p. 914-20.
62. Kummer, A., U.F. Tabin, and O. Borens, *Effect of Sonication on the Elution of Antibiotics from Polymethyl Methacrylate (PMMA)*. J Bone Jt Infect, 2017. **2**(4): p. 208-212.
63. Kelm, J., et al., *In vivo and in vitro studies of antibiotic release from and bacterial growth inhibition by antibiotic-impregnated polymethylmethacrylate hip spacers*. Antimicrob Agents Chemother, 2006. **50**(1): p. 332-5.
64. Seidlitz, A., et al., *In vitro determination of drug transfer from drug-coated balloons*. PLoS One, 2013. **8**(12): p. e83992.
65. van Oosten, M., et al., *Real-time in vivo imaging of invasive- and biomaterial-associated bacterial infections using fluorescently labelled vancomycin*. Nat Commun, 2013. **4**: p. 2584.
66. Stone, M.R.L., et al., *Fluorescent Antibiotics: New Research Tools to Fight Antibiotic Resistance*. Trends Biotechnol, 2018. **36**(5): p. 523-536.
67. Liu, S.J., et al., *In vivo release of vancomycin from biodegradable beads*. J Biomed Mater Res, 2002. **63**(6): p. 807-13.
68. Kelly, C.N., et al., *Fatigue behavior of As-built selective laser melted titanium scaffolds with sheet-based gyroid microarchitecture for bone tissue engineering*. Acta Biomater, 2019. **94**: p. 610-626.

Chapter 2

2 Quantitative, non-invasive micro-CT imaging technique to characterize small-molecule diffusion

We have developed a quantitative, non-invasive, longitudinal, micro-CT imaging technique to characterize the diffusion of a small-molecule drug surrogate within an intact, agar tissue-equivalent phantom. Iohexol, an iodine-based x-ray contrast agent, was selected as a drug surrogate to estimate the relative diffusion behavior of a commonly used antibiotic (*i.e.*, Vancomycin) within three different carriers. A concentration of Iohexol was selected that maintains appropriate image contrast during the series of longitudinal scans to effectively monitor diffusion, and with sufficiently low beam-hardening effects that could be corrected within each experiment.

The short-term and long-term release of the drug surrogate was observed in a two-part phantom consisting of a cylindrical, finite-source “core” containing the drug surrogate, and a surrounding agar, tissue-equivalent “sink” into which the drug surrogate diffuses. The phantom core was created by mixing the Iohexol contrast agent drug surrogate into a carrier material – either one of two calcium sulphate-based (CaSO_4) matrices or pure agar – for different experiments. Diffusion of the drug surrogate into the surrounding tissue-mimic was observed by monitoring the image signal intensity as the contrast-agent progresses outward from the cylindrical, finite-source core during longitudinal scanning. It was assumed that the contrast agent is more or less homogeneously distributed throughout the carrier, forming a monolithic solution. In this chapter, the experimental design of the diffusion phantom is explained in detail, along with micro-CT image acquisition parameters selected for the purpose of this work. Images were corrected for beam-hardening “cupping” artifact that would affect the apparent relative diffusion of the contrast agent. Image analysis was performed to assess contrast-agent (*i.e.*, drug surrogate) concentration and track radial-diffusion distance for the duration of the longitudinal scanning. The diffusion coefficient of the drug-surrogate contrast agent through our carrier materials was then calculated, based on available mathematical models of diffusion [1-3].

2.1 Introduction

Peri-prosthetic joint infection (PJI) has been receiving a high level of attention in recent years [4]; as described in Chapter 1, it is a serious complication resulting in prolonged treatment and morbidity [5]. To eliminate the infection in a clinical environment, systemic treatment is performed along with local antibiotic delivery. Current delivery methods are by incorporating commonly used antibiotics (*e.g.*, Vancomycin, Tobramycin, Gentamycin) in a matrix carrier to form a drug delivery system. Carriers are then implanted into the joint space temporarily to elute antibiotics. *In-vitro* studies demonstrate that calcium sulfate-based carriers (*e.g.*, Stimulan[®] Rapid Cure) may improve the elution of antibiotics (*i.e.*, Vancomycin) compared to commonly used Poly (methyl methacrylate) (PMMA) carriers [6].

Although local antibiotic delivery is widely used in PJI management, the exact diffusion mechanism remains elusive to the extent of our knowledge. Thus, a new approach is required to better understand and enhance antibiotic elution through finite-source, local drug-delivery carriers. There are complications associated with *in-vivo* tracking of drug diffusion and release amount due to biological factors and chemical reactions. Different types of mass transport processes can be involved *in vivo* in the control of drug release from a carrier. This might include the penetration of water into the system (osmotic effects), drug diffusion from the carrier, drug dissolution, carrier swelling, carrier erosion, and various other phenomena [1]; however, “ *if several of these processes occur in a sequence and one is much slower than all the other, the slowest one is the rate-limiting step for the entire sequence*” [1]. In many cases, drug diffusion is the predominant step, however, in some others, it plays a major role in combination with carrier swelling or degradation [1]; in this study, we focused on mass diffusion controlled drug-delivery systems. For the system to be diffusion controlled, the rate of dissolution of drug particles within the matrix carrier is assumed to be much faster than the diffusion rate of the dissolved drug leaving the carrier [7]. Some carriers have a very high rate of resorption *in vivo* (*i.e.*, calcium sulphate carriers that resorb within 40-70 days after implantation), which affects the effective elution of small-molecules. In this work, we evaluate the diffusion of an Iohexol-based contrast agent as a drug-surrogate only through mass diffusion.

Drug diffusion (*e.g.*, antibiotics) from a carrier (*i.e.*, PMMA and mineral based bone substitutes) has been studied *in vitro* in PJI management by application of chemical analysis such as chromatography and spectroscopy [8-11]. While such studies have yielded valuable information, they provide little understanding of drug diffusion distance from a finite source into a finite environment that is similar to *in-vivo* conditions. These methods also limit real-time, non-invasive tracking of diffusion, which could provide quantitative information in future studies of drug diffusion in live animals.

Imaging can be a non-invasive longitudinal technique to track the diffusion of small molecules over time from a finite source to a finite environment in an intact phantom. The concept of tracking a surrogate molecule has been reported previously. Fluorescein (molecular weight 332 Da) was used as an optical tracer to study elution in calcium-sulfate based carriers and Poly (methyl methacrylate) (PMMA) [12]. Our approach instead uses an X-ray contrast agent (iodine-based Iohexol), with a molecular weight of 821 Dalton (Da), which is much closer to that of commonly used antibiotics, like Vancomycin (molecular weight 1449 Da), to track diffusion in a tissue-equivalent agar sink.

The purpose of this chapter is to characterize the diffusion of a small molecule drug surrogate from calcium-sulphate and agar-based carriers into an agar tissue-equivalent sink. This objective has been accomplished by developing a novel method for image-based quantification of small-molecule diffusion; we use a micro-CT imaging technique to collect the attenuation of a high-atomic number contrast agent drug surrogate (iodine-based Iohexol) over regular time intervals. Corresponding CT numbers are correlated to the concentration of contrast agent drug surrogate within the voxels; this will allow us to track the diffusion distance and the cumulative amount released from the finite-source over time. The diffusion coefficient was then calculated by using the acquired data set from volumetric images and implementing previously described mathematical diffusion models.

2.1.1 Micro-CT Imaging

Within this work, our interest is placed on the use of a micro-CT imaging technique to monitor and quantify the diffusion of a contrast agent drug surrogate into an agar sink, using a tissue-equivalent phantom. Here, the micro-CT imaging approach will be described, along

with the specification of the system selected to monitor the diffusion and subsequent relative features for our experiments.

Wilhelm Conrad Röntgen first announced the discovery of X-rays in 1895 [13]. Planar x-ray imaging is the earliest medical imaging modality that was clinically used before the development of the CT imaging technique. X-ray imaging techniques are based on creating an image by irradiating the specimen of interest. In planar X-ray imaging, the image that is created is a single X-ray projection of the specimen. The X-ray source transmits a beam of photons to irradiate the specimen. The intensity of the X-ray beam is attenuated through the specimen along paths of known geometry. Attenuation is a result of X-ray photon interactions with the atoms and orbital electrons within the specimen, which can be either via absorption or scattering; the attenuation coefficient describes the amount of attenuation. A detector is then placed opposite the X-ray source to collect and measure the intensity of attenuated X-ray beams to create an image [14].

Computed tomography (CT) imaging is also an X-ray-based imaging technique. It combines X-ray transmission with computed tomographic reconstruction to make three-dimensional (3D) image volumes. The image that is created consists of a 3D array of volume elements (*i.e.*, voxels, or 3D pixels) that represent the radio density, or mean linear X-ray attenuation of the material contained within each individual voxel. Unlike planar x-ray images that represent the total attenuation of the X-rays along a line passing through the complete specimen, images in clinical computed tomography (CT) are created with a fan-shaped x-ray beam that rotates around the object while it moves through the gantry. The x-ray source and detector are mounted onto a rotating gantry, which allows the acquisition of x-ray projections over 360° around the object.

CT numbers are used to quantify the differences in X-ray attenuation occurring in a voxel. Attenuation values are typically scaled to Hounsfield units (HU) [15]. Values are based on the tissue electron densities and level of photon absorption. Air and water are arbitrarily assigned the values of -1000 HU and 0 HU, respectively, and are commonly used for calibration purposes [16]. In clinical applications, the best-visualized tissues with the most significant contrast in X-ray images are highly attenuating tissues (such as bone) and least attenuating tissue (such as an air-filled lung). The differences in X-ray attenuation are

determined by the object's electron density and physical density in each projection image. Attenuation, therefore, leads to image contrast in X-ray imaging. Hounsfield and Cormack were awarded the Nobel Prize in medicine (1979) for the invention of CT imaging [15, 17].

Cone-beam CT is based on the same principles as a conventional CT scanner but with the advantages of faster acquisition and (typically) higher resolution [18]. There is a cone-shaped X-ray beam (*i.e.*, fan in two directions) with a rotating flat-panel area detector (Fig 2.1). Transmission data is collected by an area detector, rather than multiple rows of detectors, allowing a fast scan of the entire organ in the body in clinical application. The rotating-gantry configuration is the most common configuration for cone-beam CT scanners; this design mounts the tube and detector on a gantry that rotates around a central axis [18]. The rotating object is another less common design of cone-beam CT scanners. Cone-beam back-projection reconstruction algorithms that account for geometry and ray path than are used to reconstruct a volumetric image from two-dimensional (2D) image projections. The duration of the collection of projections depends on the flux of photons being produced by the X-ray source, the efficiency of the X-ray detector, and the amount of attenuation of the photons by the scanned material. It is possible to make trade-offs in the system to collect scans faster or slower, with associated impacts on the image quality.

Micro-computed tomography (micro-CT) functions in the same manner as clinical CT scanners, but provides higher reconstruction resolution. Moreover, micro-CT scanners create images with isotropic voxels, and there is a consistent resolution in all planes. Typical scanners are available with voxel sizes ranging from 5 to 450 μm and fields of view ranging from 1 to 20 cm [19]. Micro-CT has developed into a popular research tool in small-animal and phantom experiments since it provides finer isotropic resolution [20]. Micro-CT has also been shown to have the capability of providing advanced analytical techniques and detailed internal quantitative information to investigate drug delivery [21, 22].

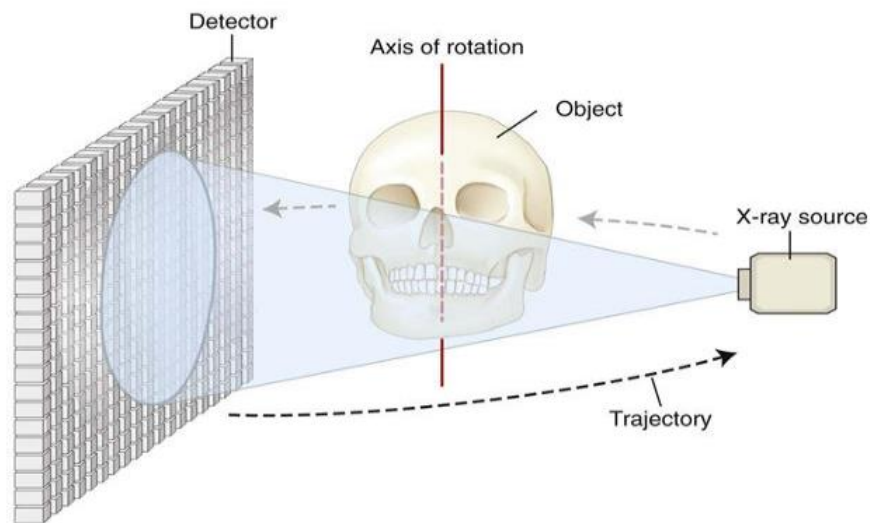


Figure 2.1: Principle of cone-beam CT scanner. Object is irradiated by the X-ray beam and the attenuated X-rays are collected by a flat panel detector, providing a single two-dimensional projection. The gantry rotates by a small defined increment angle; at the next angular position another projection is acquired. Subsequently numerous 2D projections are collected over various angles around the object to construct a volumetric image.

(adapted from cone beam computed tomography by William C. Scarfe and Allan G. Farman, chapter 11)

Laboratory micro-CT scanners (*e.g.*, the GE eXplore speCZT located at the Robarts Research Institute, Fig 2.2) consist of a cone-beam X-ray source and 2D flat panel detector, which provides a collection of multiple paths of attenuation simultaneously. This pre-clinical micro-CT system has a high resolution (*i.e.*, 50 μm) combined with fast scanning speed. An area detector mounted on a gantry allows the X-ray source and detector to rotate around the phantom and collect individual 2D projections at different angles in a relatively short time (typically 5 minutes per volume). After collection of a series of 2D images, it is necessary to reconstruct the 3D volume. The 2D projection are convolved with proper Kernel function to reduce blur and then back-projected into the 3D space to create the final image. The reconstructed images are comprised of a 3D matrix of voxels, with each voxel containing a CT number, which is proportional to the mean linear attenuation coefficient of the material

within that voxel. The intensity of each voxel is then measured and rescaled in Hounsfield units.

In this work, we investigate the application of a micro-CT imaging technique to characterize the diffusion of a contrast-agent drug surrogate. An image-based technique to characterize diffusion has the advantage of tracking diffusion mechanisms non-invasively and without sample collection, also providing real-time characterization of diffusion. In this work, a radio opaque contrast agent with high atomic number and density was chosen to be used as a surrogate for commonly used antibiotics (*i.e.*, Vancomycin) to evaluate diffusion in an agar tissue-equivalent phantom. Cumulative release amount was measured by taking advantage of the relationship between CT number and contrast-agent concentration in acquired volumetric images [23, 24] and the law of mass conservation. The technique described in this chapter allows non-invasive, non-destructive analysis of contrast-agent drug-surrogate diffusion over an extended time in an intact phantom. This approach will simulate mass-diffusion controlled delivery systems and is used to compare the diffusion behaviour of one drug-surrogate (*i.e.*, iodine-based Iohexol) out of different carrier matrices into an agar sink.



Figure 2.2: GE eXplore speCZT. Located at Robarts Research Institute, it is a cone-beam micro-CT imaging system, which we used in this work to characterize diffusion of a contrast-agent drug surrogate (Iohexol).

2.1.2 Beam Hardening

CT scanners use polychromatic x-ray beams which can be characterized by the peak energy. For example, in this study, we scanned our phantom at a tube voltage of 90 kVp; it means that our photons have energy ranging from 20 – 90 keV. In imaging different materials, low-energy photons mainly absorb by photoelectric absorption (Grodstein, 1957); the mean energy of remaining photons increases, and this results in the transmitted spectrum becoming "harder." Beam hardening causes an artifact in CT reconstructed volumetric images. In other words, there would be an overestimate in photon transmission, which leads to underestimating the attenuation coefficient of materials [25]. The center of an object will exhibit lower CT numbers than the edges in a homogeneous material, which is described as a "cupping" artifact (Fig 2.3). The higher the density of the material, the more discrepancy between the reconstructed and true attenuation coefficients.

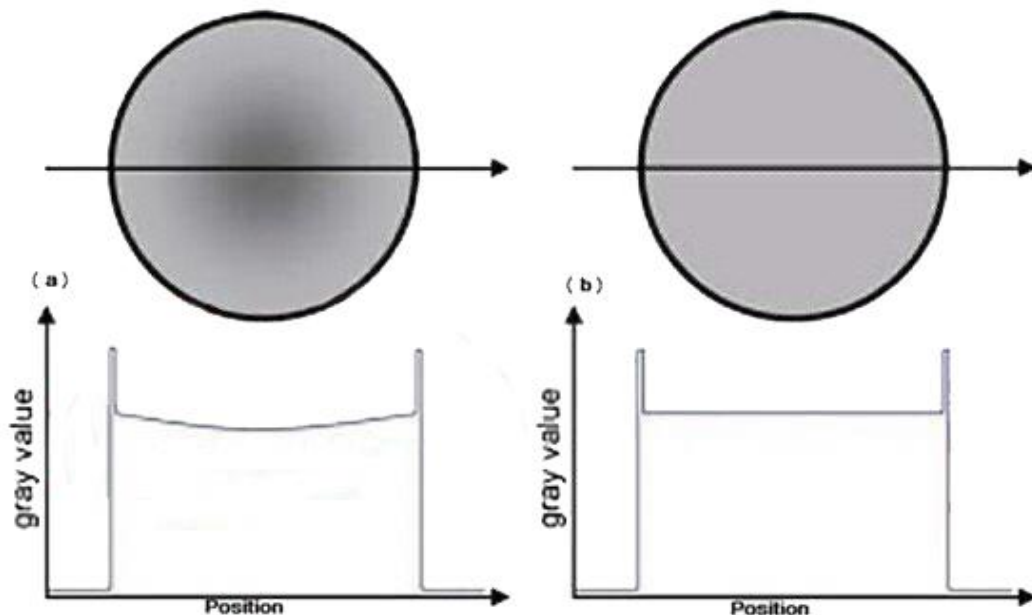


Figure 2.3: Cupping artifact. Beam hardening results in a cupping artifact at the center of the circle (a) not corrected, (b) corrected. The x-ray beam becomes harder through center and the center is erroneously assigned a lower gray value (CT number).

(adapted from www.radiologycafe.com/radiology-trainees/frcr-physics-notes/ct-artifacts)

In this work, volumetric images were corrected for beam hardening artefact. Iohexol has a relatively high CT number compared to the agar tissue-equivalent phantom; thus, the reconstruction process will have the effect of "cupping" artifact due to beam hardening. This cupping artifact will result in inaccuracies in the measurement of the concentration that remains in the carrier at each time point. In order to obtain accurate values of drug surrogate contrast-agent concentration and diffusion distance, we must use an algorithm to correct our data for beam hardening. In this project, we verified and used an algorithm that was previously developed in-house [26].

2.2 Materials and Methods

2.2.1 Contrast Agent

A commercially available contrast agent; iodine-based Iohexol (Omnipaque™ 300, GE Healthcare Canada Inc) was used in this study as a drug surrogate. Omnipaque 300 contains 300 mg of iodine per milliliter. It has an osmolality of 465 mOsm/L, absolute viscosity of 6.3 Pa.s, and specific gravity of 1.349 at 37°C. Iohexol is a common radiographic agent with a molecular weight of 821 Dalton. The Wilke- Cheng equation proposes that there is a strong correlation between the diffusion coefficient and molecular weight [27]; therefore, in this work, we hypothesized that by understanding the relative diffusion characteristics of Iohexol, we can infer the diffusion of commonly used antibiotics like Vancomycin into tissue in local PJI treatment. A contrast-agent concentration was chosen so that we maintained sufficient contrast in 3D reconstructed images throughout the duration of longitudinal micro-CT scanning to track diffusion, but which did not cause unmanageable beam-hardening artifacts.

2.2.2 Experimental Design

Diluted iodinated contrast agent (containing 30 mg/mL of Iodine) was used as a surrogate to mimic diffusion of drug in a two-part cylindrical agar sink, tissue-equivalent intact phantom. Inner cylinder cores for each experiment were placed at the center of the outer cylinder. Inner cores were surrounded by pure agar which formed outer annulus (Fig 2.4). We would expect Iohexol molecules to move in a random way and diffuse from the area of the higher concentration (cylindrical finite-source cores) to lower concentration (agar in outer annulus). Three different cylindrical inner cores were fabricated: inner cylinders were made by adding

the diluted contrast agent to agar and 2 different calcium sulfate matrices (*i.e.*, Stimulan[®] and Plaster-of-Paris). Agar and calcium sulphate matrices were evaluated as carriers for the drug surrogate contrast agent, forming a model delivery system. Control phantoms were also fabricated with the same dimensions but with no contrast agent added to the carrier matrices at each experiment. Micro-CT imaging was used to measure the signal intensity at regular time intervals. Beam hardening correction was performed on projections to correct associated artifacts (*e.g.*, cupping) prior to reconstruction of 3D volumes for each time point. 3D volumetric data sets were generated from the corrected projections using a Feldkamp, filtered, back-projection algorithm (eXplore speCZT, General Electric Healthcare, London, Ontario) implemented in the scanner software [28]. In order to reduce noise and increase the in-plane signal-to-noise ratio, the data were spatially-averaged along the z-axis. This axial spatial-averaging along Z-axis was performed to improve the estimation of the radial diffusion.

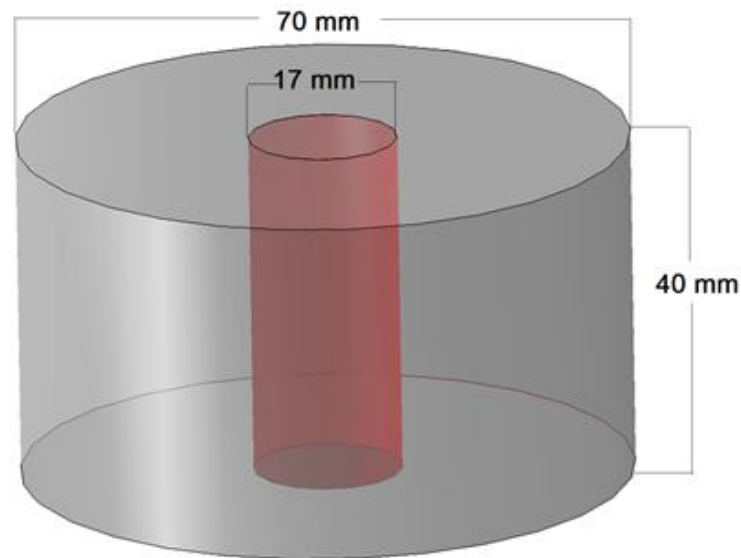


Figure 2.4: Two-part intact phantom – A schematic diagram of the diffusion phantom, showing the finite-source (30 mg/ml Iohexol) “core” carrier material (agar or CaSO₄ matrices) in red and the tissue-equivalent “sink”(agar) in gray into which the drug-surrogate contrast agent diffuses during the longitudinal micro-CT imaging experiments.

2.2.3 Phantom Molds

To ensure consistency of a series of phantoms and facilitate repeated experiments, we fabricated two custom molds. The first was an elastomer mold used for pouring an inner core (17 mm diameter \times 40 mm length) containing the drug-surrogate mixture in a carrier matrix. A two-part, “negative” housing-mold (Fig. 2.5) was created in CAD software (Solidwork, Dassault Systemes). The CAD files were then imported to a 3D-printer (DREMEL 3D40, Dremel Digilab, Illinois, USA) and fabricated from Dremel polylactic acid (PLA) filaments to create a two-part, silicone elastomer mold (Fig 2.5). The two-halves of the elastomer mold were assembled, and the core matrix mixture was poured into the mold to create the inner core of the phantom (Fig 2.5).

A second, 3D-printed, container-mold allowed for the pouring of an outer, thick-walled, cylindrical annulus of pure agar, which acts as a tissue-equivalent sink for the drug-surrogate. A 15-hour print time with 50 μ m layer thickness was chosen to achieve a smooth finish and minimum deviation from the CAD design (Fig 2.5). This radiolucent, PLA, container-mold housed the phantom, and a 3-to-4 mm gap just underneath the lid, filled with de-ionized water, helped to avoid interaction between the agar and air. Lateral ridges oriented the phantom rotationally on the shoulders of the micro-CT bed for fast and accurate re-positioning during longitudinal scanning. This mold had an outer diameter (OD) of 70 mm, a height (H) of 53 mm, and wall thickness (WT) of 1.5 mm (Fig 2.5). Dimensions of the container were chosen such that it was circumscribed entirely within a single-acquisition field-of-view (FOV) of the micro-CT scanner (eXplore speCZT, General Electric Healthcare, London, Ontario). The housing-container lid was designed with air- and water-filled calibration chambers (Fig 2.6) to rescale gray-scale values to CT numbers in Hounsfield units (HU). This mold was then reproduced to test different within different materials.

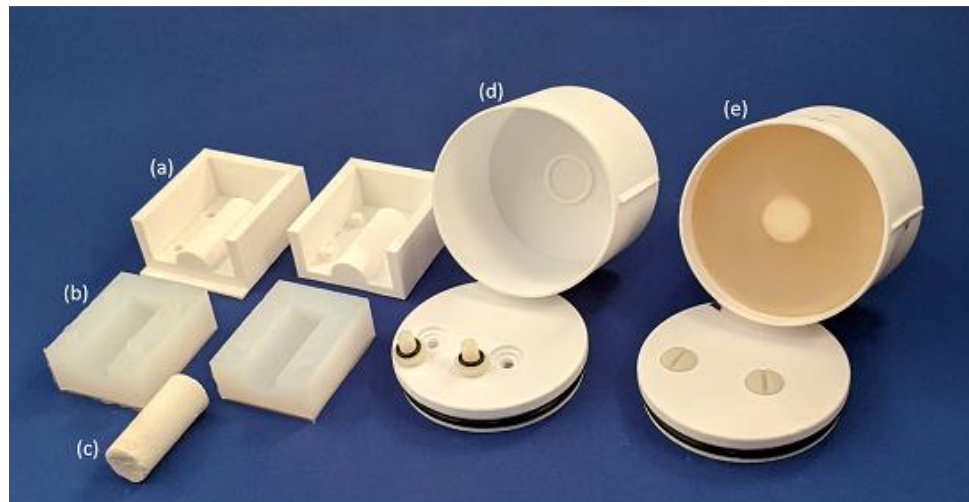


Figure 2.5: Molds and final assembled diffusion-phantom (a) a two-part, 3D-printed, “negative” mold used for making the silicone-elastomer, inner-core mold; (b) two-part, silicone-elastomer mold used for casting the inner-core ; (c) Iohexol-loaded, inner-core carrier of Stimulan matrix containing the drug-surrogate; (d) 3D-printed, PLA container mold for housing the phantom showing the lid with air- and water-calibration chambers, sealing-screws, and o-rings; (e) final, assembled, diffusion phantom showing the inner-core carrier surrounded by the agar tissue-equivalent sink into which the contrast-agent drug-surrogate diffuses.

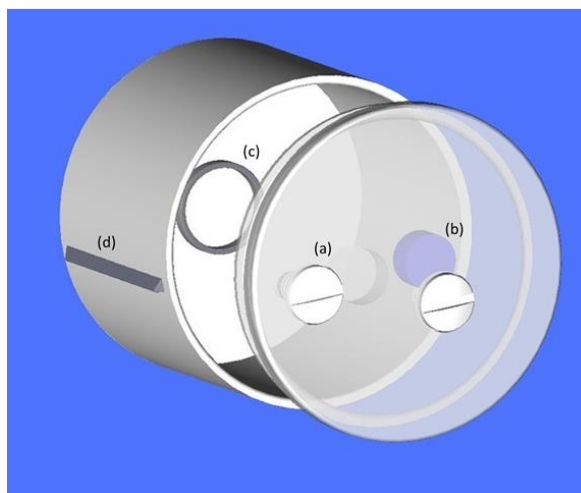


Figure 2.6: Phantom container-mold – CAD drawing of the 3D-printed, PLA, container-mold showing the (a) air and (b) water linear-calibration chambers in the phantom lid; (c) the central alignment ring in the base for accurate placement of the carrier core; and (d) the lateral ridges for rotational orientation.

2.2.4 Phantom Preparation

Inner cylindrical cores were prepared from agar (A9799, Sigma-Aldrich, Oakville, Ontario, CA), high-purity calcium sulphate (Stimulan[®] Rapid Cure, Biocomposites, Keele, U.K.) and Plaster-of-Paris (DAP, Scarborough, Ontario, Canada) powders.

To evaluate Iohexol diffusion from an agar-cylinder carrier core into an agar annulus (*i.e.*, single-phase diffusion), we prepared a sufficient agar volume solution for fabricating both the inner core and outer annulus. The outer annulus and inner core have volumes of 145 cm³ and 9 cm³, respectively. A standard formulation was used to prepare the agar [29]. 300 ml of de-ionized water was mixed at room temperature with 10.5 g agar powder. The mixture was manually stirred until homogeneous and heated at a temperature of 90-95°C for five minutes, after which impurities were skimmed from the surface. Heating and skimming were repeated two more times, for two additional minutes each time. The agar mixture was observed during heating to achieve homogeneous appearance and to avoid boiling. A warm water bath of approximately 85-90°C was used to maintain agar in the liquid phase during phantom fabrication. Trapped air bubbles were then removed manually from the end product. A vacuum chamber can also be used to remove small air bubbles in the liquid. To fabricate the Iohexol-loaded agar inner core, 0.91 ml of Iohexol (Omnipaque 300, GE Healthcare, Oakville, ON) was added to 8.17 ml of agar and mixed to obtain a homogeneous compound. This mixture was poured into a custom, non-expandable, inert, elastomeric silicone mold (Fig 2.5b) and was left undisturbed for one hour to let the agar mixture set. The two-part silicone mold was separated, and the Iohexol-loaded agar core was removed. Then, the core was centered within the custom, 3D-printed, PLA container-mold (Fig 2.5d). Pure agar was then added to the core-periphery to form an annulus. The final assembled phantom was kept undisturbed for approximately 60 minutes (Fig 2.5e). The container-mold lid was designed with integral air- and water-filled calibration chambers (Fig 2.5d) for the CT calibration purposes.

Iohexol-loaded Stimulan[®] and Iohexol-loaded plaster cores were both fabricated using the same custom, non-expandable, inert, silicone elastomer mold. The contrast agent was prepared by diluting 1.0 ml of full-strength, non-ionic Iohexol with 9.0 ml of de-ionized water. 18.54 g of Stimulan[®] powder was weighed and then mixed with 10 ml of diluted

Iohexol (30 mg/ml) as per the manufacturer's instructions and hand-mixed for 45 to 60 s to form a homogeneous paste. The same formulation was used to make the Iohexol-loaded plaster core. Specimens were kept at room temperature for 60 minutes to allow them to cure. Control phantoms with no Iohexol were made out of pure Stimulan[®] and pure plaster within the inner cores. Once again, cores were cast into pure agar and kept undisturbed at room temperature for approximately one hour to allow the agar to set prior to micro-CT scanning. De-ionized water was added on top of the agar to prevent evaporation. The water chamber embedded in the container-mold lid was filled with de-ionized water for CT calibration purposes. Final assembled phantoms were maintained at room temperature through the entire duration of micro-CT scans.

2.2.5 Image Acquisition

Diluted Iohexol, a non-ionic iodinated contrast agent Omnipaque[™], was used as a drug surrogate and our tracer source. Control phantoms containing agar, Stimulan[®] and plaster were scanned individually to achieve a baseline and corresponding CT number in Hounsfield units (HU). Image acquisition started as early as 75 minutes after phantom fabrication. Scanning was performed using a micro-CT scanner (eXplore speCZT, General Electric Healthcare, London, Ontario). All samples were scanned with an X-ray tube peak-voltage of 90 kVp, tube current of 40 mA with a large focal spot. 900 projections, each 16 ms in duration per frame, were acquired at 0.4° increments over a 360° rotation of the gantry. The relatively short scan duration of 5 minutes was selected to minimize the amount of diffusion occurring during each scan. The set of 900 projections was reconstructed into a three-dimensional (3D) data set at a nominal, isotropic voxel spacing of 50 μm. Each 3D data set was further spatially-averaged over $2 \times 2 \times 2$ voxels, resulting in a final $875 \times 875 \times 572$ voxel matrix with 100μm isotropic spacing. Since we aimed to track the diffusion of small molecule drug surrogate, we needed to minimize the movement of our sample during scanning. This micro-CT scanner utilizes rotating source-detector geometry allowing the sample to remain stationary during the scanning process. The manufacturer-supplied reconstruction algorithm was used for 3D images after performing custom beam-hardening correction on all projections.

Scanning was performed at 1.25, 3.58, 5.08, 8.08, 18.08, 30.08, 47.58, and 76.08 hours after fabrication for the Iohexol-loaded agar core surrounded by agar. Image acquisition in Iohexol-loaded Stimulan[®] and Plaster-of-Paris cores within an agar annulus continued up to 25 days to ensure sufficient time intervals for the diffusion of Iohexol through the calcium sulphate carrier into agar at the periphery. Scanning was similarly performed at 1.25, 4.25, 8.25, 11.25, 23.5 hours after fabrication, then every 24 hours for the next seven days and finally every 2 days for a further 17 days. Time zero was defined as the time of casting the inner core within the outer pure agar annulus in the custom 3D printed PLA container.

2.2.6 Beam Hardening Correction

Diametric line profiles along axial CT slices exhibited considerable cupping artifacts within images, due to beam hardening. Cupping artifacts result in errors in signal intensity measurements at each time point that could lead to misrepresenting of contrast agent drug-surrogate concentration across the inner core and outer annulus, thus requiring a correction algorithm. A beam hardening correction (BHC) algorithm was performed at each time point on the acquired projections on the scanner prior to reconstruction. Diametric line profiles were plotted at the exact same position to eliminate any error due to the repositioning of profiles. Plots were compared to evaluate the efficiency of the beam hardening correction (Fig 2.7). The correction algorithm will be described in detail.

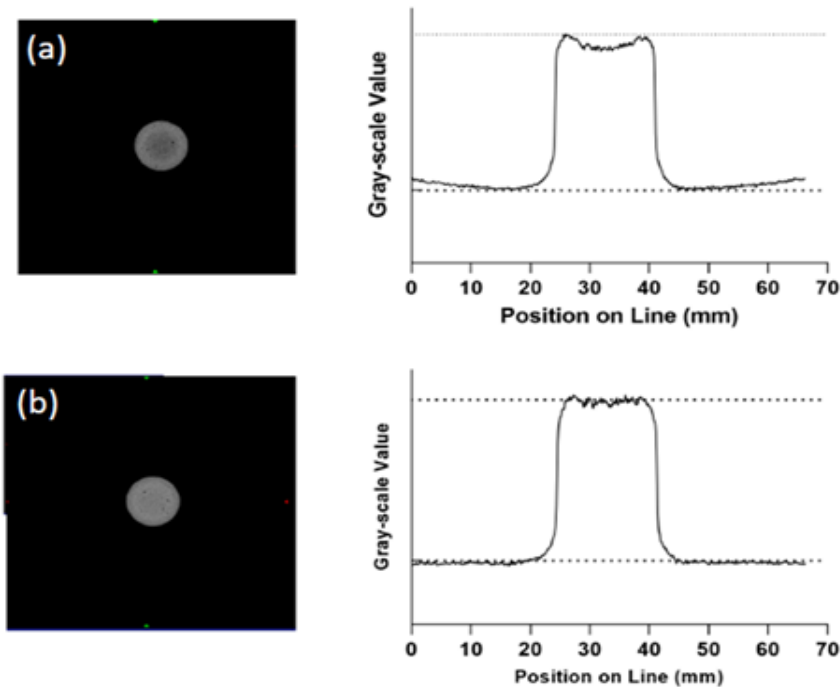


Figure 2.7: Beam hardening correction. Iohexol-loaded Stimulan[®] core in agar scanned on SpeCZT (90 kVp, 40 mA), 1.25 hrs after fabrication, with CT axial slice and corresponding diametric line profiles in the same axial CT slice. (a) no beam hardening correction (b) with beam hardening correction. Cupping artifact caused underestimation of attenuation within the inner core Iohexol-loaded matrix. CT numbers represent relative Iohexol concentration.

Beam hardening correction was performed using an algorithm that was developed in-house [26]. In this method, aluminum (Al) was used as a single calibration material to reduce or remove signal intensity errors significantly (*i.e.*, cupping artifact). The Al calibration phantom was designed and manufactured in our laboratory. This Al phantom is a single object comprised of eight coaxial cylinders with diameters ranging from 4.5 mm to 60 mm; two opposite sides were flattened in a 20° arc to provide larger locations for measurement (Fig 2.8). Image acquisition of the Al phantom was performed in the micro-CT scanner by using an acquisition protocol (90 kVp, 40 mA) that is consistent with the protocol we used for our diffusion experiments. We collected the transmission ratio values versus different known thicknesses of Al phantom to verify the BHC algorithm for application in our

experiments. Acquired data were then analyzed by analysis software (MicroView 2.2, General Electric Healthcare, London, ON).

Custom regions of interest (ROIs) were selected at each individual known thickness of the Al phantom and the CT transmission ratio of selected ROIs was measured automatically (in arbitrary units) in MicroView. We collected Al data based on the range of the transmission ratio values that we obtained in our diffusion experiments (*i.e.*, maximum CT transmission ratio of inner cores observed at the first scan time in diffusion phantoms). CT transmission ratio versus different known Al thicknesses were plotted.

The plot represented non-linearity of thickness to transmission ratio (Fig 2.9). Data were fitted to a non-linear inverted one-phase (inverse) decay numerical function in Prism (GraphPad 8.1.2 Software, Inc., La Jolla, CA, USA) with high accuracy ($R^2 > 0.99$) and described by the equation ($Y = (Y_0 - P) \times \exp(-K * x) + P$) where Y_0 is the Y value when x is zero. P is the Y value at x at infinite, K is rate constant; x is the known thickness. This function was then implemented in custom software to create a look-up table to linearize the log CT transmission [26].

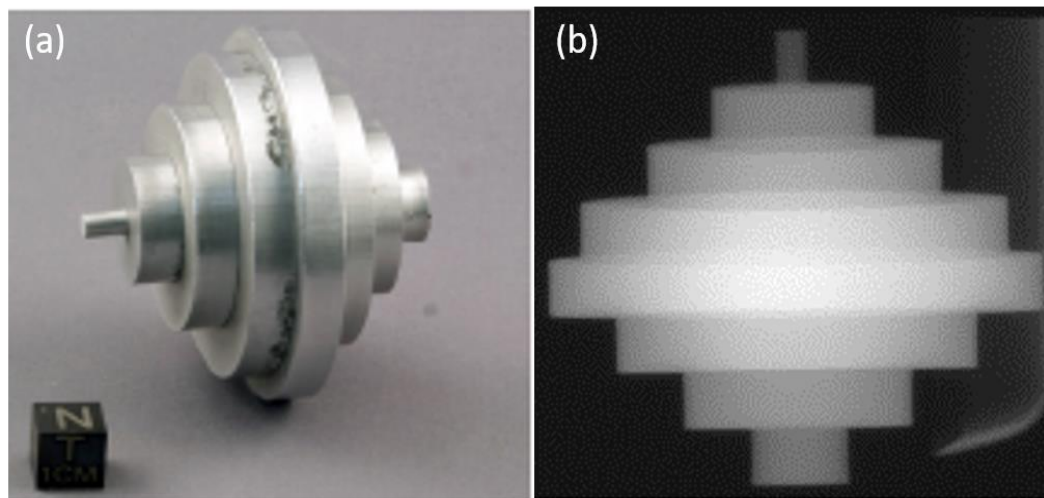


Figure 2.8: Al Calibration phantom for beam hardening correction in micro-CT and corresponding transmission image. (a) Al phantom was fabricated in house in different thickness by gluing disks of various diameters together in an alternating fashion. (b) Projection image from the scanner, obtained at 90 kVp and 40 mA.

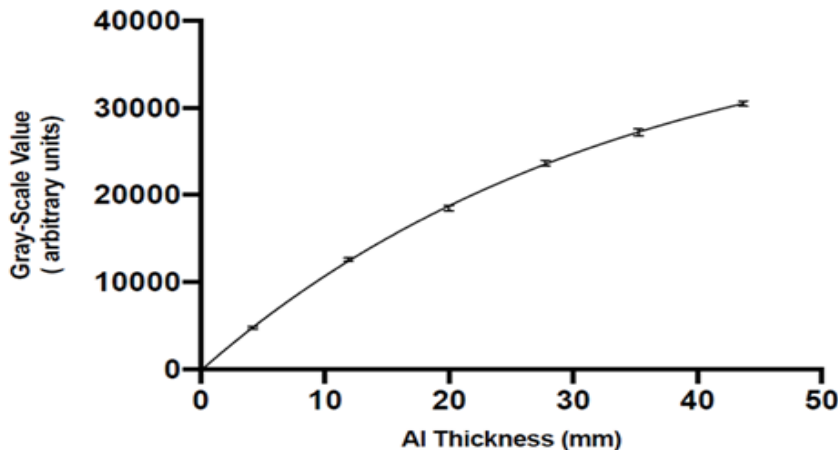


Figure 2.9: Plot of aluminum calibrator phantom thickness vs. gray-scale values. We selected relative thickness of Al phantom based on the range of our data (maximum Iohexol transmission ratio) and fitted a one phase (inverse) decay to acquired data points at the application range. The fitted function parameters were then used to create a look-up table to re-linearize the data.

2.2.7 Image Analysis

For each time point, the beam-hardening corrected projections were reconstructed into volumetric 3D data, using Feldkamp's filtered, cone-beam reconstruction algorithm [28] that is implemented in the scanner software. Custom volumes of interest (VOIs) were created in the air chamber and water-filled pocket available within each individual phantom (Fig 2.10). Relative signal intensity within the volumes of interest were measured in MicroView. Signal intensity calibration in Hounsfield units was then performed by rescaling grayscale values to arbitrarily assigned values for air and water, -1000 and 0 Hounsfield (HU), respectively.

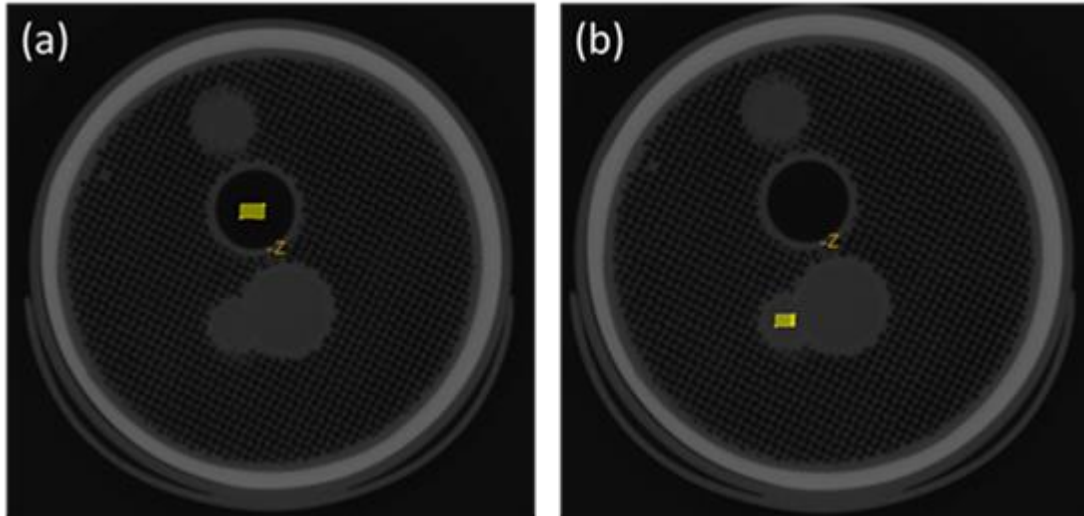


Figure 2.10: CT number calibrators. Custom regions of interest (ROIs) in (a) air chamber and (b) water-filled pocket within the phantom's lid to measure corresponding signal intensity of air and water for calibration purposes.

To increase the in-plane signal-to-noise (SNR) ratio, the volumetric data was spatially averaged along the axial direction to a voxel spacing of 5 mm.

This approach was used to reduce noise and enhance the characterization of two-dimensional (2D) radial diffusion, while maintaining in-plane resolution of 0.1 mm. (Fig 2.11). At each time point, diametric-intensity line profiles through the phantom were generated in order to visualize 2D radial diffusion over time. To reduce line profile noise, minimize the appearance of non-uniformities (*e.g.*, possible air bubbles), and enhance diffusion visualization, it was necessary to collect and average multiple line profiles. Custom software was written to generate diametric intensity line profiles, placed radially around the cylindrical phantom, and centered about the carrier core. The center of the carrier core was determined, at each time point, by computing its unweighted centroid, using a standard binary threshold technique. The diametric intensity line profiles, 65 mm in length, were sampled every 50 μm and placed radially around the carrier core at one-degree increments, in order to collect 180 profiles. The corresponding positional signal intensities of each line profile were then averaged in order to produce a single, low-noise line profile for diffusion visualization.

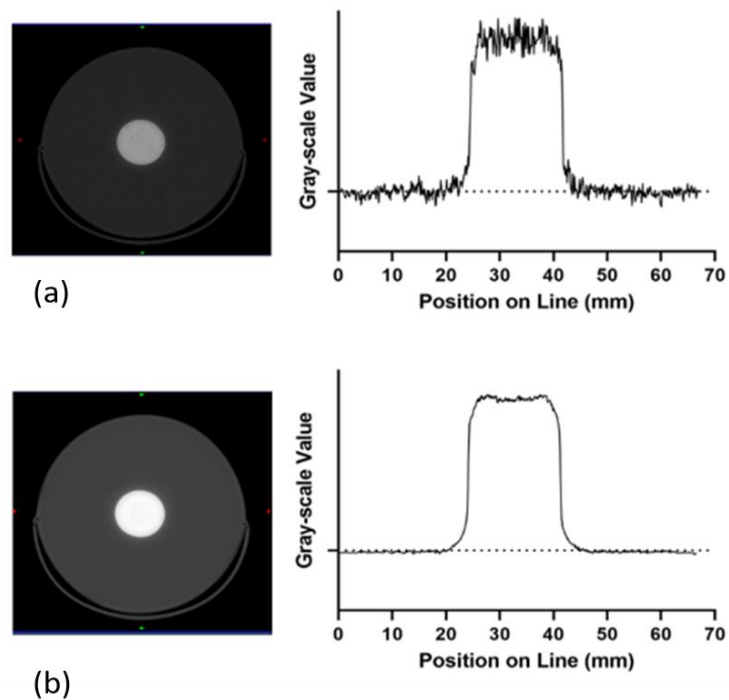


Figure 2.11: Spatial averaging of axial CT slices. Demonstrates SNR of an averaged diametric line profile through the Iohexol-loaded Stimulan[®] core in agar (a) 0.1 mm spatial voxel spacing (b) 0.1 mm in-plane and 5.0 mm axial spacing and radially averaged. Increase in signal-to-noise (SNR) ratio is observed in averaged slices in z-axis.

For analysis of single-phase diffusion, an intensity threshold was applied to determine the Iohexol radial-diffusion distance outward from the Iohexol-loaded agar core. Early time diffusion distances were obtained by adjusting a constant threshold of 300 HU and measuring the subsequent radial diffusion at each time point up to 18 hours in MicroView (MicroView 2.2, General Electric Healthcare, London, ON).

In two-phase diffusion phantoms (*i.e.*, Iohexol-loaded calcium-sulphate cores in agar annulus), we again obtained the loss of contrast agent from the inner carrier core at each time point. The custom cylindrical 3D volumes of interest within the inner cores were selected to represent the spatial and temporal distribution of contrast agent in MicroView. Mean CT numbers within the VOIs then linearly correlate with contrast agent concentration; the

cumulative release amount was calculated by the law of conservation of mass at each time-point.

2.2.8 Calculation of Diffusion Coefficient

The diffusion coefficient of the contrast agent was calculated by measuring the radial diffusion distance and cumulative release amount within single-phase and two-phase diffusion phantoms, respectively. In this work, two equations were used to calculate the diffusion coefficient of the contrast agent drug-surrogate within the single-phase (*i.e.*, Iohexol-loaded agar core in agar) and two-phase phantoms (*i.e.*, Iohexol-loaded Stimulan[®] core, or Iohexol-loaded plaster core).

The 2D diffusion equation that was used in this work represents the overall movement of particles in 2D. Although each individual molecule (particle) exhibits random Brownian motion that may not agree with the diffusion equation, as a group with the same initial and boundary conditions, they represent smooth well-behaved statistical features that can be captured by diffusion equation. In this work, instead of looking at the movement of one particle, we image many particles as a group (*i.e.*, Iohexol molecules) at each time point. Below is a brief explanation of the 2D diffusion distance evaluation that used in this work, which was described by Crank in 1975 [3].

The two-dimensional diffusion equation in Cartesian coordinates can be described as:

$$\nabla^2 P - \frac{1}{D} \frac{\partial P}{\partial t} = 0 \rightarrow \frac{\partial^2 P}{\partial x^2} + \frac{\partial^2 P}{\partial y^2} - \frac{1}{D} \frac{\partial P}{\partial t} = 0 \quad (1)$$

The function $P(x,y,t)$ gives the probability of the mean particle being present in the small vicinity of the point (x,y) at time t and named probability distribution function. In probability theory, "*A distribution holds its statistical information in the moments of the distribution.*" The constant 'D' is the diffusion coefficient of the particle in a given material and assumed to be independent of position.

The diffusion equation can be derived by the solution of the partial differential equation (PDE) using a Fourier transform. A boundary condition is applied by the assumption that at an infinite distance from where particles originally introduced, the distribution probability

should have zero chance for all times. In other words, the function P and all of its derivatives are zero at $|x| = |y| = \infty$ and we would have,

$$P(x, y, t) = A \frac{e^{\left(\frac{-(x^2+y^2)}{4Dt}\right)}}{4\pi Dt} \quad (2)$$

where (x^2+y^2) in the exponent is exactly r^2 in polar coordinates, which can represent the isotropic diffusion process on the x-y plane (*i.e.*, only the radial distance from the source matters). The solution to the 2D isotropic diffusion as presented by Crank is:

$$P(r, t) = A \frac{e^{\left(\frac{-r^2}{4Dt}\right)}}{4\pi Dt} \quad (3)$$

At first time point the molecules average position is where we originally introduce the molecules in-plane ($x=y=0$). By taking advantage of the radial symmetry, diffusion distance was presented to be linearly correlated to diffusion coefficient. In general, according to Crank solution, for n-dimensional isotropic diffusion, the mean square distance is:

$$\mathbf{R}^2 = 2 n D t \quad (4)$$

Where \mathbf{R} is radial diffusion distance (m), t is the relative diffusion time (s), and D is the diffusion coefficient ($\text{m}^2 \text{s}^{-1}$).

Diffusion distances of the contrast agent drug-surrogate were obtained from our acquired CT image data. We then plotted the mean squared radial diffusion distance as a function of time and performed linear regression within Prism (GraphPad 8.1.2 Software Inc., La Jolla, CA). By application of this equation, we can conclude that the slope of our linear regression is equal to $4D$ in two-dimensional diffusion. This approach was used to calculate the diffusion coefficient of Iohexol within agar surrounded by agar.

The diffusion coefficient of Iohexol within calcium-sulphate carrier matrices was also calculated in this work. Diffusion of Iohexol from plaster and Stimulan[®] cores in agar were obtained using a mathematical drug-delivery model for cylindrical matrix carriers. We implemented a mathematical model that describes the radial diffusion of drug molecules through the cylindrical "diffusion-controlled" drug-delivery system. A diffusion-controlled

drug-delivery system is defined as a system that is predominantly controlled by diffusional mass transport. This model has been proposed in the literature by solving Fick's second law of diffusion [1-3]. With consideration of initial and boundary conditions within the drug delivery system, different equations can be extracted and simplified to measure the approximate diffusion coefficient. The initial condition used for the model was a homogenous distribution of a drug within the carrier, forming a monolithic solution (*i.e.*, the initial drug concentration is less than the drug solubility). The boundary condition was also assumed to be "stationary," meaning that the device (*i.e.*, 2 different calcium-sulphate carriers in our experiment) dimensions are constant during diffusion [1].

Based on the initial and boundary conditions, Fick's Second Law has been solved and described by an infinite series of exponential functions [1]. In this work, we used a late-time approximation for cylindrical geometry proposed in the literature, where the diffusion coefficient can be calculated by the known cumulative amount of drug released as a function of time [1].

$$\frac{M(t)}{M(\infty)} = 1 - \frac{4}{(2.405)^2} \exp\left(-\frac{Dt(2.405)^2}{R^2}\right) \quad (5)$$

where $M(t)$ and $M(\infty)$ denote the cumulative amount of drug released at time t and in infinite time, respectively; D is the diffusion coefficient of the drug within the system, and R represents the radius of the inner core cylinder. Sets of experimental data were then fitted to this equation to calculate the diffusion coefficient.

Cylindrical volume of interest (VOIs) were placed at the inner core of each phantom at various time points. The relative CT number was measured automatically in MicroView. We then used the linear relation between the CT numbers and concentration to obtain relative concentration remaining in the inner core as a function of time. To agree with the law of conservation of mass, the amount released can then be calculated by subtracting the amount remaining in the core from the initial concentration measured at the first scan time for each phantom.

Prism (GraphPad 8.1.2 Software Inc., La Jolla, CA, USA) was used, and the image data were fitted to the equation No.5 to calculate diffusion coefficient.

2.3 Results

2.3.1 CT Measurements

The initial CT numbers (HU) and standard deviations (HU) were measured in each of the volumes of interest (VOIs) within the phantoms in MicroView, (as shown in Table 2.1). Measured CT numbers were then used to linearly correlate the subsequent contrast agent concentration at each time point to the CT numbers within each diffusion phantom. Custom VOIs were selected at the first scan time within the inner core of each diffusion and control phantoms. CT numbers at the outer edge of agar, sink annulus were also measured that represent pure agar. All agar values at the annulus at first scan time showed similar CT number. This result verifies the consistency of agar composition within different phantoms.

Table 2.1: CT numbers measured within each phantom. Custom volumes of interest were selected at the first the scan time (*i.e.*, 1.25 hours after phantom fabrication) within each diffusion phantom.

phantom	Core CT Number (HU)	SD (HU)	Annulus CT Number (HU)	SD (HU)
Iohexol-loaded Agar	1380	±24	-32	±15
Iohexol-loaded Stimulan [®]	2490	±48	-30	±18
Iohexol-loaded Plaster-of-Paris	2485	±50	-32	±20
Pure Stimulan [®]	1780	±32	-32	±16
Pure Plaster-of-Paris	1790	±28	-33	±20

2.3.2 Diffusion Visualization

CT image data at each time point provides direct visualization of small-molecule diffusion within the intact phantoms, due to the fact that corrected image signal intensity is linearly correlated with Iohexol concentration. Images from CT volumes at different time points within each phantom are consistent with that expected for the diffusion of molecules from a finite-source into a surrounding medium. Diffusion proceeds, as expected, from higher to

lower values across a concentration gradient. In our experiments, the flux of diffusion was observed from inner-core matrices that had a higher concentration of Iohexol contrast agent drug-surrogate into the agar sink at the periphery. For Iohexol-loaded agar cylindrical cores within agar, images of CT axial slices showed almost uniform concentration of Iohexol after 76.0 hrs. (Fig 2.12).

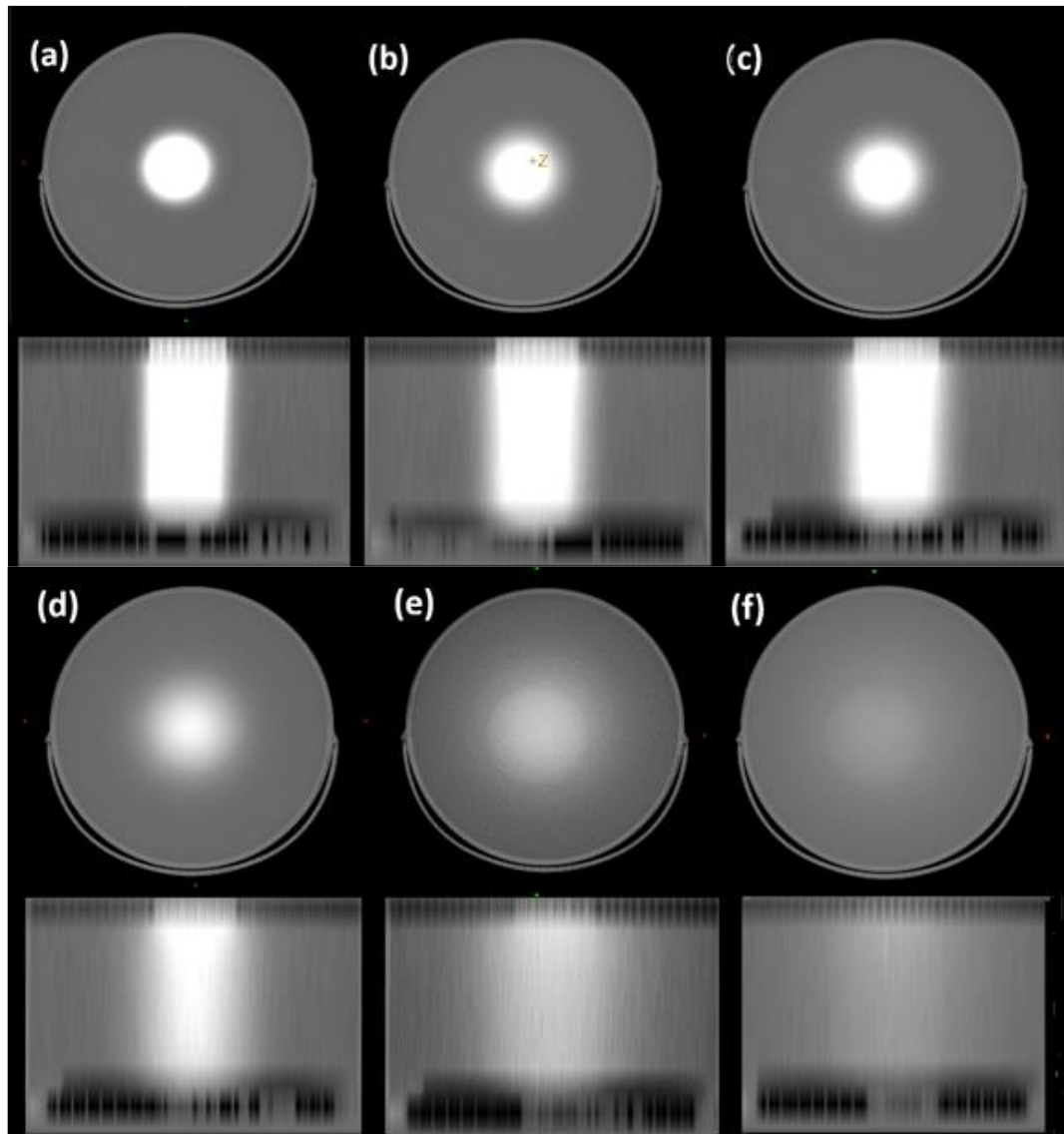


Figure 2.12: CT slices of Iohexol loaded agar cylindrical core in agar. Diffusion process of Iohexol contrast agent drug surrogate was characterized by down-gradient propagation, spreading and smoothing over time (a) 1.25 hrs, (b) 5.08 hrs, (c) 8.08 hrs, (d) 18.08 hrs, (e) 47.58 hrs, (f) 76.08 hrs after phantom fabrication. CT axial slices showed almost uniform concentration of Iohexol after 76.0 hrs.

The diffusion rate of the contrast agent was also observed in the two calcium sulphate-based matrices, either a Stimulan® or plaster-of-paris core within an annular agar sink. These CT images showed a much slower diffusion rate of Iohexol from both calcium sulphate-based carriers, while both carriers exhibited similar diffusion characteristics (Fig 2.13) In these cases, the cylindrical core was still visible at late time points, due to the inherent contrast provided by the remaining calcium-sulphate carrier.

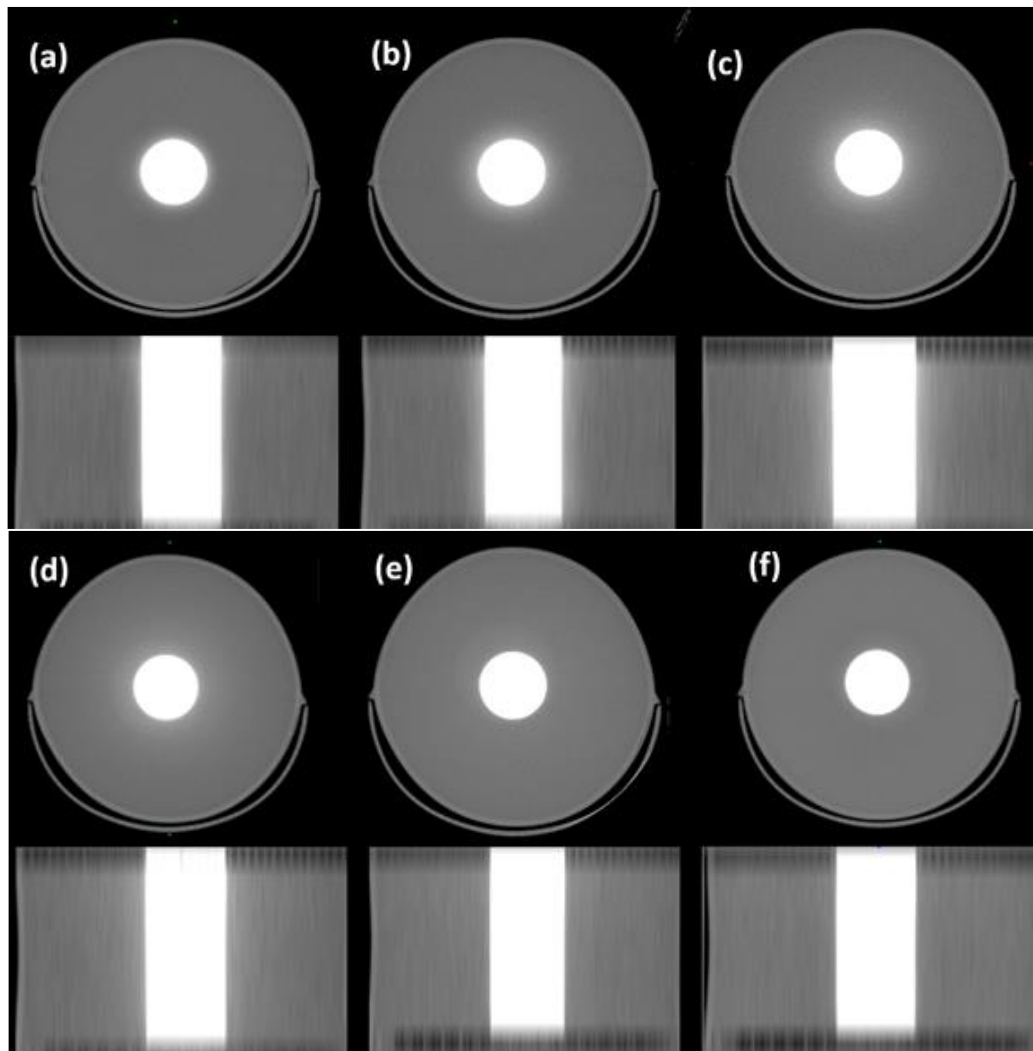


Figure 2.13: CT slices of Iohexol loaded Stimulan® cylindrical core in agar. Iohexol contrast agent drug surrogate diffuses slowly from the core into pure agar. Contrast agent diffuses from the core primarily over the first 120 hours and remains relatively stable between 435 and 600 hours. a) 1.25 hrs, (b) 8.25 hrs, (c) 24.0 hrs, (d) 70.25 hrs, (e) 121.50 hrs, (f) 607.25 hrs after phantom fabrication.

2.3.3 Quantitative Analysis of Line Profiles

Diametric line profiles across CT axial slices represent the corresponding signal intensity (and hence contrast concentration) within each pixel along the line at that axial location; moreover, CT signal intensity variation is linearly correlated with contrast agent propagation within the phantom [23, 24]. Thus, diametric line profiles can be used to characterize two-dimensional (2D) radial diffusion of contrast agent drug-surrogate diffusion from inner-core matrices into the peripheral agar tissue-equivalent sink.

CT diametric line profiles *versus* position in pixels were plotted for each time point in Prism (GraphPad 8.1.2 Software Inc., La Jolla, CA). Data were plotted for each phantom at various time points, with the curves superimposed to compare relative 2D radial diffusion of the contrast-agent drug surrogate through each of the carrier matrices.

Slow diffusion of Iohexol contrast agent from the Stimulan[®] core carrier and plaster core carrier was observed, compared to the Iohexol-loaded agar core (Fig 2.14). In this case, contrast agent diffuses from the calcium-sulphate core primarily over the first 120 hours and remains relatively stable between 435 and 600 hours. The sharp boundary between the calcium sulphate cores and the agar periphery was visible at all-time points; this was due to the fact that the signal intensity in the core cannot be reduced below the offset value of the pure calcium sulphate carrier (*e.g.*, 1780 HU). Similar time-dependent line profiles were observed for the Iohexol-loaded plaster of Paris core; these data were visually indistinguishable from the Stimulan[®] results. Both of the calcium sulphate based carriers were scanned for up to 25 days, to ensure that we observed the entire process of diffusion. At early time points, Iohexol molecules diffused initially from the boundary of Iohexol-loaded cores, which are in contact with the surrounding sink agar. This can be observed in CT line profiles through axial CT slices. In these cases, the cylindrical core value can not fall below the absolute CT number of pure plaster of paris and Stimulan[®].

The evolution of contrast-agent concentration over time for the Iohexol-loaded agar core within agar is shown in Fig 2.15. In this case, we observe a reduction in signal intensity within the core, with a concurrent radial spread into the agar annulus. We also observe rapid blurring of the boundary between the core and annulus, with Gaussian-like line profiles after 3 – 5 hours. There is a significant reduction of Iohexol concentration in the core after 76

hours, approaching a uniform contrast-agent concentration across the entire phantom, consistent with rapid diffusion.

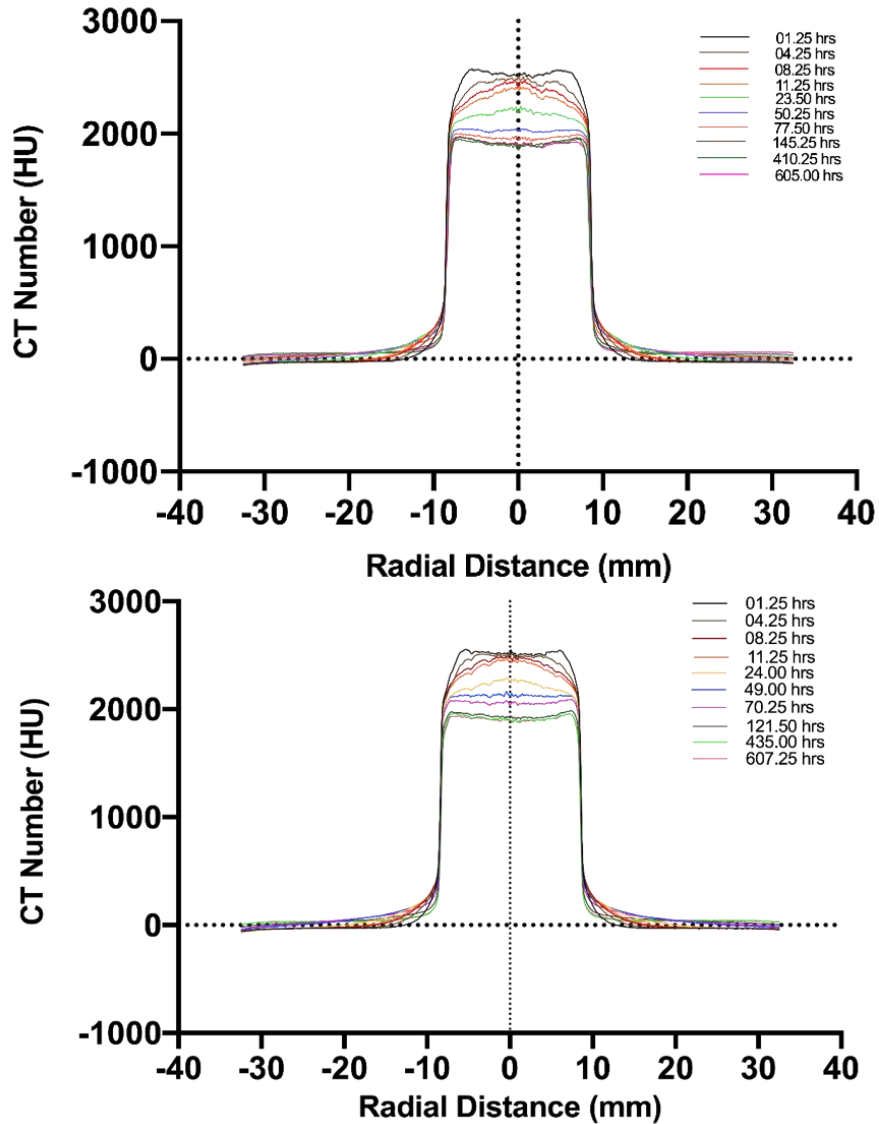


Figure 2.14: Two-dimensional (2D) diametric line profiles within an axial CT slice. (a) Iohexol-loaded Stimulan[®] cylindrical core and (b) Iohexol-loaded Plaster cylindrical core surrounded by pure agar sink phantom at different time points. Iohexol contrast agent drug surrogate diffused from core into agar periphery. Diffusion from the core was reduced to a negligible value within approximately 145 hrs after phantom fabrication.

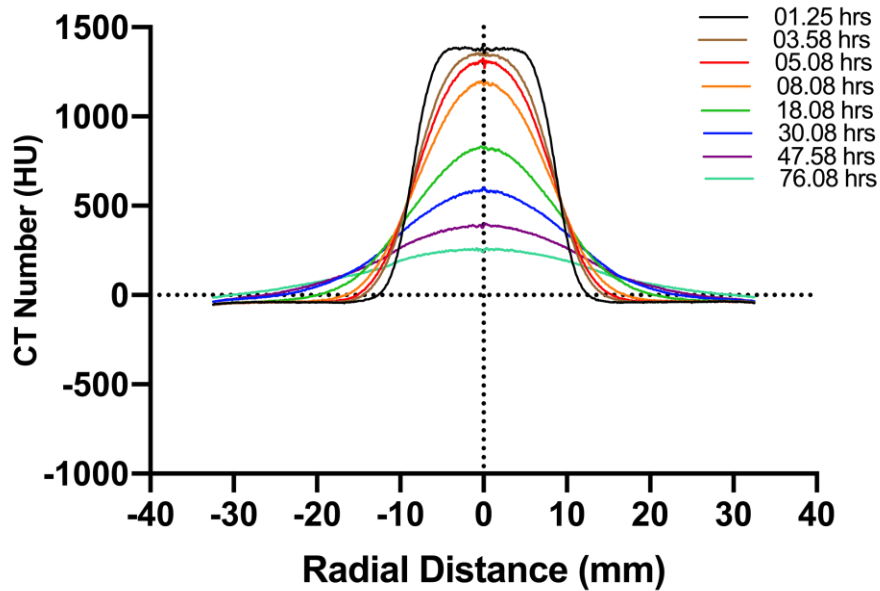


Figure 2.15: Two-dimensional (2D), diametric, line profiles through an axial CT slice in Iohexol-loaded cylindrical agar core surrounded by a pure agar sink at various time points. Iohexol contrast agent drug surrogate diffused from the agar core into the agar periphery. The Iohexol concentration observed within the phantom was significantly reduced 76.0 hrs after phantom fabrication.

2.3.4 Calculation of Iohexol Concentration

Linear correlation was used to estimate contrast agent concentration at the inner cores over different time intervals [23, 24]. Inner core signal intensity (CT numbers) were obtained in the control phantoms; pure agar, Stimulan[®] and plaster that correspond to -30 ± 18 , 1780 ± 32 , 1790 ± 28 Hounsfield unit, respectively. All control phantoms contain zero concentration of Iohexol contrast agent. Inner core CT numbers were also measured within Iohexol-loaded agar, Iohexol-loaded Stimulan[®] and Iohexol-loaded plaster cores. Linear regression then was applied in order to correlate the measured CT numbers to the subsequent concentration of contrast agent drug-surrogate.

Linear regression results for iodine can be expressed as an equation $S(i) = 47 \frac{ml}{mg} \times C_i - 32$ where S is the signal intensity in (HU), and C_i is the iodine concentration in mg/ml.

2.3.5 Diffusion Coefficient Calculation

The quantitative CT signal intensity data can be used to derive the diffusion coefficient from both single-phase and two-phase diffusion phantoms. The estimate of the diffusion coefficient in a single-phase diffusion experiment (*i.e.*, Iohexol-loaded agar, cylindrical core, in agar) was derived from the analysis of 2D (*i.e.*, radial) diffusion distance over time, as described in Equation 4. In this case, the early-time diffusion distance (R) was derived from the CT images shown in Fig. 2.12, using a constant gray scale threshold to determine the radial extent at each time point. These data were then used to determine the diffusion coefficient, based on linear regression (Fig. 2.16). The linear regression shows an excellent fit ($R^2 > 0.99$), allowing accurate determination of the slope, which is equal to $4D$ in two-dimensional diffusion, where D is the diffusion coefficient ($m^2 s^{-1}$). The derived diffusion coefficient, in this case, was $2.26 \times 10^{-10} m^2 s^{-1}$, which compares well with literature values of $2.5 \times 10^{-10} m^2 s^{-1}$ for Iohexol in water [30].

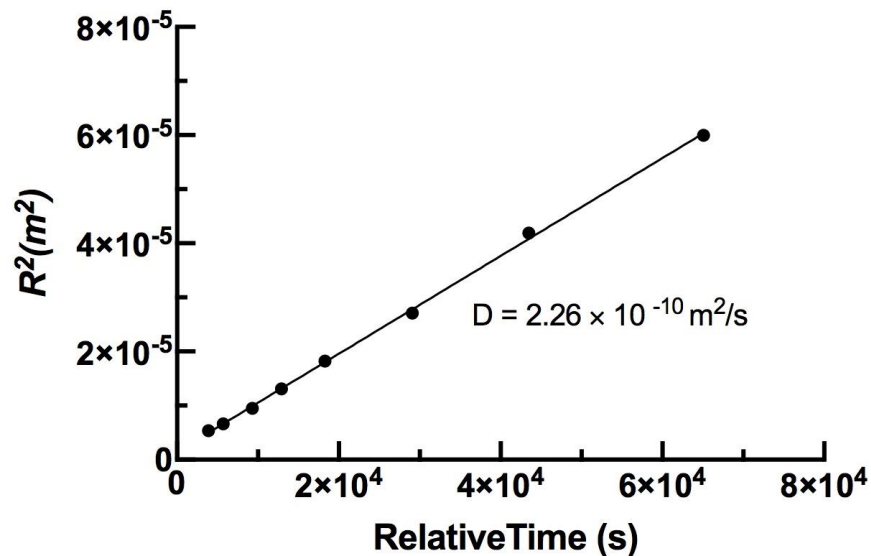


Figure 2.16: Linear regression plot of radial diffusion distance vs. time. The slope of the line represents $4D$ in two-dimensional diffusion in Iohexol-loaded agar core in agar. The derived diffusion coefficient was equal to $2.26 \times 10^{-10} m^2 s^{-1}$.

The estimate of the diffusion coefficient in a two-phase diffusion experiment (*i.e.*, Iohexol-loaded calcium-sulphate matrices, in agar) was derived from the calculation of the cumulative release amount of the contrast agent drug-surrogate at each time point by measuring the inner core loss. The cumulative release amount was calculated based on the known inner core CT number, the linear relation between CT number and contrast concentration, and the law of mass conservation. We then fit the cumulative release data to the mathematical model for quantification of drug release from monolithic solutions (Eq.5); the diffusion coefficient was then derived from the non-linear fit to this equation (Fig. 2.17), with an $R^2 > 0.99$. Using this approach, we derived diffusion coefficients of $0.46 \times 10^{-10} \text{ m}^2 \text{ s}^{-1}$ and $0.85 \times 10^{-10} \text{ m}^2 \text{ s}^{-1}$ for Iohexol incorporated in Stimulan[®] and plaster cores, respectively.

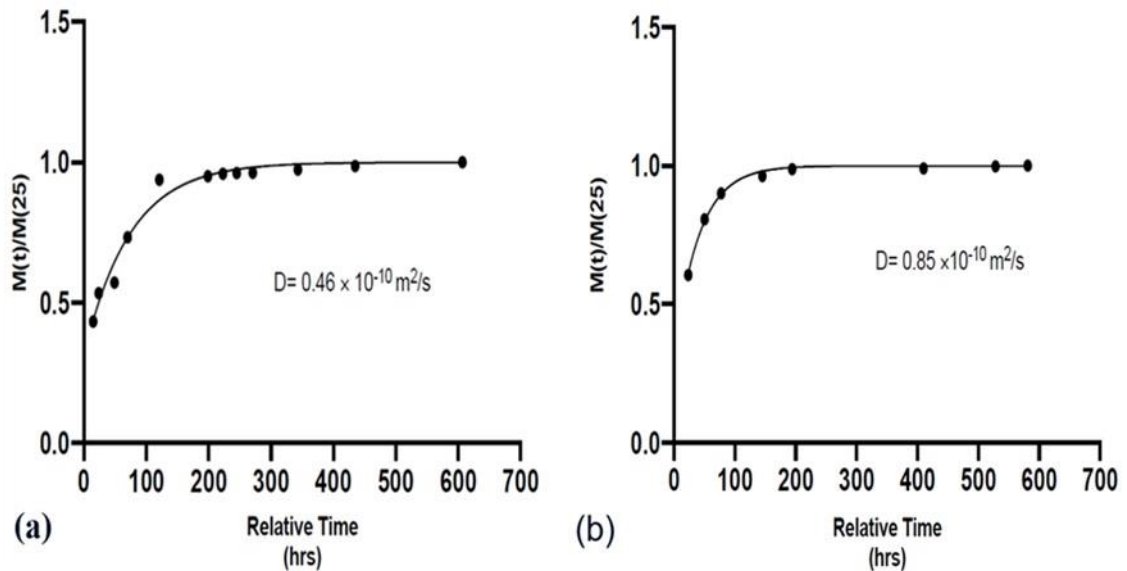


Figure 2.17: Plot of the cumulative release of Iohexol contrast agent vs. time, (a) Iohexol-loaded Stimulan[®] in agar (b) Iohexol-loaded Plaster in agar. diffusion coefficients of $0.46 \times 10^{-10} \text{ m}^2 \text{ s}^{-1}$ and $0.85 \times 10^{-10} \text{ m}^2 \text{ s}^{-1}$ were calculated for Iohexol incorporated in the Stimulan[®] and plaster cores, respectively.

2.4 Conclusion

2.4.1 Image-based Diffusion Characterization

We have successfully developed a non-invasive, non-destructive, quantitative, micro-CT technique to characterize real-time diffusion of small-molecules within an intact phantom. We have shown that previously described mathematical approximations of diffusion phenomena can be used to describe release kinetics from predominantly mass-diffusion controlled delivery systems [1, 31]. We were able to fit our image-based diffusion data set to mathematical models of diffusion and thereby calculate the diffusion coefficient. Our micro-CT technique has improved in-plane signal-to-noise ratio, allowing us to more accurately estimate two-dimensional diffusion of a small-molecule contrast agent, acting as a drug surrogate. The short scan time (*i.e.*, five minutes) enabled us to minimize the amount of diffusion that was occurring during each scan, while reducing exposure to a high X-ray dose. X-ray dose should be considered in future applications of this method in animal models and clinical testing. Iohexol is one of the most common CT contrast agents, and it was demonstrated in this work that it provides sufficient signal-to-noise ratio to characterize relative diffusion during longitudinal scanning. Radial diffusion distance was obtained by the application of a standard binary threshold technique at each time point for agar core. Since CT numbers are correlated with the contrast agent concentration, it was also possible to determine the mass loss of the contrast agent drug surrogate from the carrier core over time. This provides a quantitative estimate of the cumulative release of contrast agent at each time point. To the best of our knowledge, this is the first time that a CT-based, non-invasive technique has been used to quantify small-molecule diffusion, with specific applications in improving local drug delivery for ODRI.

The diffusion coefficients of Iohexol were calculated to be $2.26 \times 10^{-10} \text{ m}^2 \text{ s}^{-1}$ in agar, $0.46 \times 10^{-10} \text{ m}^2 \text{ s}^{-1}$ in Stimulan[®], and $0.85 \times 10^{-10} \text{ m}^2 \text{ s}^{-1}$ in plaster cylindrical carriers. As expected. Iohexol molecules exhibited a higher diffusion rate in the water-based, carrier (*i.e.*, agar) compared to the calcium-sulphate based carriers (*i.e.*, Stimulan[®] and plaster). Both calcium-sulphate carriers exhibited similar relative diffusion characteristics over time, allowing us to substitute plaster for Stimulan[®] in future experiments (and thereby reducing the cost of research investigations in calcium-sulphate matrices). The diffusion coefficients for the two

forms of calcium sulphate were found to be slightly different in this study. This may be explained by the fact that Stimulan[®] is a highly-purified, medical-grade synthetic recrystallized calcium sulphate alpha-hemihydrate, while conventional plaster is the beta-hemihydrate form of calcium-sulphate [32].

2.4.2 Limitations

There are certain limitations of this study; in this work, we used Iohexol, and we assumed that Vancomycin follows relatively similar diffusion characteristics compared to Iohexol. As we have described, the concept of tracking a surrogate molecule is not new; fluorescein (MW 332 Da) has been used as an optical tracer to study elution in calcium-sulphate carriers and PMMA in ODRI, for example [12]. Our approach instead used an x-ray contrast agent (Iohexol), with a molecular weight of 821 Da, which is much closer to that of commonly used antibiotics in ODRI treatment, such as Vancomycin (MW 1449 Da).

Our *in-vitro* micro-CT test was performed under static conditions that did not include fluid flow, load, or other stresses to which carriers are exposed *in vivo*. These factors would likely affect the release of drug-surrogate molecules from each of the various materials. We observed 2D diffusion characteristics. However, 3D evaluation would improve our understanding of small-molecules diffusion within asymmetrical delivery carriers.

During the release of antibiotics from PMMA-based carriers, drug diffusion is the predominant process, however, calcium-sulphate carriers are also biodegradable. Therefore, resorption within these carriers is expected to increase the apparent rate of diffusion and this process requires further consideration. Saturation of the surrounding tissue sink may also affect the diffusion rate of drugs in local treatment. There are also different types of clinically approved calcium-sulphate carriers, and this study only tested one (*i.e.* Stimulan[®]).

2.4.3 Applications

This study provided a controlled environment for the diffusion of a drug surrogate from a finite source into a finite tissue-equivalent sink, which simulates the *in-vivo* conditions of antibiotic delivery in ODRI treatment. However, the diffusion study was carried out *in vitro* using intact phantoms. In the future, this approach can be applied to non-invasive characterization of diffusion *in-vivo*, including animal models and clinical studies. Our

technique can be very helpful, since it eliminates the need for invasive sampling of tissue and enables us to non-invasively track and understand different mechanisms that ultimately may affect drug release kinetics in animal models or clinical testing (*e.g.*, resorption, carrier swelling). By developing this micro-CT technique, we were able to obtain appropriate signal intensity and concentration information to facilitate diffusion characterization of a contrast-agent drug surrogate within various calcium-sulphate and agar carriers. This work could be furthered by testing other types of carriers, such as PMMA bone cement (which is already used clinically as an antibiotic carrier in two-stage revision surgery for infected orthopedic implants) and calcium-phosphate carriers.

This micro-CT method also positions us to characterize the elution kinetics of small molecules from enhanced carriers within a porous metal scaffold [25-28]. A highly-porous metal scaffold may lead to a breakthrough in local antibiotic therapy for ODRI, as the scaffold can separate the competing needs for mechanical strength, by providing structural support while maintaining appropriate drug elution characteristics. Unfortunately, the presence of a metal scaffold introduces the need for imaging artifact correction in micro-CT. Thus, our future work (Chapter 3) will validate micro-CT diffusion measurements with a drug-surrogate loaded carrier within the metal scaffold. We will also evaluate sequential diffusion measurements near intact metal scaffolds in two dimensions. Further investigation of the efficacy of a highly porous, metal scaffold containing antibiotic-eluting calcium-sulphate is also needed, with the overarching goal to develop more effective revision implants for ODRI management.

Our methods for elution tracking are flexible and can be applied to any contrast agent to mimic various antibiotics, or for studies employing entirely different imaging modalities. It may also be possible to extend the principles of non-invasive image-based methods for studying diffusion to include the use of gadolinium-based MRI contrast agents, such as Magnevist[®] (Bayer, Leverkusen, Germany) which has a molecular weight of 938 Da. The artifact reduction (*i.e.* smaller signal void and lower field inhomogeneity) resulting from the high porosity of the metal scaffold may potentially allow for quantitative susceptibility mapping to reproduce the results of this study. Although MR-based contrast agent tracking is unlikely to surpass the accuracy of micro-CT, MRI is likely to be commonly used for monitoring patients in the clinic, due to excellent soft-tissue contrast and the lack of ionizing

radiation. Further investigations into the use of clinical CT are also required, in order to establish clinical relevance.

2.4.4 Summary

In this work, we have presented a quantitative micro-CT technique that can be used to monitor the diffusion of small-molecules in an intact phantom. This technique has the advantage that diffusion data can be obtained directly during longitudinal scans without the need for invasive sampling of the tissue-equivalent sink, unlike previous studies that are based on invasive sampling techniques [33-36]. CT measurements can facilitate quantitative prediction of radial diffusion distance over time and cumulative amount of drug-surrogate released from a finite-source into a controlled environment. These diffusion data can be obtained by observing the subsequent CT value at each time point within volumes of interest. We have shown that simple, mathematical approximations can be used to quantitatively describe the drug release from a predominantly mass-diffusion controlled delivery system in the absence of other factors that may affect diffusion (*e.g.*, drug carrier resorption). Further studies of diffusion of small molecules will help us to better understand the elution kinetics of various drugs that are being used in local treatment. This will help us reach the long-term goal of the development of more effective drug-delivery systems for local therapy.

2.5 References

1. Siepmann, J. and F. Siepmann, *Modeling of diffusion controlled drug delivery*. J Control Release, 2012. **161**(2): p. 351-62.
2. Watson, E.B., K.H. Wanser, and K.A. Farley, *Anisotropic diffusion in a finite cylinder, with geochemical applications*. Geochimica et Cosmochimica Acta, 2010. **74**(2): p. 614-633.
3. J., C., *Diffusion_Crank-Mathematics of Diffusion*. second ed. 1975: CLARENDON PRESS.
4. McConoughey, S.J., et al., *Biofilms in periprosthetic orthopedic infections*. Future Microbiol, 2014. **9**(8): p. 987-1007.
5. Kurtz, S.M., et al., *Are We Winning or Losing the Battle With Periprosthetic Joint Infection: Trends in Periprosthetic Joint Infection and Mortality Risk for the Medicare Population*. J Arthroplasty, 2018. **33**(10): p. 3238-3245.
6. McConoughey, S.J., et al., *Comparing PMMA and calcium sulfate as carriers for the local delivery of antibiotics to infected surgical sites*. J Biomed Mater Res B Appl Biomater, 2015. **103**(4): p. 870-7.
7. harnish patel, D.R.P., Upendra Pael, Tushar Brahmhatt, Mayur Sathar, *Matrix Type Drug Delivery System: A Review*. Journal of pharmaceutical science and bioscience research (JPSBR), 2011. **1**(3): p. 143-151.
8. Paz, E., et al., *Evaluation of Elution and Mechanical Properties of High-Dose Antibiotic-Loaded Bone Cement: Comparative "In Vitro" Study of the Influence of Vancomycin and Cefazolin*. J Arthroplasty, 2015. **30**(8): p. 1423-9.
9. Slane, J., B. Gietman, and M. Squire, *Antibiotic elution from acrylic bone cement loaded with high doses of tobramycin and vancomycin*. J Orthop Res, 2018. **36**(4): p. 1078-1085.
10. Stevens, C.M., et al., *An articulated antibiotic spacer used for infected total knee arthroplasty: a comparative in vitro elution study of Simplex and Palacos bone cements*. J Orthop Res, 2005. **23**(1): p. 27-33.
11. Gasparini, G., et al., *Drug elution from high-dose antibiotic-loaded acrylic cement: a comparative, in vitro study*. Orthopedics, 2014. **37**(11): p. e999-1005.
12. Dusane, D.H., et al., *Effects of loading concentration, blood and synovial fluid on antibiotic release and anti-biofilm activity of bone cement beads*. J Control Release, 2017. **248**: p. 24-32.

13. Frankel, R.I., *Centennial of Rontgen's discovery of x-rays*. West J Med, 1996. **164**(6): p. 497-501.
14. Seibert, J.A. and J.M. Boone, *X-ray imaging physics for nuclear medicine technologists. Part 2: X-ray interactions and image formation*. J Nucl Med Technol, 2005. **33**(1): p. 3-18.
15. Hounsfield, G.N., *Computerized transverse axial scanning (tomography). 1. Description of system*. Br J Radiol, 1973. **46**(552): p. 1016-22.
16. Romans, L.E., *Computed Tomography for Technologists: A Comprehensive Text*. 2010: Lippincott Williams & Wilkins.
17. Kalender, W.A., *X-ray computed tomography*. Phys Med Biol, 2006. **51**(13): p. R29-43.
18. Badea, C.T., et al., *In vivo small-animal imaging using micro-CT and digital subtraction angiography*. Phys Med Biol, 2008. **53**(19): p. R319-50.
19. Schambach, S.J., et al., *Application of micro-CT in small animal imaging*. Methods, 2010. **50**(1): p. 2-13.
20. Ritman, E.L., *Small-animal CT - Its Difference from, and Impact on, Clinical CT*. Nucl Instrum Methods Phys Res A, 2007. **580**(2): p. 968-970.
21. Wang, Y., et al., *Micro-CT in drug delivery*. Eur J Pharm Biopharm, 2010. **74**(1): p. 41-9.
22. Szymanski-Exner, A., et al., *Noninvasive monitoring of local drug release using X-ray computed tomography: optimization and in vitro/in vivo validation*. J Pharm Sci, 2003. **92**(2): p. 289-96.
23. Wang, L., et al., *Correlation between CT attenuation value and iodine concentration in vitro: discrepancy between gemstone spectral imaging on single-source dual-energy CT and traditional polychromatic X-ray imaging*. J Med Imaging Radiat Oncol, 2012. **56**(4): p. 379-83.
24. Du, L.Y., et al., *A quality assurance phantom for the performance evaluation of volumetric micro-CT systems*. Phys Med Biol, 2007. **52**(23): p. 7087-108.
25. Brooks, R.A. and G. Di Chiro, *Beam hardening in x-ray reconstructive tomography*. Phys Med Biol, 1976. **21**(3): p. 390-8.
26. Edey, D.R., et al., *Extending the dynamic range of biomedical micro-computed tomography for application to geomaterials*. J Xray Sci Technol, 2019. **27**(5): p. 919-934.

27. Valencia, D.P. and F.J. González, *Understanding the linear correlation between diffusion coefficient and molecular weight. A model to estimate diffusion coefficients in acetonitrile solutions*. Electrochemistry Communications, 2011. **13**(2): p. 129-132.
28. Feldkamp, L.A., L.C. Davis, and J.W. Kress, *Practical cone-beam algorithm*. Journal of the Optical Society of America A, 1984. **1**(6): p. 612-619.
29. Souza, R., et al., *Standard operating procedure to prepare agar phantoms*. Journal of Physics: Conference Series, 2016. **733**: p. 012044.
30. Mohammad, M., et al., *Diffusion Coefficient of Iodide ions in Aqueous Medium and in Vacuum: an Appraisal*. Journal- Chemical Society of Pakistan, 2015. **37**.
31. Mircioiu, C., et al., *Mathematical Modeling of Release Kinetics from Supramolecular Drug Delivery Systems*. Pharmaceutics, 2019. **11**(3).
32. Oliver, R.A., et al., *Application of Calcium Sulfate for Dead Space Management in Soft Tissue: Characterisation of a Novel In Vivo Response*. Biomed Res Int, 2018. **2018**: p. 8065141.
33. Bishop, A.R., et al., *Vancomycin elution, activity and impact on mechanical properties when added to orthopedic bone cement*. J Mech Behav Biomed Mater, 2018. **87**: p. 80-86.
34. Aiken, S.S., et al., *Local release of antibiotics for surgical site infection management using high-purity calcium sulfate: an in vitro elution study*. Surg Infect (Larchmt), 2015. **16**(1): p. 54-61.
35. Samuel, S., et al., *In vitro study of elution kinetics and bio-activity of meropenem-loaded acrylic bone cement*. J Orthop Traumatol, 2012. **13**(3): p. 131-6.
36. Kim, T.W.B., et al., *3D printed liner for treatment of periprosthetic joint infections*. Med Hypotheses, 2017. **102**: p. 65-68.

Chapter3

3 Mechanical Properties and Diffusion Characterization of Highly Porous 3D-printed Scaffolds

3.1 Introduction

As describe in Chapter 1, there are unmet needs in the area of orthopedic-device-related-infection (ODRI), which includes infections near fracture fixation components in trauma surgery [1-4], as well as peri-prosthetic joint infection (PJI) near orthopedic components (*e.g.*, hip, knee and shoulder joint replacements) [5-8]. Infection is a growing problem in orthopedic surgery and is now the number one reason for early revision of hip and knee replacements [9]. Local antibiotic delivery is commonly used as a gold-standard treatment to eliminate infection in ODRI; however, it is often associated with poor clinical outcomes [10]. Poly (methyl methacrylate) bone-cement spacers are currently the most common carriers for local antibiotic delivery in PJI. PMMA provides a level of mechanical strength for temporary application in weight-bearing joints (*i.e.*, ultimate strength of 70 MPa), however, with limited capacity to be loaded with high-dose antimicrobial agents. It also exhibits relatively poor antibiotic elution kinetics [11]. Hence, several alternative approaches have been proposed to enhance local antibiotic delivery in PJI. Application of calcium sulphate-based and calcium phosphate-based materials as antibiotics carriers can be considered as a practical approach to overcome the poor elution kinetics of PMMA. These carriers exhibit enhanced elution characteristics [12, 13], however, they exhibit poor mechanical properties in comparison to PMMA. They are weak and brittle with low compressive strength; this is a barrier for these carriers to be considered as a replacement for current PMMA carriers, and, as a result, their application in PJI management has remained limited [14].

We propose an alternative approach for PJI management, using carriers that maintain sufficient mechanical properties while incorporating a higher dose of the antimicrobial agent within their structure and also exhibit improved elution characteristics. We proposed that highly porous 3D-printed metal structures can be utilized for PJI management; these structures can provide sufficient mechanical properties for load-bearing applications while being capable of delivering antimicrobial agent to the target tissue due to their associated

open pores. In this chapter, we investigate the development of hybrid structures, incorporating a highly porous metal scaffold that can support virtually any carrier material, with high-dose antimicrobial agents loaded into the carrier. This approach separates the competing needs for mechanical strength and appropriate drug elution characteristics and may lead to a breakthrough in local antibiotic therapy for PJI.

Biological materials are often porous; they exhibit optimized multi-functional structuring, size-effect strengthening and high interconnectivity [15]. Recent advances in additive manufacturing (*i.e.*, laser powder-bed fusion) have enabled fabrication of porous metal structures with such biological features and appropriate mechanical properties [16, 17]. Porous structures based on a gyroid lattice have been introduced to provide significant advantages for orthopedic applications [18]. These porous structures can be manufactured by laser powder-bed fusion in metal alloys. Gyroid-based scaffolds allow the adjustment of mechanical properties, provide improved compressive fatigue resistance due to the lack of stress concentrations, and may exhibit superior mass-transport properties [6, 18]. For these reasons we believe that gyroid-based porous structures could be used to fabricate orthopedic components with appropriate mechanical properties and high delivery capacity. This may help in the development of a novel single-stage treatment strategy in PJI management. It may be possible that such a scaffold could integrate into bone and be retained after an infection is cleared, unlike current temporary spacers (*i.e.*, PMMA), which must be replaced in a second operation.

In this chapter, our first objective is to design a highly porous, 3D-printed gyroid-based scaffold that can provide sufficient mechanical support and can be loaded with enhanced antibiotics carriers (*e.g.*, calcium sulphate). Such scaffolds can be designed with modifications to parameters to achieve porosity (*i.e.* void fraction) over the range of 60 to 90%. These values fall within the range that can be fabricated in metal using 3D-printing and approximate the porosity of trabecular bone (50% - 90%) [19]. It will be essential to verify that the porous scaffolds we design will maintain sufficient strength; thus, the mechanical properties of our scaffold designs will be determined computationally by the application of the finite-element method (FEM). Laser powder-bed fusion will then be used to fabricate porous cylindrical gyroid-based scaffolds out of titanium alloy (Ti-6Al-4V). Our long term goal is to test our porous metal designs with material testing equipment (according to

ISO5833 [11]) and verify an ultimate strength greater than 100 MPa, compared to PMMA with an ultimate strength of 70 MPa. With these properties, we believe that the scaffold could integrate into bone (due to resorption of carrier and subsequent osseointegration) and be retained after an infection is cleared.

Our second objective is to characterize the diffusion of small molecules from calcium-sulphate based carriers embedded within the porous metal scaffold. As described in chapter 2, we have developed a novel technique to measure small-molecule diffusion in an intact phantom. Here, we will use our quantitative micro CT-based technique to evaluate diffusion through a gyroid-based scaffold. Ultimately, this scaffold design, combined with the use of enhanced medical-grade calcium-sulphate carriers (*i.e.*, Stimulan[®], Biocomposites, Keele, U.K.), could provide a solution to current challenges in infection treatment in ODRI.

3.1.1 Gyroid-based Structures

Cellular/lattice structures can exhibit better material properties (*e.g.*, structural strength) as well as enhanced mass transport properties, compare to their bulk counterparts [20]. These structures can be used in many biomedical applications. The mass transport property is an essential feature for lattice structures when they are to be applied in applications such as the development of drug delivery systems. Cellular/lattice structures have high interconnectivity; this enhances their application as filling structures [17]. The pore networks of such structures can be designed to reduce resistance to mass transport, shortening the diffusion path, and increasing interconnectivity. Among cellular/lattice structures, the gyroid has promising mass-transport properties; for example, Ma *et al.* report that the gyroid structure has better interconnection and accessibility of fluids than a hexagonal structure [21] and has the potential for application in bone-mimicking scaffolds.

The gyroid is a member of cellular/lattice structures that has been considered in different biomedical applications such as orthopedic (*i.e.*, bone-mimicking scaffolds) as well as tissue-engineering applications [16, 17, 22]. Gyroid-based structures naturally exist in many different systems in stable forms, such as butterfly wing scales [23], cell membranes [16, 24], and block copolymers [25]. The gyroid is a member of triply periodic minimal surfaces (TPMS) that divide space into two continuous phases [16]. The area fractions occupied by the structure are approximately the same for various cross-sections, regardless of the cell size

in gyroid-based lattices [26]. A TPM surface is a minimal surface that is repeated continuously in three independent directions, which has constant mean curvature of zero at all points. The symmetry of the elements can also be used to design various TPMS-based geometries. In 1970, the gyroid was introduced by Alan Schoen, and he identified gyroid surfaces as belonging to a family of triply periodic minimal surfaces that is free of self-intersections (*i.e.*, their edges never cross each other) [27]. The gyroid has relatively good mechanical properties compared to other TPMS cellular structures, and is one of the most effective TPMS that can be utilized to create structures with robust mechanical performances [15]. The gyroid structure also exhibits isotropic elasticity [17]. Moreover, such lattices provide the advantage of a porous, open structure without significant stress concentrations [18]. The gyroid is a highly adjustable structure with respect to mechanical strength and a specific target architecture can be achieved by parametric design modification (*e.g.*, changes to unit cell size, wall thickness/pore size); this provides control over the porosity and hence mechanical strength that is an advantage in orthopedic applications.

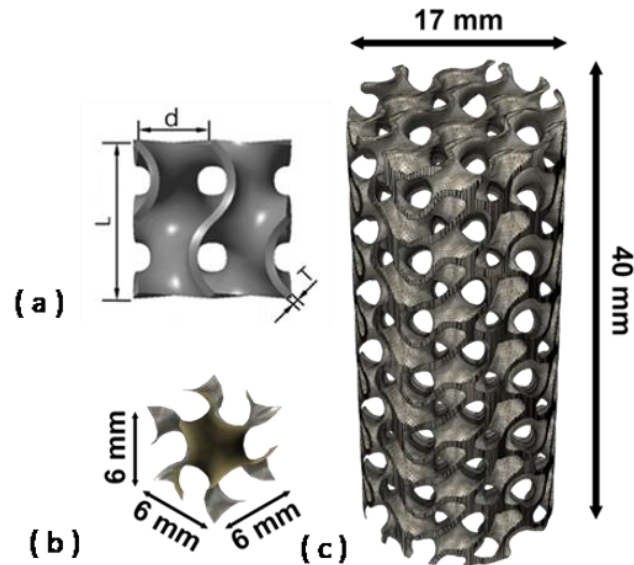


Figure 3.1: Schematic of Gyroid-lattice structure, (a) shows one unit cell of a gyroid structure where d is the pore size, T is the wall thickness and L is the length; (b) The unit cell with the length of 6 mm that was used in this work; (c) three-dimensionally volume rendering of a unit cell forming a cylindrical structure of 17 mm diameter \times 40 mm length.

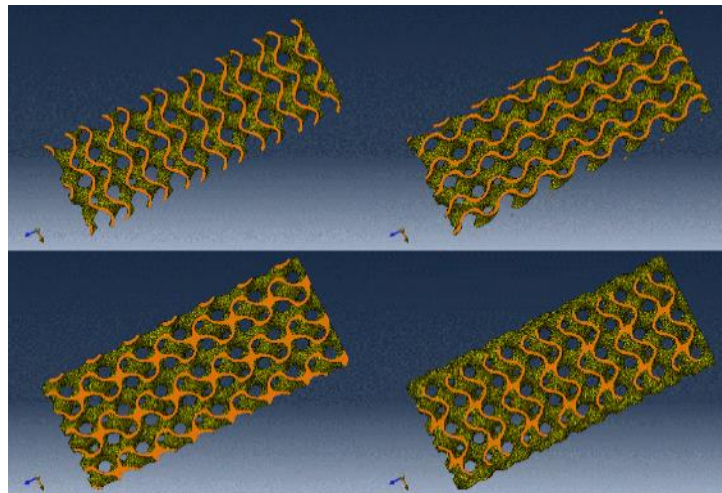


Figure 3.2: Load-bearing surfaces of a gyroid-based cylinder at various cross sections. Various cross-section shapes viewed from in plane shift of the two-dimensional cross-section. The area fractions occupied by the structure are approximately the same for all cross-sections.

3.1.2 Selective Laser Melting

Traditional manufacturing methods such as casting, machining, and metal injection molding have been used to fabricate porous metal scaffolds. However, these approaches provide limited control over microarchitecture and surface features [28]. Although some metallic lattice structures can be manufactured using traditional processes, using conventional methods to fabricate complex structures like gyroid-based scaffolds is challenging [17]. In this work, the fabrication of gyroid-based scaffolds was explored through an additive manufacturing technique. Additive manufacturing is a collection of new manufacturing techniques that allow layer-by-layer fabrication of three-dimensional (3D) structures. Recent developments in additive manufacturing have made the fabrication of complex structures possible. One example of a potential application that is in our interest is the ability to fabricate porous metal gyroid-based structures that can be used in ODRI treatment.

Various cellular metal structures are manufactured by utilizing 3D printing (*i.e.*, laser-power bed fusion) [17]. Laser-power bed fusion is a promising laser-based additive manufacturing technique in which an object is built layer-by-layer using a laser, heaters, and powdered materials. By using laser-power bed fusion, we can fabricate scaffolds with complex geometry, and we are able to convert a computer model into an actual structure directly with high precision. In this technique, a focused laser beam is used to selectively melt thin layers of metal powders together (*e.g.*, Ti-6Al-4V); once the scanning of a layer is completed, a new layer of powder is deposited, and fabrication of a new layer starts. This process is repeated until the complete specimen is created [29]. Medical-grade Ti-6Al-4V is one of the metals that can be successfully processed through laser-power bed fusion manufacturing. It is notable that triply periodic minimal surface structures like the gyroid are also self-supporting, which is another advantage for fabrication by laser powder-bed fusion (*i.e.*, minimal supports or no supports are required when 3D-printed) [17].

In this work, we used a metal 3D printer (AM 400, Renishaw plc, UK) at the Additive Design in Surgical Solutions (ADEISS) Centre at Western University to fabricate our gyroid-based structures. This machine has a laser power of 400 W with a laser spot size of 70 μm and a layer thickness of 40 μm , and it is able to print parts using metal powder with 15-45 μm

grain diameter. This printer can be used to build complex medical-grade metal components directly from three-dimensional design computer files (*e.g.*, STL).

3.1.3 Finite element method

The finite element method (FEM) is a numerical method for analyzing complex engineered structures. This numerical approach has been used for several years and can solve differential equations, based on continuum mechanics models. This method can describe the characteristics of engineered structures with complex initial and boundary conditions that are impossible to examine using conventional numerical methods. In FEM, a complex structure is broken down into a finite number of smaller pieces (elements), and the governing equations are then formulated. These elements are then assembled to model the mechanical behaviour of the structure [30]. Complex shapes or geometries (such as the gyroid) can be discretized into a series of elements with known geometry and deformation behaviour within a three-dimensional mesh. For example, in the case of static analysis, forces are applied to the mesh model, creating deformation at the nodes of the elements that provide relative values for displacement and stress distribution on the structure. Material properties must also be assigned prior to the finite element solution. In this work, we performed a finite element method on our gyroid-based structures to evaluate the displacement and stress distribution under compression, for a range of porosities. We used a commercial FE software package (ABAQUS, Dassault Systèmes, Vélizy-Villacoublay, France) for our loading simulations.

3.2 Material and Methods

3.2.1 Design of Porous Gyroid-based Cylinders

The design of the gyroid-based prototype was achieved using open-source software (Blender 2.78 3D software). The dimension of the unit cell was selected based on the previous literature that has evaluated the mechanical properties of Gyroid structures for orthopedic applications [18]. We also aimed to achieve optimum porosity, while preserving the mechanical properties at an acceptable range for use in drug delivery.

A unit cell size of 6 mm × 6 mm × 6 mm in the three orthogonal directions (length × width × length) was selected. The gyroid-based structure was designed by 3D rendering of the unit cell. Due to the symmetry of the surface, unit cells were patterned in three directions (x, y, z)

to achieve a cuboid structure of 18 mm × 18 mm × 42 mm. The cuboid gyroid-based scaffold was further transformed into a cylindrical structure using Boolean intersection with a cylinder (17 mm diameter x 40 mm high).

In this work, we used wall thickness as a controlling parameter to vary the porosity of the final scaffold. We created five gyroid-based cylinders with porosity consistent with that observed in trabecular bone (*i.e.*, 50% - 90% [19]). We set the wall thickness of each cylindrical gyroid-based structure to 0.85, 0.60, 0.40, 0.30, and 0.20 mm (denoted as G01, G02, G03, G04, and G05, respectively). These cylindrical gyroid-based structures represent approximate porosity of 60%, 70%, 80%, 85%, and 90%, respectively (Table 3.1).

The STL file that was exported from Blender did not provide sufficient triangle quality and connectivity to be suitable for import, volume meshing, and loading in ABAQUS (Dassault Systèmes, Vélizy-Villacoublay, France). These issues arise from the Boolean intersection operation in Blender, which was used to create the cylindrical object from the rectangular lattice of repeated gyroid unit cells. Additional improvements to the triangulated gyroid-based surface model were required in order to satisfy conditions necessary for ABAQUS to produce a high-quality volume mesh. The desired mesh must exhibit sufficient resolution to capture geometric features adequately and to also accurately resolve stress and strain gradients during mechanical loading simulation. The STL file was imported into Geomagic Studio (3D Systems, Rock Hill, SC, USA) for additional processing. Prior to surface mesh improvement, a 0.2 mm thick section was removed from each end of the model by bisecting with planes perpendicular to the long axis of the gyroid-based cylinder. The planar surfaces resulting from this at the ends of the model were required for proper uniform distribution of loading in simulation. Triangle improvement was carried out using a process of Laplacian smoothing, triangle subdivision, and decimation with any geometric issues being corrected *via* an automated verification tool contained in the software application between each step. Once completed, and the geometry of the final model's validity confirmed, the final model was exported once again in STL format for subsequent import into ABAQUS for tetrahedral volume meshing and finite element analysis (FEA) setup.

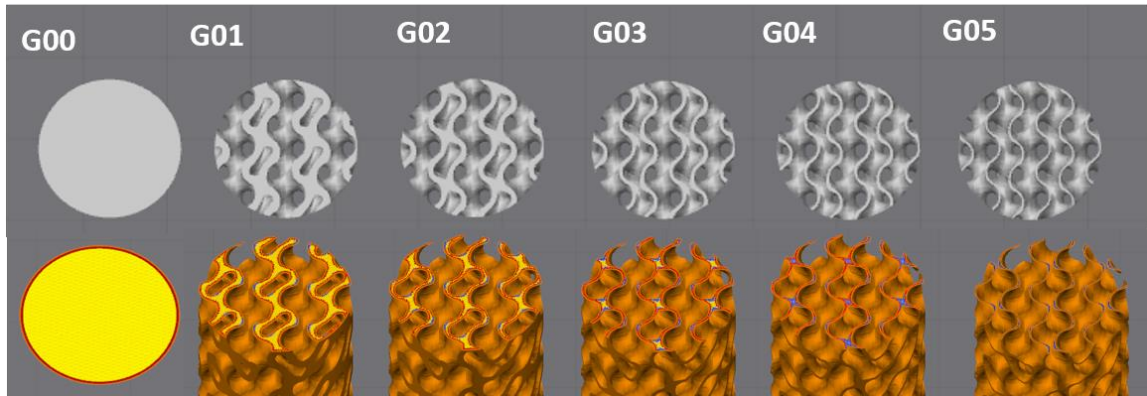


Figure 3.4: Top surface of gyroid-based cylinders of 17 mm diameter and 40 mm length with various porosity. Renderings illustrate altering of the wall thickness and porosity: G00) 0%, G01) 60%, G02) 70%, G03) 80%, G04) 85%, G05) 90%. All gyroid-based cylinders were designed by periodically repeating a unit cell of 6 mm in length in 3 principal spatial directions (x,y,z).

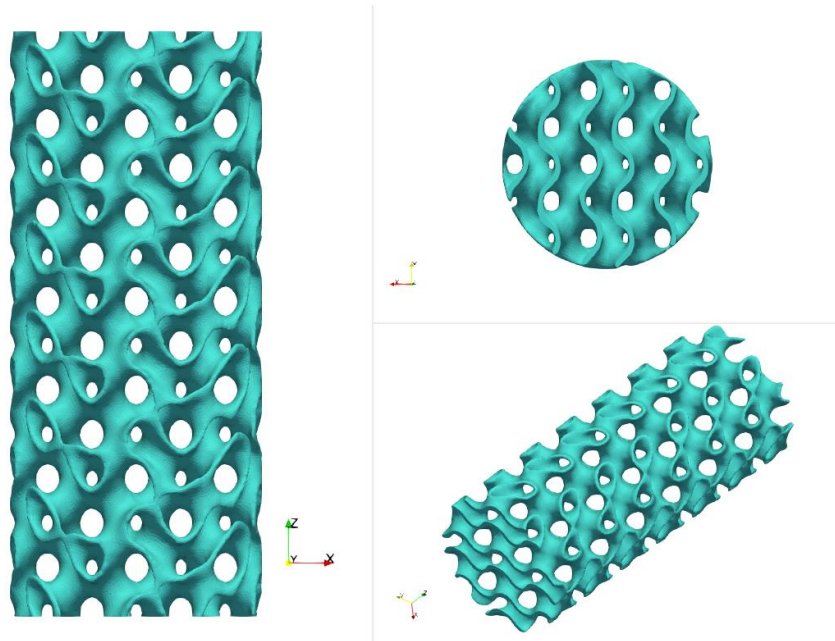


Figure 3.3: 3D rendering of Gyroid cylinder of 17 mm diameter and 40 mm length. Unit gyroid cell of 6mm in length was repeated to create a cuboid structure, and truncated to a cylinder using open-source design software (Blender 2.78 3D software).

Table 3.1: Gyroid-based cylindrical scaffolds (17 mm diameter and 40 mm length) with varying porosity ranging from (60-90%)

Gyroid Cylinders	Unit cell Length (mm)	Porosity %	Wall Thickness (mm)
G01	6	60.02	0.85
G02	6	70.14	0.60
G03	6	79.83	0.40
G04	6	84.60	0.30
G05	6	89.70	0.20

3.2.2 Finite Element Analysis of Gyroid-based Cylinders

Mechanical performance of cylindrical Gyroid-based structures with porosity ranging from 60% - 90% were investigated under static compression load using a computationally finite element method (FEM). The stress distribution, displacement, and effective uniaxial elastic moduli were obtained by the commercially available finite element analysis software (ABAQUS, Dassault Systèmes, Vélizy-Villacoublay, France). The results from FEM analysis were used to select the optimum porosity for the fabrication of a porous scaffold in titanium alloy (*i.e.*, Ti-6Al-4V) and to perform a diffusion characterization experiment using micro-CT.

Three-dimensional (3D) designs of the cylindrical gyroid-based scaffolds of various porosity were imported into commercial finite-element analysis software (ABAQUS, Dassault Systèmes, Vélizy-Villacoublay, France) for model assembly and loading simulation. Loading and boundary conditions were consistent in all various designs of Gyroid cylinders. All the samples were subjected to only a static compression load.

We applied a 10 kN compression load in the Z-direction as a ramp load with a step size of 0.001 per increment as the initial increment and the maximum increment of 0.5. ABAQUS

software automatically controls the increments in between that are used during the solution. In contact simulation, it is important to start with small initial increments to allow the software to increase the increment based on the shared nodes at contact surfaces. A distributed compression load was applied on the top surface of the gyroid-based cylinders (Fig 3.5). A rigid plate with dimensions of 5 mm height (H) \times 19 mm length (L) \times 19 mm width (W) was created to apply the distributed compression load on the top surface of the cylinders. A full-contact interface between the plate and gyroid-based cylinder surface was defined during the compression process. The material property of the plate was assigned to be equivalent to elastic homogenous stainless steel (*i.e.*, SS316L) with modulus of elasticity of 193 GPa and a uniform Poisson's ratio of $\nu=0.25$. Each cylindrical structure was solved for displacement in the direction of the applied static compression load. As described, the increment solution available in the ABAQUS software was used to perform the compression ramp load; cylinders were gradually loaded from 0% to 100%. The boundary condition for the loading plate was displacement-rotation, and only one-degree of freedom was allowed in the load direction.

Boundary conditions were applied on the cylinders for the finite-element analysis; the

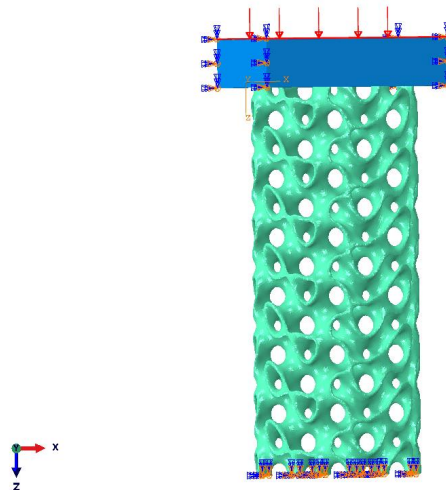


Figure 3.5: Compression load and boundary condition of the gyroid-based cylinder. A uniform distributed load of 10 kN was applied on a stainless-steel plate, the boundary condition for the plate is displacement-rotation and only one-degree freedom is allowed in the load direction. The cylinder is fully constrained at the bottom, while expansion of lateral surfaces is free to occur.

cylinders were rigidly fixed (*i.e.*, fully constrained) at the bottom to prevent rotation and displacement in all degrees, but lateral expansion of all the samples was free to occur.

The material properties for the metal within the porous cylindrical scaffolds were set to correspond to linear elastic homogeneous titanium alloy (*i.e.*, Ti-6Al-4V) with modulus of elasticity of 113.8 GPa and a uniform Poisson's ratio of $\nu=0.342$.

Linear, four-node tetrahedral elements were chosen for all simulations, which ensured high material resolution within the elements of the FE models while maintaining reasonable simulation times [31], typically on the order of 4 hours per simulation. Surfaces of Gyroid cylinders were meshed with an element size of 0.25 mm. This allowed for an accurate representation of the specific gyroid geometry and was found to be sufficient for representing von Mises stress (*i.e.* maximum value changes are smaller than 1%). To ensure convergence of this contact simulation, an increase in mesh density on contact surfaces was configured, along with the use of small computation increments in the software.; elements on the contact surfaces were allowed to be smaller (*i.e.*, 0.15 mm) to guarantee the convergence. Elements were connected to adjacent elements by nodes, thereby creating numerical representations of the object geometry. The total number of elements was at a range of 1.4 - 1.6 million for this simulation (depending on specific porosity). 8-node first-order linear hexahedral elements were used for the plate, due to the simple geometry and to reduce the computational cost.

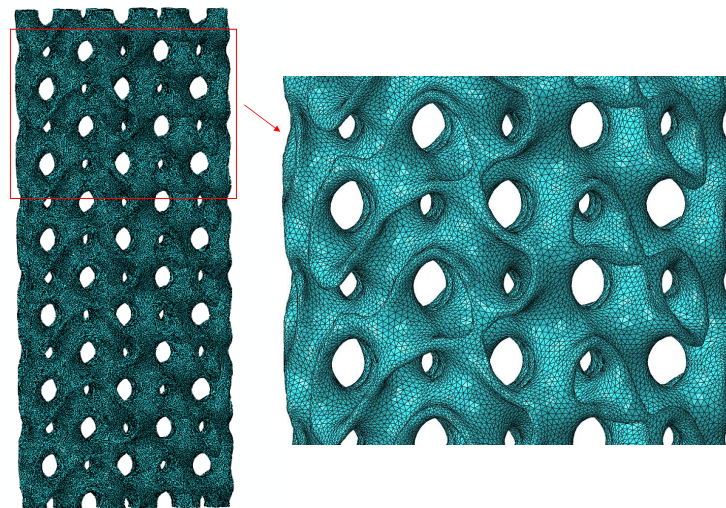


Figure 3.6: Finite element mesh of a gyroid-based cylinder. The cylinder was discretized by linear, 4-node tetrahedral elements

von Mises stress distribution under compression (and the resulting displacement in the load direction) were obtained from the finite-element analysis for each cylindrical gyroid-based structure. Previous literature has shown that the effective elastic modulus of a structure that contains voids would be the ratio of the average stresses to the average strains that result in the structure when it is subjected to pure compression on its outer boundary [32]. We have approximated our porous cylindrical gyroid-based structures as homogenous elastic bodies which contain periodically distributed voids of a common geometry (*i.e.*, gyroid cell unit). The effective (apparent) elastic modulus of each porous cylindrical structure was then calculated by imposing the obtained displacement of each porosity under 10 kN compression load into an equivalent homogeneous solid cylinder. Note that the apparent elastic modulus calculated in this way is equivalent to compressive stiffness, for a homogeneous isotropic material.

The porous gyroid-based cylinders were substituted with a solid cylinder of the same dimension (*i.e.*, 17 mm × 40 mm) in order to estimate the effective elastic moduli in ABAQUS finite element software. The distributed ramp compression load of 10 KN was applied on the top surface of the solid cylinder by a stainless-steel plate. The boundary conditions were also consistent with the analysis of the porous gyroid-based structures. The solid cylinder was fully restricted for displacement or rotation in any degree of freedom at the bottom surface while the lateral surfaces were free to expand. The available obtained displacement values for each porous gyroid-based cylinder were then applied to the equivalent homogenous solid cylinder, and the subsequent effective elastic moduli for each porosity were calculated.

3.2.3 Additive Manufacturing of Gyroid Cylinders

A metal 3D printer in the Additive Design in Surgical Solutions (ADEISS) Centre at Western University was used to manufacture porous gyroid-based cylinders, using laser power-bed fusion. A commercial 3D metal printer (AM400, Renishaw plc, UK) was used for the fabrication process. This printer provides the capability of printing layers with a thickness of 40µm. Porous gyroid-based cylinders were fabricated out of powdered Ti6Al4V ELI-0406 alloy; this alloy comprises titanium mass fraction up to 90% with an average particle size of 15-45µm in diameter. Ti6Al4V was processed at the elevated melting temperature under

400 W laser power with a beam size (*i.e.*, laser spot size) of 70 μm . This printer provides an inert atmosphere, achieved by creating a vacuum before backfilling with high purity argon gas through sealed and welded chambers to minimize the oxidation of the metal powder during the printing process. Support filaments of 400 μm were used to anchor the printed components to the build platform; these support filaments are crucial for the successful completion of printing. When the entire part has been printed layer by layer as described in the introduction, samples then undergo a standard heat treatment process for densification and relief of any residual stresses. Heat treatment affects the mechanical properties of 3D-printed objects; with post-heat-treatment on fabricated objects, fatigue life will be increased, and objects will exhibit enhanced ductility [33]. Over the course of 60 minutes, the temperature was raised to 350°C and held at this temperature for 30 minutes. The annealing continued by increasing the temperature to 850°C, which takes 60 minutes. The 3D-printed structures were then kept at 850 °C for 60 minutes. Objects were then left undisturbed to cool down naturally. Heat treatment was performed while the cylinders were still attached to the build platform. After heat treatment, components were detached from the build plate by manually cutting the support structure. Trapped loose powder was removed by ultrasonic cleaning in a bath of pure ethyl alcohol, and cylinders were shot-blasted to minimize the surface roughness. The mass of each fabricated gyroid-based cylinder was then obtained by weighing the printed objects on a scale with 1 mg precision.

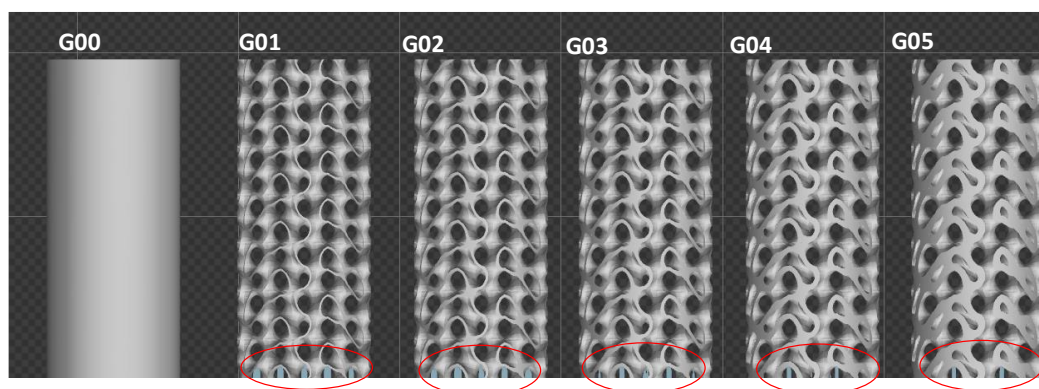


Figure 3.7: Schematic of gyroid-based cylinders of 17 mm diameter and 40 mm length with various porosity on the 3D-printer build-plate. G00) 0%, G01) 60%, G02) 70%, G03) 80%, G04) 85%, G05) 90%. The cylinders are attached to the build platform through support structures (blue filaments inside red circle) of 400 μm . Support filaments are built using the same Ti6Al4v powder to avoid warping and distortion that may occur

3.2.4 Diffusion Characterization Within the Gyroid-based Cylinder

The overall goal of this work is to develop a 3D-printed porous gyroid-based titanium scaffold that provides structural support while simultaneously incorporating carrier materials to enhance small-molecule diffusion kinetics. Thus, we investigated small-molecule diffusion in a 3D-printed metal gyroid-based cylinder with 80% porosity (*i.e.*, G03). We utilized the quantitative micro-computed tomography (micro-CT) technique that was described in Chapter 2 to track the diffusion of a surrogate tracer molecule. This approach can help us to better evaluate mechanisms of antibiotics elution, and to characterize the changes in elution due to the presence of the metal scaffold. As in Chapter 2, we used a radiographic contrast agent (*i.e.*, Iohexol, molecular weight 821) as a drug-surrogate for one of the commonly used antibiotics in PJI treatment. (*i.e.*, Vancomycin, molecular weight 1449 Da).

Plaster-of-Paris (DAP, Scarborough, Ontario, Canada) was shown in Chapter 2 to exhibit diffusion characteristics similar to commercially available medical-grade calcium-sulphate carriers (Stimulan® Rapid Cure, Biocomposites, Keel, UK). For this reason, we used Plaster-of-Paris as a cost-effective substitute for Stimulan® to evaluate relative diffusion of small

molecules through a calcium sulphate-based carrier matrix that had been introduced into the gyroid-based porous scaffold.

We observed the diffusion of Iohexol drug-surrogate in a two-part cylindrical phantom consisting of a gyroid-based cylinder that was loaded with Iohexol carrier and surrounded by pure agar acting as a tissue-equivalent sink. This phantom was fabricated with the same dimensions that were described in Chapter 2 to maintain consistency between all diffusion experiments. To obtain Iohexol at a concentration of 30 mg/ml, we diluted 1.0 ml of full-strength Iohexol (Omnipaque 300, GE, Healthcare, Oakville, ON) with 9.0 ml of de-ionized water. 10 ml of Iohexol (30 mg/ml) was then mixed with 18.5 g of plaster powder. The mixture was hand-mixed to achieve a homogenous paste. The paste was introduced into the porous gyroid-based cylinder (17 mm diameter \times 40 mm length) with a 10 ml syringe. A 3D-printed PLA mold was used to position the cylinder in place during the injection of an Iohexol-loaded plaster paste. Cylinder G03 with 80% porosity was selected to ensure sufficient porosity for loading the drug-surrogate carrier, while retaining appropriate mechanical properties. The loaded cylinder was then kept undisturbed at room temperature for 60 minutes.

We used the same standard formulation that was described in Chapter 2 to prepare the agar [34]. The gyroid-based porous cylinder (*i.e.*, G03) was centered in the custom, 3D-printed, PLA container-mold that was shown in chapter 2, Figure 2.5d. We poured pure agar into the container to form an annular sink surrounding the porous cylinder. Air and water chambers within the mold were used for CT calibration purposes, as described in Chapter 2.

A micro-CT scanner (eXplore speCZT, General Electric Health Care, London, Ontario) was used for diffusion characterization. Image acquisitions were completed on the speCZT at an X-ray tube voltage of 90 kVp and tube current of 40 mA, with a large focal spot in an 8.9 cm bore. For each scan, 900 views were obtained at 0.4° increments over a 360° rotation of the gantry at an exposure time of 16 ms per frame. These scan parameters resulted in an acquisition duration (*i.e.*, scan time) of approximately 5 minutes. Scans were acquired with $50 \times 50 \times 50 \mu\text{m}$ voxel spacing. The scan acquisition parameters were kept consistent with the diffusion experiments that were described in Chapter 2. Scanning was similarly performed at 1.25, 4.25, 8.25, 11.25, 23.5 hours after fabrication, then every 24 hours for the

next seven days and finally every 2 days for a further 17 days. Time zero was assumed to be at the time of casting the Iohexol-loaded gyroid-based cylinder within the outer pure agar annulus in the custom 3D printed PLA container.

We then applied a beam-hardening correction (BHC) algorithm to the acquired projections prior to reconstruction [35]. The main cause of metal artifacts is the high attenuation of metallic objects, which leads to X-ray beam-hardening of the polychromatic X-ray spectrum and signal under-ranging [36]. For each time point, the corrected projections were reconstructed into volumetric 3D data, using Feldkamp's filtered cone-beam reconstruction algorithm [37], which is implemented in the scanner software. Reconstructed three-dimensional (3D) images were all averaged $2 \times 2 \times 2$, result in final $100 \times 100 \times 100 \mu\text{m}$ isotropic spatial resolution. Gray-scale values were rescaled to arbitrarily assigned values for air and water, -1000 and 0 Hounsfield (HU), respectively. To increase the in-plane signal-to-noise (SNR) ratio, the volumetric data were spatially averaged in the Z-axis to a slice spacing of 5mm to characterize the two-dimensional (2D) radial diffusion. The in-plane resolution was maintained at 0.1 mm.

The loss of Iohexol contrast agent drug-surrogate from the porous Gyroid core was obtained by measuring the corresponding CT number within the core at each time point. CT numbers are assumed to linearly correlated with Iohexol concentration [38]. The diffusion coefficient of the Iohexol drug-surrogate from the plaster carrier within the porous gyroid-based cylinder was obtained by fitting the image data to the equation that was fully-described in Chapter 2 and shown below [39, 40]:

$$\frac{M(t)}{M(\infty)} = 1 - \frac{4}{(2.405)^2} \exp\left(-\frac{Dt(2.405)^2}{R^2}\right) \quad (1)$$

The cumulative release amount of Iohexol tracer from the porous gyroid-based core into the agar annulus was obtained at each time-point, based on the gray-scale values measured within the core and the assumption of mass conservation. The image data was then fitted to Equation 1 using non-linear Levenberg Marquardt fitting in Prism (GraphPad 8.1.2 Software, Inc., La Jolla, CA).

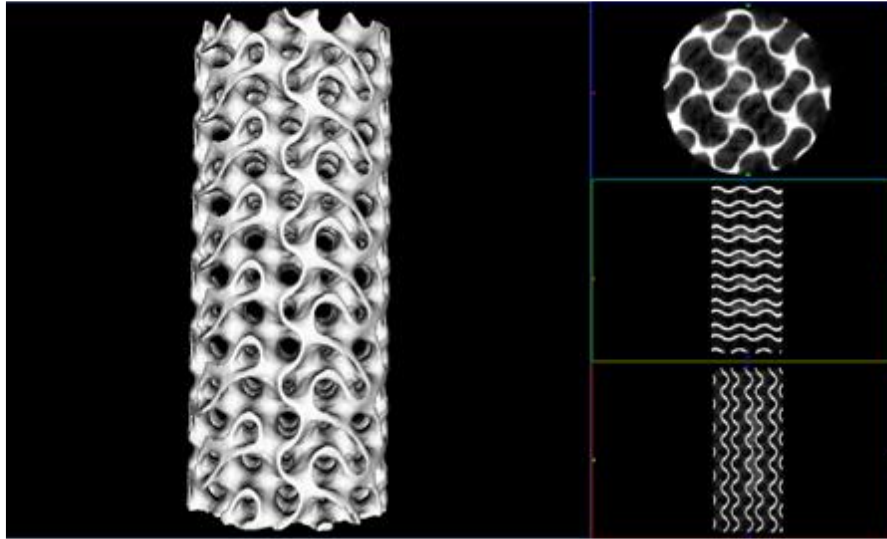


Figure 3.8: CT volume of gyroid-based cylinder with 80% porosity (G03) acquired by isosurface volume rendering after beam hardening correction (BHC). The images on the right show that the correction algorithm has resulted in significant reduction of metal artifacts.

3.3 Results

3.3.1 Finite Element Results

Von Mises stress distribution and subsequent displacement in the load direction under a 10 KN compression force were obtained in ABAQUS software for all gyroid-based cylinders. We assessed the effect of varying porosity on the von Mises stress distribution. Calculated von Mises stress within the cylinder were compared to the yield strength of Ti6Al4V alloy (equal to 970 MPa in compression [41]) to select a porosity that would be appropriate for the CT-based diffusion experiment.

The maximum stress value in the FE result represented a single element in the mesh that was seen to be on the edge of the contact surface between the gyroid-based cylinder and the load plate for all porosity values. This artifactually high stress value was due to a limitation in optimizing the mesh at the top surface of the gyroid, and also limitations in bisecting the top surface with a plane perpendicular to the long axis of a cylinder, as described in the design section (3.2.1). This value was significantly higher than the values within the cylinder volume.

Artificially high-stress values were also observed at the outer surface of the gyroid-based cylinders due to the application of a Boolean operation to intersect the cylinder and the cubic volume design. This process resulted in connected bridges at the outer surface with no support underneath, and these locations correspond to significantly high-stress values in FE simulation (Fig 3.9).

As the artificially elevated maximum von Mises values observed at the outer surfaces were due to design, meshing and memory limitation, they were excluded from further analysis in this work.

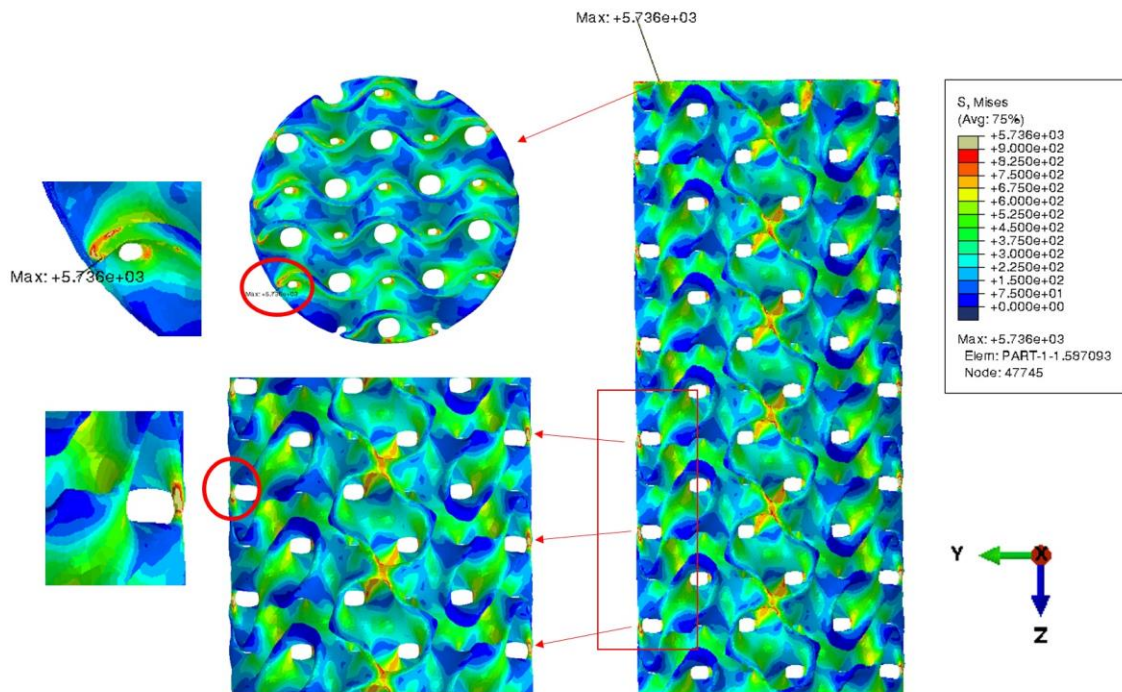


Figure 3.9: : Maximum Von Mises stress and regions with high-stress values at outer surface. (a) the maximum stress value was observed at the edge of the top surface due to the limitation in mesh sizing. (b) there were regions with no underlying support at the outer surface that exhibited artificially higher stress values due to design limitations, these numbers do not represent the strength of structure and were eliminated in this work.

Figure 3.10 depicts the von Mises stress distribution of cylinder G03, at different cross-sections in the X-Z plane. As described in the introduction, this structure minimizes the stress concentration, as can be seen across various cross-sections.

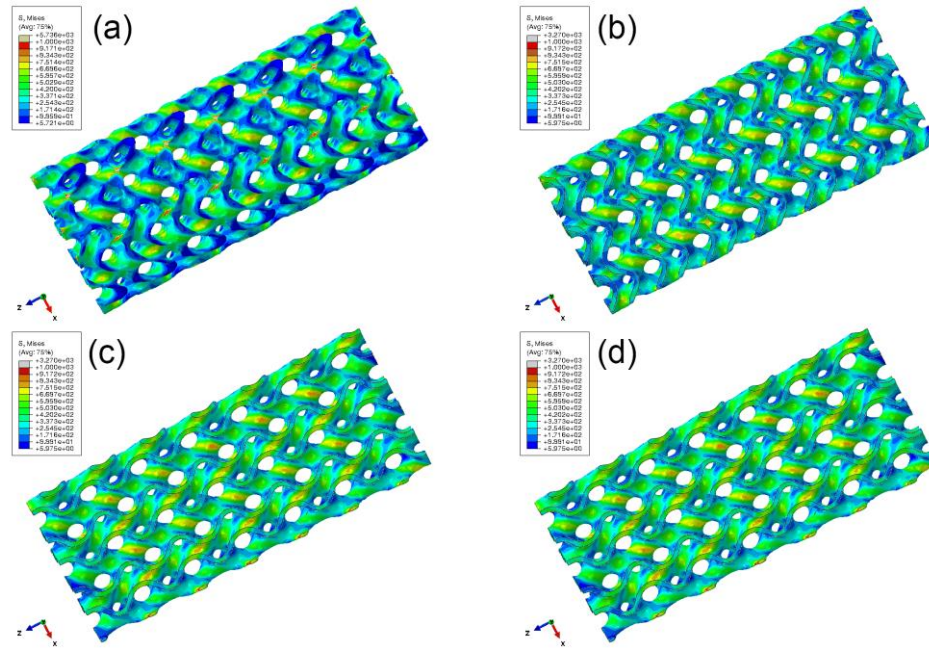


Figure 3.10: von Mises stress distributions of gyroid-based cylinder G03 (i.e., 80% porosity). (a) artifactually higher values were observed at the outer surface due to small regions with no support (b-d) these cross-sections better represent the smooth stress distribution within the model at various cross sections obtained by shifting in the y direction, perpendicular to the applied load.

The stress distribution was consistent across all modeled porosity values. However, higher von Mises stress values were obtained as the porosity increases (Fig 3.11). Displacements of the gyroid-based cylinders in the direction of compressive load were also recorded, as shown in Table 3.2. The difference in displacement magnitude was expected; gyroid-based cylinders exhibited greater displacement as the porosity increases. Effective elastic moduli of various porosity values were calculated by using the equivalent solid cylinder under the same load and boundary condition, as described in methods (3.2.2) and shown in Table 3.2

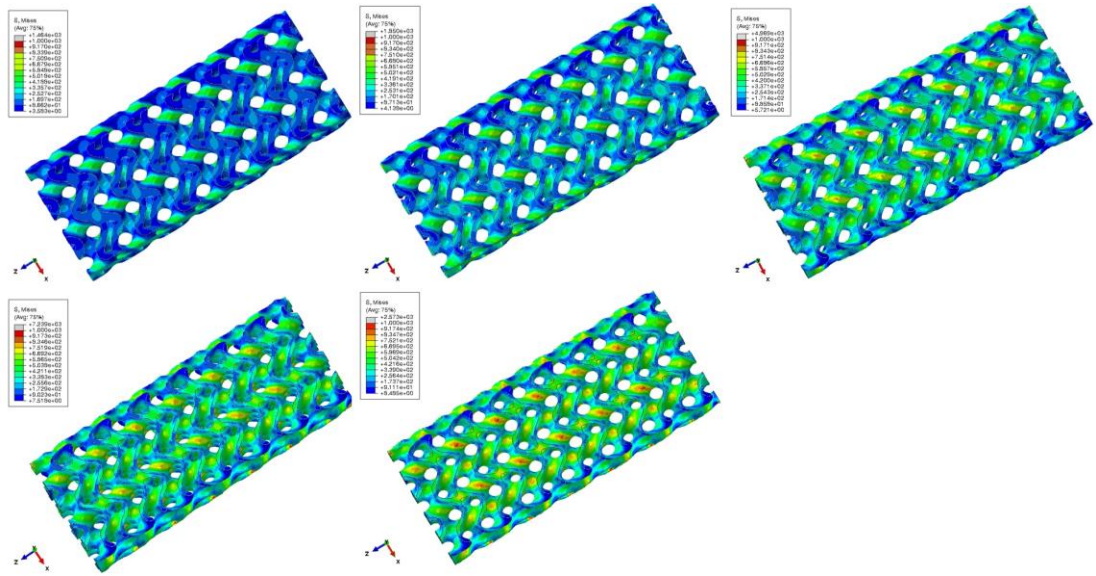


Figure 3.11: The contours of von Mises stress at one fixed cross-section in the X-Z plane for cylinder porosity (G01 – G05). The stress distribution is consistent among all porosity values, however, higher von Mises stresses were observed as the porosity increased.

Table 3.2: Calculated displacement and effective elastic moduli of gyroid-based cylinders with varying porosity ranging from (60-90%). All samples were tested under 10 kN compression load in ABAQUS software. G00 is the solid cylinder of 17 mm ×40 mm out of Ti6Al4V.

Name	Porosity %	Displacement (mm)	Effective Elastic Moduli (GPa)
G00	0	0.0152	113.8
G01	60	0.1050	16.5
G02	70	0.1500	11.5
G03	80	0.2050	8.4
G04	85	0.2200	7.9
G05	90	0.2500	7.0

Analysis of displacement and calculated effective elastic moduli *versus* varying porosity was performed using linear regression and non-linear Levenberg Marquardt fitting in Prism (GraphPad 8.1.2 software, Inc, La Jolla, CA) respectively. A second-order polynomial (quadratic) was the best-fit equation, with $R^2 > 0.99$ for the elastic moduli versus porosity plot.

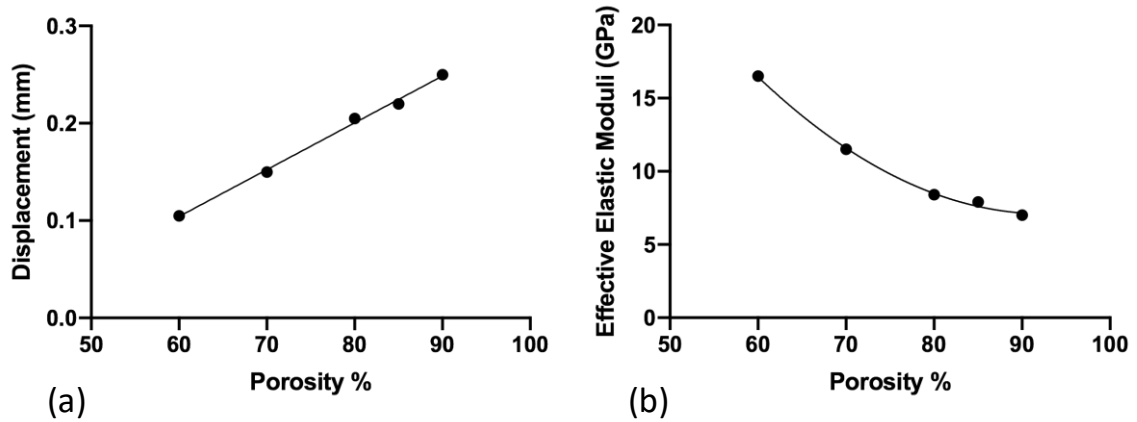


Figure 3.12: Plot of FE analysis results of gyroid-based cylinders' vs varying porosity

(a) Linear regression of displacement *vs* porosity ($R^2 = 0.99$) (b) Non-linear regression (quadratic) effective elastic moduli *vs* porosity ($R^2 = 0.99$)

We obtained the Von Mises stress values within the gyroid-based structures by manually identifying elements that had higher values inside the volume. Maximum Von Mises stress for G03 was reported at a range of 870-920 MPa, which is within the elastic region of Ti6Al4V, and just below the yield stress of 970 MPa. Cylinder G03 exhibited an elastic modulus of 8.4 GPa, which is higher than PMMA (2-3 GPa) and exhibited 80% porosity; thus G03 was selected to be loaded with the antibiotic-loaded carrier for the subsequent diffusion experiment.

3.3.2 Gyroid-based Cylinder Fabrication

Cylinders of various porosity values were fabricated using the 3D-metal printer (AM400, Renishaw plc, UK). The gyroid-based cylinders were built over 7 hours and 30 minutes using the laser parameters described in the methods section (3.2.3).

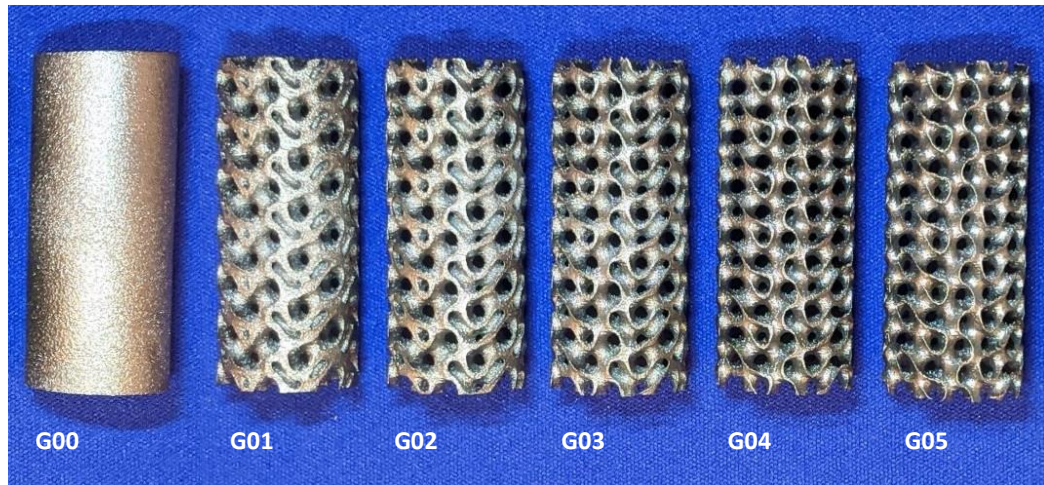


Figure 3.10: 3D-printed gyroid-based cylinders (17 mm length × 40 mm diameter) with varying porosity values G00) 0% G01) 60 G02) 70% G03) 80% G04) 85% G05) 90%. A 3D-metal printer (AM400, Renishaw plc, UK) was used with laser power of 400W and laser spot size of 70 μm .

Fabricated cylinders were then weighed on a scale with 1 mg accuracy. G01, G02, G03, G04, and G05 represented the mass of 13.777, 9.823, 6.283, 4.531, and 2.901 g, respectively, compared to the solid printed cylinder (G00) of 39.103 g. This demonstrated that by application of porous lattice structures, we can obtain sufficient mechanical properties while significantly reducing the weight of the component; thus, this approach can be used further to develop lightweight orthopedic components.

3.3.3 Diffusion coefficient Calculation

The estimate of the diffusion coefficient of Iohexol drug-surrogate through a plaster carrier within the gyroid-based porous structure of 80% porosity (*i.e.*, G03) was derived from the mathematical solution of Fick's second law for a cylindrical drug delivery system; this solution was represented in the literature [39, 40] and described in Chapter 2 (section 2.2.8).

Inner core gray-scale values at each time point were obtained and related to the Iohexol concentration. The release amount was then calculated by subtracting the initial concentration of Iohexol drug-surrogate from the remaining concentration level within the core. We defined the equation based on release amount in Prism (GraphPad 8.1.2 software, Inc, La Jolla, CA) for the application of non-linear regression and then fitted our CT-based intensity data to Equation 1 ($R^2 = 0.98$). The diffusion coefficient was then derived by non-linear Levenberg Marquardt fitting.

The diffusion coefficient of Iohexol drug-surrogate through a calcium-sulphate based carrier (*i.e.*, Plaster-of-Paris) within a gyroid-based porous cylinder was determined to be $0.5 \times 10^{-10} \text{ m}^2/\text{s}$. This value is lower than that reported in Chapter 2 for a plaster core without the presence of a metal scaffold (*i.e.*, $0.85 \times 10^{-10} \text{ m}^2/\text{s}$).

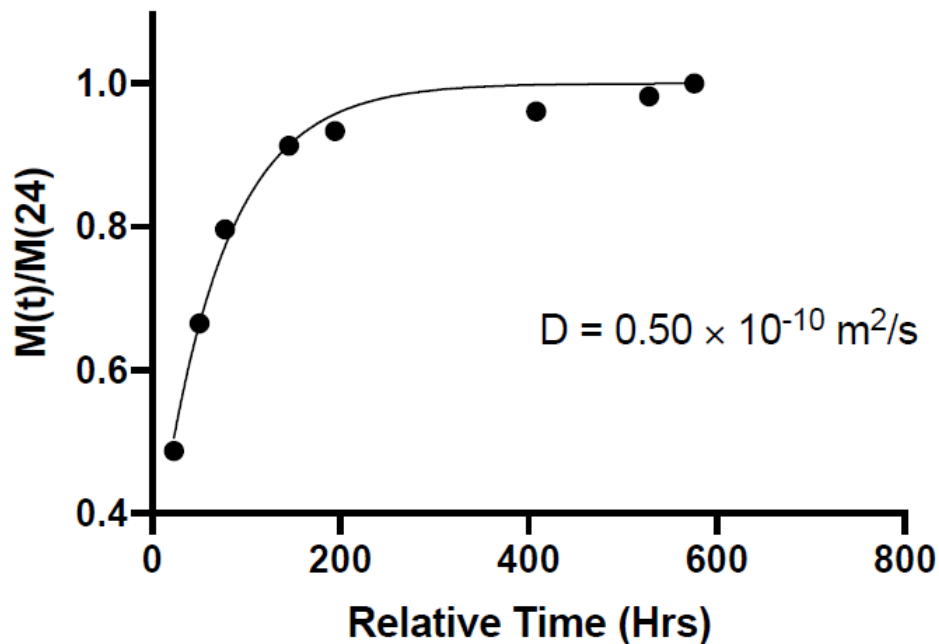


Figure 3.11: Plot of the cumulative release of Iohexol contrast agent vs. time. Contrast agent was embedded in plaster and was loaded into a gyroid-based cylinder of 80% porosity (*i.e.*, G03) and surrounded with an annulus of pure agar. The image data were fitted to the equation for a cylindrical geometry drug delivery carrier; a diffusion coefficient of $0.50 \times 10^{-10} \text{ m}^2/\text{s}$ was calculated.

3.4 Conclusion

3.4.1 Mechanical and Diffusion Characterization of a Porous Scaffold

We have developed a novel approach that can be used to address the current challenge of local antibiotic treatment in orthopedic device-related infection (ODRI). We propose that hybrid 3D-printed titanium scaffolds can provide structural support, while simultaneously incorporating carrier materials with high-dose antimicrobial agents to enhance the elution kinetics of conventional antibiotics in local drug delivery. Our target in this work was to design a porous structure for ODRI treatment with an effective elastic modulus higher than current bone-cement carriers (*i.e.*, PMMA with the elastic moduli of 2-3 GPa, [42]).

We have designed, fabricated, and tested a hybrid highly porous Ti alloy gyroid-based scaffold capable of being loaded with a drug-surrogate incorporated within enhanced carriers (*i.e.*, calcium-sulphate). The results showed that the gyroid-based structure can be fabricated out of Ti6Al4V using a laser power-bed fusion technique, and that by this approach, we can improve the mechanical properties of the entire delivery system. The effective elastic moduli of our designs were at the higher range (7-16.5 GPa), compared to the elastic moduli of current PMMA (2-3 GPa). The mechanical properties of the gyroid-based lattice structure are adjustable by altering the design parameters (*i.e.*, wall thickness, unit cell size), and we can modify our design according to the application. The ability to control the microarchitecture of the gyroid structure (and thereby the mechanical properties) will enable the application of these lattice structures for the design of orthopedic implants.

We were able to characterize small-molecule diffusion in an intact 3D phantom with the presence of a metal structure, using our quantitative micro-computed tomography (micro-CT) technique and beam-hardening correction algorithm. This technique was based on tracking a contrast agent surrogate tracer molecule (*i.e.*, Iohexol) with a molecular weight close to commonly used antibiotics. It has been shown that the open, accessible, gyroid-based architecture of the cylindrical scaffold that was fabricated by metal 3D-printing can be loaded with drug-surrogate impregnated calcium sulphate carriers and contrast agent molecules are observed to diffuse outward through the open-pore interconnected networks; this indicates that gyroid-based lattices exhibit a smooth transition between unit cells for the purpose of mass diffusion.

The beam-hardening correction [35] that was developed in-house reduced the artifact due to the presence of the metal structure, and it allowed us to determine the relative drop in gray-scale value at each time point within the inner core. However, the signal intensity had a low signal-to-noise ratio, making it difficult to analyze diametric line profiles over time. We obtained the cumulative release amount of contrast-agent drug surrogate at each time point, based on observed CT numbers, and thereby calculated the diffusion coefficient. We were able to fit our CT-data to a mathematical diffusion equation and calculate the Iohexol diffusion coefficient. Yao *et al.* previously described the application of a porous orthogonal Ti scaffold loaded with antibiotic-impregnated PMMA in the treatment of bone infection, and have also shown higher mechanical strength of the delivery system by the application of a porous Ti 3D-printed structure while enabling more controlled diffusion mechanisms [43]. To the best of our knowledge, the current work is the first time that the diffusion characteristic of a drug-surrogate has been investigated by a non-invasive technique (*i.e.*, micro-CT) while the drug-surrogate is embedded in an enhanced carrier (*i.e.*, calcium sulphate) within a porous metal structure. The result demonstrated that the diffusion coefficient of Iohexol through calcium sulphate would be reduced in the presence of a metal structure, compared to pure calcium sulphate; this could provide an advantage by allowing the antimicrobial agent to diffuse over a longer period of time and have an enhanced effect.

3.4.2 Limitations

The additive manufacturing process is associated with some limitations that should be noted while fabricating porous structures. “Internal voids” or “void porosity” has been defined as a porosity resulting from the fabrication process, and “porosity” refers to the open macroporosity of the porous structure (*i.e.*, volume fraction) [18]. In this work, the gyroid-based cylinders were considered to be completely solid in the FE simulations in ABAQUS, with no “internal voids.” However, the manufacturing process would affect the result and may lead to small internal voids associated with the structure; thus, we may have obtained higher mechanical properties in finite element analysis, compared to future experimental mechanical analysis by Instron material testing. It is worth noting that no obvious internal voids were observed in the CT scan data (Fig. 3.8). Previous studies have shown that thicker walls fabricated by metal 3D-printing would increase the likelihood of internal voids [18].

The other implication of the possibility of internal voids resulting from additive manufacturing is the nodal stress concentration at defects and voids. Although the gyroid-based lattice has minimum stress concentration naturally, artifactual defects due to additive manufacturing may lead to a drop in fatigue resistance of the structure and may need to be further addressed. If the gyroid-based scaffold undergoes mechanical failure in a load-bearing joint in the orthopedic application, it is potentially catastrophic and would cause severe complications *in vivo* in the future; thus, understanding the worst-case mode is critical before clinical application.

Here in this work, we used a 400 W laser power with a 70 μm laser spot size. However, the optimization of the laser parameters for maximizing printed scaffold density and minimizing defects can also be considered, and the selected laser parameters may not be the optimum to achieve the highest density in the relatively thicker walls. The effect of refined laser parameters can also be studied in the future.

Since metal implants in an orthopedic application are mainly loaded in compression, the body of this chapter regarding the mechanical evaluation of the porous gyroid-based cylinders is focused on compressive behavior. All samples were subjected to a 10 kN force, and models were solved for the deformation in the direction of applied force. There have been some previous studies on the tensile strength of gyroid-based lattice structures for orthopedic applications; Kelly *et al.* performed an experimental analysis and represented similar stretch-dominating behavior of titanium gyroid-based lattice structures, under both macroscopic compressive and tensile loading. The results indicate that gyroid-based structures are highly attractive for load-bearing applications and could be further studied for our purpose in the application in drug delivery. Due to the dynamic loading of body joints *in vivo*, fatigue strength analysis of gyroid-based structures could also be considered as a further improvement in our finite element analysis to validate our proposed architecture. Kelly *et al.* have also shown that gyroid-based lattice structures exhibit lower fatigue strength in tension, compared to compression [18].

While the laser powder-bed fusion technique is quite mature, as mentioned, there is still the risk that small structures will not be fully consolidated, which could compromise the mechanical properties. It is important to verify that the porous scaffolds we produce have

adequate strength in compression, consistent with the FEM predictions. We could further test our 3D-printed structures using the material testing equipment in our lab (Instron 5966) that will apply up to 10 kN compressive load. We can test our structures (using the ISO 13314 guidelines for porous materials) over the entire range of elastic and inelastic deformation to determine the yield strength and ultimate strength. The ultimate strength of cortical bone is about 140 MPa [44], so we will aim for at least 70% of that value with our scaffold; porosity can be reduced, if necessary.

3.4.3 Implications and Future Applications

Recent advances have made it possible to use CT-image data of a patient's joint structure and create a 3D-model by the application of CAD design, matching the patient anatomy to fabricate custom patient-specific implants. Moreover, the gyroid-based unit cell can be patterned to match any specific geometry and mechanical properties based on design parameters; thus by taking the advantage of recent advances in computer aided design (CAD) and additive manufacturing techniques, we can develop porous gyroid-based structures with complex internal microarchitectures that have mechanical and transport properties tailored to a specific orthopaedic application. This addresses the current challenges of two-stage revision surgeries in peri-prosthetic joint infections. We have shown that gyroid-based structures can carry antimicrobial agents for local treatment due to their porous nature, and could be retained as the definitive fixture in revision surgery – potentially eliminating the second stage of treatment.

Due to the porous nature of gyroid-based structures, we expect less image artifact caused by the metal cylinder – not only in CT-images, but also in other imaging modalities (such as MRI) compared to the bulk metal counterpart. This opens up a potential that may enable our lab to include the use of gadolinium-based MRI contrast agents, such as Magnevist® (Bayer, Leverkusen, Germany) in diffusion studies[45]. This MRI contrast agent has a higher molecular weight of 938 Da (compared to Iohexol with a molecular weight of 821 Da) and can be evaluated for quantitative diffusion characterization of small-molecule drug-surrogates within a porous structure in future studies to reproduce the result of this work.

The porous gyroid-based structure can also be studied *in-vivo* to evaluate the diffusion characteristics of drug-surrogates in animal models. It is expected that the open

interconnected network of the gyroid-based structure would also facilitate wetting properties *in vivo*. This may enhance the resorption of calcium-sulphate carriers, which would increase the diffusion rate. The open interconnected network may also enhance osseointegration following the resorption of a drug carrier; that possibility needs to be tested in the future.

3.4.4 Summary

This research demonstrates the capabilities of 3D metal printing to successfully fabricate complex structures with desired mechanical properties, while not compromising the porosity required to incorporate drugs in novel drug delivery systems. Recent advances in additive manufacturing could open up several new developments in the design and fabrication of a more advanced metal porous structure that could improve local drug delivery in PJI management. Gyroid-based porous structures exhibit promising features for application in local drug delivery, while the variation of design parameters enabled prescribed modulation of porosity and interconnectivity, and thus resulted in varying effective mechanical properties.

We were able to monitor the 2D diffusion of contrast agent drug surrogate through a hybrid metal/calcium-sulphate scaffold to an agar tissue-equivalent sink. A combination of drug impregnated carrier (*i.e.*, plaster) within the porous structure resulted in a lower diffusion coefficient, compared to its pure constituents. This may provide an advantage of elution over a more extended period, which may have a stronger effect on Staphylococcus bacteria. We can conclude that the application of a porous metal structure may be effective in the treatment of peri-prosthetic joint infection by local drug delivery, and can be applied to other applications in the future.

References

1. Qiu, X.S., et al., *Coating the plate with antibiotic cement to treat early infection after fracture fixation with retention of the implants: a technical note*. BMC Musculoskelet Disord, 2018. **19**(1): p. 360.
2. Moriarty, T.F., et al., *Orthopaedic device-related infection: current and future interventions for improved prevention and treatment*. EFORT Open Rev, 2016. **1**(4): p. 89-99.
3. Metsemakers, W.J., et al., *Influence of implant properties and local delivery systems on the outcome in operative fracture care*. Injury, 2016. **47**(3): p. 595-604.
4. Raschke, M., T. Vordemvenne, and T. Fuchs, *Limb salvage or amputation? The use of a gentamicin coated nail in a severe, grade IIIc tibia fracture*. Eur J Trauma Emerg Surg, 2010. **36**(6): p. 605-8.
5. Hutzler, L. and J. Williams, *Decreasing the Incidence of Surgical Site Infections Following Joint Replacement Surgery*. Bull Hosp Jt Dis (2013), 2017. **75**(4): p. 268-273.
6. Kamath, A.F., et al., *Quantifying the Burden of Revision Total Joint Arthroplasty for Periprosthetic Infection*. J Arthroplasty, 2015. **30**(9): p. 1492-7.
7. Kurtz, S.M., et al., *Economic burden of periprosthetic joint infection in the United States*. J Arthroplasty, 2012. **27**(8 Suppl): p. 61-5 e1.
8. Bhandari, M., et al., *Clinical and economic burden of revision knee arthroplasty*. Clin Med Insights Arthritis Musculoskelet Disord, 2012. **5**: p. 89-94.
9. *Hip and Knee Replacements in Canada, 2017 - 2018*. Canadian Joint Replacement Registry Annual Report, 2019. **Canadian Institute for Health Information**.
10. Frangiamore, S.J., et al., *alpha-Defensin Accuracy to Diagnose Periprosthetic Joint Infection-Best Available Test?* J Arthroplasty, 2016. **31**(2): p. 456-60.
11. Bishop, A.R., et al., *Vancomycin elution, activity and impact on mechanical properties when added to orthopedic bone cement*. J Mech Behav Biomed Mater, 2018. **87**: p. 80-86.
12. Laycock, P.A., et al., *In Vitro Efficacy of Antibiotics Released from Calcium Sulfate Bone Void Filler Beads*. Materials (Basel), 2018. **11**(11).
13. McConoughey, S.J., et al., *Comparing PMMA and calcium sulfate as carriers for the local delivery of antibiotics to infected surgical sites*. J Biomed Mater Res B Appl Biomater, 2015. **103**(4): p. 870-7.

14. Dusane, D.H., et al., *Effects of loading concentration, blood and synovial fluid on antibiotic release and anti-biofilm activity of bone cement beads*. J Control Release, 2017. **248**: p. 24-32.
15. Abueidda, D.W., et al., *Mechanical properties of 3D printed polymeric Gyroid cellular structures: Experimental and finite element study*. Materials & Design, 2019. **165**.
16. Walker, J.M., et al., *Design and mechanical characterization of solid and highly porous 3D printed poly(propylene fumarate) scaffolds*. Progress in Additive Manufacturing, 2017. **2**(1-2): p. 99-108.
17. Ma, S., et al., *Mechanical behaviours and mass transport properties of bone-mimicking scaffolds consisted of gyroid structures manufactured using selective laser melting*. J Mech Behav Biomed Mater, 2019. **93**: p. 158-169.
18. Kelly, C.N., et al., *Fatigue behavior of As-built selective laser melted titanium scaffolds with sheet-based gyroid microarchitecture for bone tissue engineering*. Acta Biomater, 2019. **94**: p. 610-626.
19. Buck, D.W., 2nd and G.A. Dumanian, *Bone biology and physiology: Part I. The fundamentals*. Plast Reconstr Surg, 2012. **129**(6): p. 1314-20.
20. Khaderi, S., V. Deshpande and N. Fleck, *The stiffness and strength of the gyroid lattice*. International Journal of Solids and Structures, 2014. **51**: p. 3866-3877.
21. Olivares, A.L., et al., *Finite element study of scaffold architecture design and culture conditions for tissue engineering*. Biomaterials, 2009. **30**(30): p. 6142-9.
22. Melchels, F.P., et al., *Effects of the architecture of tissue engineering scaffolds on cell seeding and culturing*. Acta Biomater, 2010. **6**(11): p. 4208-17.
23. Michielsen, K. and D.G. Stavenga, *Gyroid cuticular structures in butterfly wing scales: biological photonic crystals*. J R Soc Interface, 2008. **5**(18): p. 85-94.
24. Landh, T., *From entangled membranes to eclectic morphologies: cubic membranes as subcellular space organizers*. FEBS Lett, 1995. **369**(1): p. 13-7.
25. Olmsted, P.D. and S.T. Milner, *Strong-segregation theory of bicontinuous phases in block copolymers*. Phys Rev Lett, 1994. **72**(6): p. 936-939.
26. Shi, J., et al., *A TPMS-based method for modeling porous scaffolds for bionic bone tissue engineering*. Sci Rep, 2018. **8**(1): p. 7395.
27. Schoen, A.H., *Infinite periodic minimal surfaces without self-intersections*. NASA Technical Report, 1970. **D-5541**.
28. Chen, Y., et al., *Fabrication of porous titanium implants with biomechanical compatibility*. Materials Letters - MATER LETT, 2009. **63**: p. 2659-2661.

29. Wauthle, R., et al., *Additively manufactured porous tantalum implants*. Acta Biomater, 2015. **14**: p. 217-25.
30. Moatamedi, M. and H.A. Khawaja., *Finite Element Analysis*. 2018: CRC press.
31. Perillo-Marcone, A., A. Alonso-Vazquez, and M. Taylor, *Assessment of the effect of mesh density on the material property discretisation within QCT based FE models: a practical example using the implanted proximal tibia*. Comput Methods Biomech Biomed Engin, 2003. **6**(1): p. 17-26.
32. Zimmerman, R.W., *Compressibility of Sandstones*. 1991.
33. Ter Haar, G.M. and T.H. Becker, *Selective Laser Melting Produced Ti-6Al-4V: Post-Process Heat Treatments to Achieve Superior Tensile Properties*. Materials (Basel), 2018. **11**(1).
34. Souza, R., et al., *Standard operating procedure to prepare agar phantoms*. Journal of Physics: Conference Series, 2016. **733**: p. 012044.
35. Edey, D.R., et al., *Extending the dynamic range of biomedical micro-computed tomography for application to geomaterials*. J Xray Sci Technol, 2019. **27**(5): p. 919-934.
36. Chen, M., et al., *An Analytical Method for Reducing Metal Artifacts in X-Ray CT Images*. Mathematical Problems in Engineering, 2019. **2019**: p. 1-7.
37. Feldkamp, L.A., L.C. Davis, and J.W. Kress, *Practical cone-beam algorithm*. Journal of the Optical Society of America A, 1984. **1**(6): p. 612-619.
38. Du, L.Y., et al., *A quality assurance phantom for the performance evaluation of volumetric micro-CT systems*. Phys Med Biol, 2007. **52**(23): p. 7087-108.
39. Mircioiu, C., et al., *Mathematical Modeling of Release Kinetics from Supramolecular Drug Delivery Systems*. Pharmaceutics, 2019. **11**(3).
40. Siepmann, J. and F. Siepmann, *Modeling of diffusion controlled drug delivery*. J Control Release, 2012. **161**(2): p. 351-62.
41. R. Boyer, G.W., and E. W. Collings, *Materials Properties Handbook: Titanium Alloys*. 1994, ASM International, .
42. Abreu, E., *Mow VC, Huiques R: Basic Orthopaedic Biomechanics and Mechano-Biology. 3rd edition*. Biomedical Engineering Online - BIOMED ENG ONLINE, 2005. **4**: p. 1-1.
43. Yao, Q., et al., *Mechanical and In Vitro Antibacterial Properties of a Porous Ti-6Al-4V Scaffold Combined with Vancomycin-Loaded Polymethyl Methacrylate by Three-Dimensional Printing*. Journal of Biomaterials and Tissue Engineering, 2018. **8**: p. 740-749.

44. Bayraktar, H.H., et al., *Comparison of the elastic and yield properties of human femoral trabecular and cortical bone tissue*. J Biomech, 2004. **37**(1): p. 27-35.
45. Hong. G., K.T., Cobos. S., Drangova. M., Holdsworth. D., *MRI characterization of a novel porous 3D printed metal scaffold*, in *Imaging network ontario*. 2020: Toronto.

Chapter 4

4 Conclusion and Future Directions

4.1 Summary

The ability to provide a better understanding of small-molecule diffusion characteristics is essential to the development of improved, local, drug-delivery systems. Local drug delivery is an important component in the standard treatment in orthopedic-device-related infection (ODRI), but little is known of how the antimicrobial agents diffuse through the carriers into the target tissue. In this work, we have characterized the two-dimensional (2D) diffusion of small-molecules, non-invasively, using a micro-CT imaging technique. Conventional CT imaging has been previously employed for studying the local diffusion characteristics of platinum-based, clinically-administered drugs, such as carboplatin and cisplatin [1], which are used in cancer treatment. Because they contain a heavy element, platinum, that effectively attenuates X-rays, these drugs have intrinsically good image contrast and require no additional contrast agent for image conspicuity. However, antimicrobial agents that are used in infection treatment in ODRI are not easily detected in micro-CT imaging, as they do not possess appropriate X-ray attenuating properties. Hence, a radiopaque contrast agent (Iohexol) was chosen for use as a drug-surrogate in this study. Iohexol can act as a drug mimic to visualize diffusion. Although it cannot be assumed that antimicrobial agents like Vancomycin will exhibit exactly the same diffusion characteristics as the contrast agent, this approach provided a better evaluation of the relative-diffusion characteristics of small-molecules from a finite source to a surrounding environment in ODRI.

Iohexol has been well studied in biological systems [2] and has a molecular weight of 821 Da that is close to commonly used antibiotics in ODRI treatment, such as Vancomycin with molecular weight 1449 Da. A preliminary test was designed and performed by incorporating the contrast agent into an agar carrier. The diffusion into the agar was tracked, which validated our micro-CT, acquisition parameters, and artifact correction algorithms for quantitative diffusion characterization. Further experiments were designed to determine the diffusion characteristics of the drug-surrogate from enhanced carriers made of calcium-sulphate based matrices (Plaster-of-Paris and Stimulan®).

Both mineral-based and polymethylmethacrylate (PMMA) carriers suffer from poor mechanical strength, which is further degraded by incorporating a high-dose of antimicrobial agents [3], therefore; in this work, we also proposed a new design for incorporating an antibiotic carrier inside a porous metal structure. A carrier with good elution and resorption properties can effectively deliver a sustained dose of antibiotic, while the metal structure provides structural integrity.

Gyroid-based porous metal cylinders of various porosities were designed and 3D printed in a Titanium alloy. Finite-element analysis was used to model our structures under compression loads. The von Mises stress distribution and deformation of each porosity were modeled and the effective elastic moduli were calculated. Gyroid cylinders were then fabricated using the laser-power bed-fusion technique. We selected the gyroid cylinder of 80% porosity for diffusion experiments because it represented the effective elastic moduli of 8.4 GPa that is higher than PMMA (*i.e.*, 2-3 Gpa), and its 80% porosity enabled the loading of a drug-surrogate, impregnated, calcium-sulfate carrier (plaster). The two-dimensional diffusion of the Iohexol into an agar was then evaluated using the optimized micro-CT imaging technique.

This micro-CT data enabled us to estimate the diffusion coefficient of the drug-surrogate using mathematical models [4, 5]. The diffusion coefficient of Iohexol was calculated within various carriers (Table 4.1). As expected, Iohexol molecules diffused at a higher rate in agar carriers compared to polymeric, calcium-sulphate based matrices.

Signal-intensity profile plots across the diameter of the carriers were found to be a good visual representation of the diffusion of Iohexol over time. Both calcium-sulphate matrices exhibited similar signal-intensity profiles over time, thus validating the application of Plaster-of-Paris as a viable, cost-effective alternative to Stimulan[®] for the study of diffusion. While the two calcium-sulphate based carriers exhibited very similar relative diffusion properties, it should be noted that in the calculation of quantitative, mass-transport properties, Plaster-of-Paris yielded a higher value for the diffusion coefficient, compared to Stimulan[®]. This difference in the quantitative material properties is primarily due to the two different forms of calcium-sulphate that compose these two materials, as well as some possible additional trace chemicals and impurities [6].

For the case of Iohexol incorporated in the plaster carrier and then loaded into an 80% porosity gyroid cylinder, the estimated diffusion coefficient dropped 41% compared to the comparable pure plaster core with no metal gyroid. A similar reduction in diffusion rate by the application of a porous, metal, 3D-printed, orthogonal structure was previously reported [7], and is consistent with our results.

Metal structures exhibit high attenuation of X-ray photons that cause significant image artefacts due to phenomena such as X-ray beam-hardening of the polychromatic spectrum and scatter [8]. By implementing a post-processing, beam-hardening, correction algorithm [9] developed in-house, and application of spatial averaging due to geometric symmetry, we were able to reduce metal artifacts sufficiently to obtain the cumulative release amount of the Iohexol [1] into the surrounding agar by measuring signal loss at the inner core. Unfortunately, the signal-to-noise (SNR) ratio was not sufficient to track the radial-diffusion distance longitudinally in the presence of a metal component.

Previous studies by Exner *et al.* have demonstrated the feasibility of conventional CT to qualitatively monitor *in vivo*, local, drug pharmacokinetics from polymeric implants in small-animal models [1, 10]. They tracked diffusion of drug-loaded (Iohexol and platinum-based carboplatin), polymeric implants through the rat liver, before and after radiofrequency ablation treatment. We have extended this approach by developing non-invasive, micro-CT imaging techniques with sufficient spatial resolution to qualitatively and quantitatively track drug pharmacokinetics through metal 3D printed implants for orthopedic applications.

To summarize, we believe that this study is the first to measure the diffusion coefficient of a drug-surrogate within a porous, metal structure using a non-invasive, imaging technique to acquire diffusion data and a fit to mathematical models. This *in-vitro* work offers a clear understanding of the mechanism of mass-diffusion for local drug delivery because other transport mechanisms, such as resorption, were not present in our phantom-based study [7]. Using the micro-CT imaging technique, image post-processing, porous-scaffold design and manufacturing, and mathematical modeling techniques developed here for the *in-vitro* experiments to measure passive diffusion, this technique could be further extended to animal models to measure both passive diffusion and other possible mechanisms *in-vivo* that would affect the diffusion rate of various drugs.

Table 4.3: Iohexol diffusion coefficient (m²/s) through various cylindrical core carriers to the annular, agar tissue-equivalent, sink. The diffusion coefficients were obtained by fitting the CT-image data to the diffusion mathematical models.

Core Carrier	Diffusion Coefficient (m²/s)
Agar	2.26×10^{-10}
Stimulan®	0.46×10^{-10}
Plaster-of-Paris	0.85×10^{-10}
Plaster-of-Paris in metal scaffold	0.50×10^{-10}

4.2 Future Directions

Although *in-vitro* experiments are cost-effective approaches, *in-vivo* animal studies are the next, critically important step in preclinical research to expand our knowledge and for the development of new treatment approaches in ODRI. As is often the case, preliminary work carried out *in vitro* is useful for refining techniques, choosing mathematical or theoretical models, designing and building apparatus, and refining one’s basic understanding, all of which is excellent preparation for extension to the *in-vivo* environment which is invariably much richer and more complex. While we have shown in this work that it is possible to measure small-molecule diffusion in intact phantoms using a drug-surrogate, this work does not yield a full understanding of *in-vivo* diffusion due to other mechanisms that come into play, such as the resorption of calcium-sulphate carriers, and wetting properties of the carrier that affect the diffusion rate upon local treatment [11]. Other *in-vivo* transport mechanisms can be explored and evaluated by implementing our micro-CT technique in animal models. We first need to explore the *in-vivo* feasibility of this micro-CT imaging technique for further studies.

Pre-clinical studies generally entail the use of small-animals, such as rats, and mice to be more cost-effective [12]. Small-animal imaging applications require isotropic voxel sizes on the order of 100 μm or less [13] – much smaller than is available on conventional CT scanners. This work was performed on an eXplore SpeCZT micro-CT scanner (General

Electric Healthcare, London, Ontario), which provides the fast scanning comparable to clinical scanner with a high resolution – isotropic voxel spacing of 50 μm .

Since the animal has to be anesthetized during image acquisition to minimize subject motion, the scan must be relatively short, so an imaging protocol with a 5-minute scan duration was selected for our work. Small animals can also undergo multiple, short-duration scans at defined time intervals to evaluate the diffusion for an extended period. One can try to make intuitive guesses about how often scans are required in order to accurately characterize a diffusion profile, but these preliminary experiments make it clear that our 5-minute scan durations are short enough to sample the diffusion profile, while maintaining adequate image quality.

In the extension of our *in-vitro* experiments using a drug surrogate to track the *in-vivo* diffusion in animal-models, there are additional considerations such as toxicity. Fortunately, the Iohexol employed in this study is a low-osmolality, non-ionic, monomer, contrast agent, and one of the most commonly used iodinated compounds that is routinely administered in small-animal preclinical research studies, veterinary science [14], and clinical medicine. Thus, we will be able to continue to use Iohexol in the study of diffusion in small-animal models as a tracer source and also for further clinical tests.

Although our micro-CT image acquisition parameters can be directly implemented to measure diffusion in small-animal models, it may achieve an insufficient signal-to-noise (SNR) ratio to monitor in-plane diffusion, even after spatial averaging, due to the smaller scale of animal subjects. This may lead to potential difficulties in obtaining the radial diffusion distance of a drug-surrogate over time. However, based on previous literature [1, 10], we expected to achieve sufficient SNR to be able to quantitatively assess the tracer loss from the core carrier over time, and thus calculate the cumulative release amount (based on the law of conservation of mass).

Unfortunately, micro-CT scans come with an associated dose from ionizing radiation, that is cumulative upon serial scanning protocols, and which may result in adverse effects on live animals. Dose is a significant concern when the employed radiation interferes with the study results – mainly in the evaluation of structural changes or tumor development. It is unknown whether there would be any effect from this radiation on our diffusion measurements.

However, Detombe *et al.* reported the effect of inducing dose on lung and myocardial tissue of mice by performing scans twice weekly for 6 weeks with 80 kVp tube voltage and 50mA tube current, resulting in a weekly dose of 0.84 Gy, and a total study dose of 5.04 Gy, and reported no significant difference between the control group and the irradiated group [15]. Miyahara *et al.* performed a study on the effect of induced dose on mice by micro-CT using 90 KVp tube voltage (identical to ours) and showed that micro-CT, in general, induces a very-low dose of radiation to a subject. For example, frequent micro-CT scans for a period of 4 weeks only give an average dose of 194.3 mGy, and he concluded that "*It is unlikely that an extremely-low dose can cause any acute radiation damage to mice*"[16]. Still, the induced radiation dose needs to be studied prior to the clinical implementation of this technique in ODRI treatment.

To implement porous metal structures loaded with drug-surrogate impregnated carriers in animal models, we also need to investigate the capability of the 3D metal printer to fabricate gyroid-based, porous scaffolds at a small-animal scale. Due to the smaller size in the small-animal models, the deviation of the CAD geometry design from an actual fabricated structure needs to be addressed. However, our group has previously introduced the first metal hip implant for hemi-arthroplasty in a rat using a metal 3D-printer [17]. This bodes well for the capability of the in-house, metal 3D printer in the application of further diffusion studies in small-animal models.

High concentrations of drug-surrogate contrast agent yield high signal intensity and facilitate the ability to track diffusion, however, they also lead to image artifacts, such as beam-hardening and increased scatter. A study to optimize the concentration level of Iohexol contrast agent may be useful to balance the need for our beam-hardening, artifact correction methods based with the desire for high signal intensity to track drug-surrogates over an extended period of time.

Other imaging modalities such as magnetic resonance imaging (MRI) may prove useful in the development of non-invasive diffusion characterization techniques. Using commonly employed MRI contrast agents with higher molecular weights such as Gd-DTPA, tradename Magnevist[®] (Bayer, Leverkusen, Germany), with a molecular weight of 938 Da, and a comparison of the result with our CT-based experiments may shed further light on our

understanding of diffusion in small-molecules. The use of a variety of contrast agents opens up the possibility to investigate the effect of molecular weight on diffusion. Additionally, the use of MRI negates any ionizing radiation dose burden that is inherent with micro-CT based studies.

Diffusion coefficient values calculated in this work can also be used in computational models to validate diffusion models based on our experimental evidence. Validated numerical models facilitate further investigation, while minimizing the need for animal or human subjects. They also provide a framework for work in more complex 3D structures and for the evaluation of the effect of geometry on diffusion. Both CT-derived, patient-specific, or generic anatomical geometry can also be incorporated into numerical diffusion models to study diffusion in ODRI. These models allow us to manipulate a variety of transport properties and investigate the extent to which they are important in the diffusion mechanisms.

The level of osteo-integration into the porous, gyroid scaffold can also be studied via histology in small-animal models. While calcium sulphate has superior elution kinetics compared to PMMA carriers, it also exhibits an osteoconductive nature that can improve bone formation. Calcium-sulphate based materials are currently applied to implant substrates to improve bone-implant fixation [18], thus, we expect that resorbed calcium-sulphate carrier can be replaced by bone formation within the open-pore network of our proposed gyroid-based scaffold. This would improve the mechanical properties of the structure and would facilitate the permanent retention of the porous scaffold, and may even lead to the elimination of two-stage revision surgeries.

PMMA is the current clinical standard material for carriers, but it is not ideal, and others with different diffusion, resorption, and mechanical properties may demonstrate superior performance. We started this research with the relatively low-risk material for current PMMA carriers, and evaluated the diffusion of tracers through calcium-sulphate matrices. We can also explore more innovative approaches in the future for antibiotic release, using stimuli-responsive materials. The first group of materials to be investigated could include pH-sensitive, acetal-containing polymers that can be used to encapsulate antimicrobial agents [19]. This may be an effective strategy for controlled release, because pH is reduced in tissue

near an infection [20]. The polymers can be designed to degrade at varying rates depending on the acetal structure, thereby releasing drug-surrogate over controllable time frames and in a pH-dependent manner [21]. Temperature change can also be used as a stimulus, particularly in conjunction with RF-induced hyperthermia. We can employ biodegradable poly(ester amide)s (PEAs) that undergo a glass transition just above 37°C [22]. Upon transition, the diffusion rate of the drug out of the polymer increases [23]. The polymers can be synthesized and characterized by methods including NMR spectroscopy, thermal analysis, and size-exclusion chromatography. Chemical modifications can also be introduced, as needed, to enhance coating and adhesion to the porous, metal scaffolds, and micro-CT can be performed to monitor diffusion through suggested novel carriers.

Heating titanium gyroid-based components within the body to a temperature (typically over 55°C) is useful to the disruption of harmful biofilms in case of permanent implantation of porous scaffolds. In the future, we could take advantage of the phenomenon of high-frequency, electromagnetic field use for non-contact heating of metals [24] and we can investigate the effects of heating gyroid-based porous-scaffold surfaces (rather than the interior) by using coils operating at high frequencies to obtain the “skin” effect [25]. Accurate measurements of the implant and nearby-tissue temperatures should be performed to avoid inadvertent damage to the adjacent tissue. It is expected that temperatures above 50°C may cause damage to healthy tissues (*i.e.*, bone, muscle, vessels), and that sustained temperatures above 70°C cause tissue necrosis [26-28]. Once we have developed the required tools to heat titanium scaffolds and measure surface temperatures, we can investigate the effect of hyperthermia on bacteria and biofilms *in vitro* and further in animal-models.

Despite the lack of *in-vivo* data in this work, certainly our ultimate goal is to develop techniques that will reduce the number of costly (and time-consuming) two-stage therapy in ODRI, specifically PJI. Towards this objective, we have provided a quantitative technique to track diffusion characteristics of small-molecules through carriers embedded in a highly-porous metal scaffold. We are not the first group to suggest porous structures [29], but, to the best of our knowledge, we are the first that have described the use of calcium-sulphate matrices within a titanium gyroid-based porous structure for infection treatment. Application of porous structures can also be used to provide local delivery of other agents such as growth factors, bone morphogenic protein, and cancer drugs, in the future.

4.3 References

1. Exner, A.A., et al., *Quantitative computed tomography analysis of local chemotherapy in liver tissue after radiofrequency ablation*. Acad Radiol, 2004. **11**(12): p. 1326-36.
2. Nath, R., N. Yue, and J. Weinberger, *Dose perturbations by high atomic number materials in intravascular brachytherapy*. Cardiovasc Radiat Med, 1999. **1**(2): p. 144-53.
3. Jung, J., et al., *Complications after spacer implantation in the treatment of hip joint infections*. Int J Med Sci, 2009. **6**(5): p. 265-73.
4. Siepmann, J. and F. Siepmann, *Modeling of diffusion controlled drug delivery*. J Control Release, 2012. **161**(2): p. 351-62.
5. J., C., *Diffusion_Crank-MathematicsofDiffusion*. second ed. 1975: CLARENDON PRESS.
6. Oliver, R.A., et al., *Application of Calcium Sulfate for Dead Space Management in Soft Tissue: Characterisation of a Novel In Vivo Response*. Biomed Res Int, 2018. **2018**: p. 8065141.
7. Yao, Q., et al., *Mechanical and In Vitro Antibacterial Properties of a Porous Ti-6Al-4V Scaffold Combined with Vancomycin-Loaded Polymethyl Methacrylate by Three-Dimensional Printing*. Journal of Biomaterials and Tissue Engineering, 2018. **8**: p. 740-749.
8. Chen, M., et al., *An Analytical Method for Reducing Metal Artifacts in X-Ray CT Images*. Mathematical Problems in Engineering, 2019. **2019**: p. 1-7.
9. Edey, D.R., et al., *Extending the dynamic range of biomedical micro-computed tomography for application to geomaterials*. J Xray Sci Technol, 2019. **27**(5): p. 919-934.
10. Szymanski-Exner, A., et al., *Noninvasive monitoring of local drug release using X-ray computed tomography: optimization and in vitro/in vivo validation*. J Pharm Sci, 2003. **92**(2): p. 289-96.
11. Mircioiu, C., et al., *Mathematical Modeling of Release Kinetics from Supramolecular Drug Delivery Systems*. Pharmaceutics, 2019. **11**(3).
12. National Research, C., B. Institute of Medicine Committee on the Use of Laboratory Animals in, and R. Behavioral, in *Use of Laboratory Animals in Biomedical and Behavioral Research*. 1988, National Academies Press (US) Copyright (c) National Academy of Sciences.: Washington (DC).

13. Ritman, E.L., *Small-animal CT - Its Difference from, and Impact on, Clinical CT*. Nuclear instruments & methods in physics research. Section A, Accelerators, spectrometers, detectors and associated equipment, 2007. **580**(2): p. 968-970.
14. Kirberger, R.M., et al., *The effects of repeated intravenous iohexol administration on renal function in healthy beagles--a preliminary report*. Acta Vet Scand, 2012. **54**: p. 47.
15. Detombe, S.A., et al., *X-ray dose delivered during a longitudinal micro-CT study has no adverse effect on cardiac and pulmonary tissue in C57BL/6 mice*. Acta Radiol, 2013. **54**(4): p. 435-41.
16. Miyahara, N., et al., *Evaluation of X-ray doses and their corresponding biological effects on experimental animals in cone-beam micro-CT scans (R-mCT2)*. Radiol Phys Technol, 2016. **9**(1): p. 60-8.
17. Paish, A., et al., *Towards optimizing a custom small animal model of partial joint replacement system created via additive manufacturing*. Frontiers in Bioengineering and Biotechnology, 2016. **4**.
18. Chen, D., et al., *Osseointegration of porous titanium implants with and without electrochemically deposited DCPD coating in an ovine model*. J Orthop Surg Res, 2011. **6**: p. 56.
19. Paramonov, S.E., et al., *Fully acid-degradable biocompatible polyacetal microparticles for drug delivery*. Bioconjug Chem, 2008. **19**(4): p. 911-9.
20. Pichavant, L., et al., *pH-controlled delivery of gentamicin sulfate from orthopedic devices preventing nosocomial infections*. J Control Release, 2012. **162**(2): p. 373-81.
21. Gillies, E.R., A.P. Goodwin, and J.M. Frechet, *Acetals as pH-sensitive linkages for drug delivery*. Bioconjug Chem, 2004. **15**(6): p. 1254-63.
22. Villamagna, I.J., et al., *Poly(ester amide) particles for controlled delivery of celecoxib*. J Biomed Mater Res A, 2019. **107**(6): p. 1235-1243.
23. Viger, M.L., et al., *Near-infrared-induced heating of confined water in polymeric particles for efficient payload release*. ACS Nano, 2014. **8**(5): p. 4815-26.
24. Pijls, B.G., et al., *Non-contact electromagnetic induction heating for eradicating bacteria and yeasts on biomaterials and possible relevance to orthopaedic implant infections: In vitro findings*. Bone Joint Res, 2017. **6**(5): p. 323-330.
25. Wu, Z., et al., *An induction heating device using planar coil with high amplitude alternating magnetic fields for magnetic hyperthermia*. Technol Health Care, 2015. **23 Suppl 2**: p. S203-9.

26. Muffly, M.T., et al., *Cadaveric Study of Bone Tissue Temperature During Pin Site Drilling Using Fluoroptic Thermography*. J Orthop Trauma, 2018. **32**(8): p. e315-e319.
27. Timon, C. and C. Keady, *Thermal Osteonecrosis Caused by Bone Drilling in Orthopedic Surgery: A Literature Review*. Cureus, 2019. **11**(7): p. e5226.
28. Mediouni, M., et al., *An overview of thermal necrosis: present and future*. Curr Med Res Opin, 2019: p. 1-8.
29. Yao, Q.Q., et al., *Mechanical and In Vitro Antibacterial Properties of a Porous Ti-6Al-4V Scaffold Combined with Vancomycin-Loaded Polymethyl Methacrylate by Three-Dimensional Printing*. Journal of Biomaterials and Tissue Engineering, 2018. **8**(5): p. 740-749.

Curriculum Vitae

Name: Tina Khazae

Post-secondary Education and Degrees: Biomedical Engineering
Tehran, Iran
2006-2010 B.Sc.

Biomedical Engineering
Tehran, Iran
2010-2012 M.Sc.

Medical Biophysics
London, Ontario, Canada
2018-2020 M.Sc.

Scholarships and Awards: Collaborative Training in Musculoskeletal Health
Research Transdisciplinary Bone & Joint Award
2018-2020

Western Graduate Scholarship (WGRS)
2018-2020

Related Work Experience Teaching Assistant
Western University
2018

Publications and Presentations:

1. A.Lakzadeh, **T. Khazaei**, A. Ataei, S-23 Influence of Femoral Component Material Properties on Stress Shielding in Total Hip Replacement, Journal of Biomechanics, 43(1), pp38-39, 2010
2. **Tina Khazae**, Hristo N. Nikolov, Chris Norley, and David W. Holdsworth. Micro-CT imaging technique to characterize diffusion of small molecules, Poster Presentation at the 2019 London Health Research day.
3. **Tina Khazae**, Chris J.D Norley, Hristo N. Nikolov, Steven I. Pollmann and David W. Holdsworth. Micro-CT imaging technique to characterize diffusion of small- molecules, Oral Presentation at the 2020 SPIE Medecial Imaging Conference, Houston, Texas, US.

4. **Tina Khazae**, Chris J.D Norley, Hristo N. Nikolov, Steven I. Pollmann and David W. Holdsworth, Micro-CT imaging technique to characterize diffusion of small- molecules. proceeding of the SPIE, Medical Imaging 2020: Biomedical Applications in Molecular, Structural, and Functional Imaging, Volume 11317.
5. **Tina Khazae**, Chris J.D Norley, Steven I. Pollmann, Hristo N. Nikolov, and David W. Holdsworth. Non-destructive Quantification of Small Molecules. Diffusion using Micro-CT. Poster Presentation at the 2020 Imaging network Ontario (IMNO), Toronto, Ontario.
6. Gregory Hong, **Tina Khazae**, Santiago Cobos, Maria Drangova, David W Holdsworth. MRI characterization of a novel porous 3D printed metal scaffold. Oral presentation in at the 2020 Imaging network Ontario (IMNO), Toronto, Ontario.